Experimental and Numerical Modeling of Aerosol Generation for the Treatment of Respiratory Distress Syndrome in Preterm Infants

eman ta zabal zazu

Universidad del País Vasco
Euskal Herriko Unibertsitatea

PhD THESIS

Author: Iñigo Aramendia Iradi

Supervised by:
Dr. Unai Fernández Gámiz
Dr. Javier Sancho Saiz

Nuclear Engineering and Fluid Mechanics Department
Faculty of Engineering - Vitoria-Gasteiz
University of the Basque Country UPV/EHU

November 2019

(cc)2019 IÑIGO ARAMENDIA IRADI (cc by-nc-sa 4.0)

Acknowledgements

This thesis has been carried out from November 2015 to November 2019 at the Nuclear Engineering and Fluid Mechanics Department of the University of the Basque Country (UPV/EHU). It has been a truly life-changing experience for me and it would not have been possible to do without the support and help that I received from many people.

Foremost, I would like to express my deepest and sincere gratitude to my supervisors: Professor PhD Unai Fernández Gámiz and Professor PhD Javier Sancho. I am particularly grateful to Unai Fernández Gámiz for his constant guidance and motivation throughout all these years. This thesis would not have been possible without his dedication and enthusiasm in each stage of this research work. I could not have imagined having a better advisor and mentor for my Ph.D study. I would also like to declare my sincere gratitude to Javier Sancho for his valuable time and advice during all these years. Thank you very much for your support and for always find time in your busy schedule to answer all my doubts related with the research work and the regulations governing the management of doctoral studies.

Besides my supervisors, I wish to acknowledge the endless help and continuous support provided by Ekaitz Zulueta. From the very first moment he has always been ready to lend a hand, even in difficult times, and contributing with original ideas. Eskerrik asko. I am also particularly grateful for the help provided by Jose

Manuel López Guede, who contributed to spread this research work in conferences and taught me valuable advice on how to prepare and structure new scientific publications.

My sincere thanks also go to Miguel Angel and Alberto from the Department of Nautical Science and Marine Systems of the University of the Basque Country (UPV/EHU). Thank you for so many fruitful discussions in this long journey to design and manufacture these new prototypes. Thank you very much Miguel Angel for all your support. I would also like to express my very great appreciation to Mari Carmen and Vicky from the BioCruces Health Research Institute for always being willing to help me with the experimental part and for your positive energy. My special thanks are extended to Jon, from the Neonatal Intensive Care Unit of Hospital de Cruces. His immense knowledge in this research work, not only in medical terms but also in technical aspects, has helped me to advance in this research work.

This work would not have been possible without the financial support given by the University of the Basque Country UPV/EHU through the predoctoral grant and the funding by Consolidated Groups from the Basque Government. Technical and human support provided by IZO-SGI, SGIker (UPV/EHU) is gratefully acknowledged as well.

I would also like to acknowledge the assistance given by Estibalitz Goikoetxea. Her knowledge with CFD multiphase models and her large experience in the aerosol modelling was a great help during the development of the numerical study. I am also very grateful to Francisco Basterretxea from the Department of Physical Chemistry of the Faculty of Science and Technology (UPV/EHU). Thank you for your warm welcome in your laboratory in Leioa and the assistance given with the Aerodynamic Particle Sizer, which was essential to carry out all the experimental studies. I would also like to offer my special thanks to the company OPTIMUS 3D for the support in the manufacturing of the prototypes presented in this thesis, and especially to Izaskun, who got involved in this challenging manufacturing process

from the first moment.

My special thanks are extended to the Nuclear Engineering and Fluid Mechanics Department Professors Iñigo Errasti and Alberto Peña. Thank you Iñigo for your valuable advice and support during these years. I would also like to mention all the lecturers and members of the Faculty of Engineering of Vitoria-Gasteiz with whom I have been able to share good times and learned from them (Ana, Igor, Naiara, Borja, Ortzi, Leyre, Teo…). The assistance given by the administrative and technician staff of the university is also really appreciated. Thanks to all the PhD students I have met during the course of this thesis (Dani, Iosu, Pablo, Aitor, Arrate, Jon, Jose Mari). Never give up, your hard work will be rewarded!

Last but not least, I would like to thank my dear friends, who helped me to disconnect during the days off and for their encouragement, and of course to my family (parents, brother, sister-in-law, nephews…) for supporting me spiritually throughout writing this thesis and my life in general. Especially to my parents for their patience in hard moments, this journey would not have been possible if not for them, and I dedicate this milestone to them.

Resumen

Según la Organización Mundial de la Salud (OMS), cada año nacen de forma prematura alrededor de 15 millones de bebés, cifra que va en aumento, entre otros factores, por el incremento de técnicas de reproducción asistida o la cada vez mayor edad materna. Las complicaciones derivadas del nacimiento prematuro son la principal causa de mortalidad en niños menores de cinco años, responsables de aproximadamente 1 millón de muertes en 2015. En un nacimiento prematuro los bebés presentan complicaciones por la inmadurez de sus órganos, entre ellos los pulmones, los cuales presentan un déficit de surfactante pulmonar, siendo ésta la causa de la enfermedad conocida como **Síndrome de Distrés Respiratorio (SDR)**. Esta sustancia que recubre la superficie alveolar se genera de forma gradual a partir de las 22 semanas de gestación y su función es la de reducir la tensión superficial y, por consiguiente, la presión necesaria para la expansión del alveolo, facilitando la respiración.

El tratamiento empleado en la actualidad para el tratamiento del Síndrome de Distrés Respiratorio (SDR) en bebés prematuros conlleva riesgos que pueden causarles daños permanentes. Este tratamiento consiste en intubar al neonato para someterlo a ventilación mecánica y en administrarle surfactante pulmonar mediante instilación intratraqueal. Aunque este tratamiento reduce el índice de morbilidad y mortalidad, la instilación intratraqueal de surfactante está asociada con efectos adversos que pueden causar lesiones pulmonares y cerebrales. Con el objetivo de evitar o minimizar los riesgos de éste tratamiento se están investigando técnicas alternativas más seguras. Entre éstas técnicas, una posible alternativa con gran potencial es la **administración del surfactante en forma de aerosol**, simultaneándolo con un método de ventilación no-invasivo. Ello permitiría una mínima manipulación de las vías respiratorias del neonato y una administración del surfactante de forma menos agresiva. Hasta la fecha se han llevado a cabo diferentes estudios clínicos que han mostrado la seguridad y viabilidad de ésta técnica. Sin embargo, los resultados obtenidos son dispares, lo cual puede deberse, entre otros motivos, a las diferencias en el dispositivo empleado para generar el aerosol, el uso de distintas preparaciones de surfactante (natural vs sintético) o el emplazamiento del dispositivo nebulizador. El estudio de la administración de surfactante en forma de aerosol conlleva la investigación y desarrollo de **nuevos dispositivos de nebulización**. Concretamente los dispositivos de nebulización tipo 'jet', también denominados neumáticos o de chorro de aire.

El trabajo de esta tesis se ha desarrollado tanto en el campo experimental como en el campo numérico. Primero, se ha realizado un estudio experimental *in vitro* de una técnica de nebulización para generar aerosoles de forma menos invasiva en neonatos a través de un catéter de inhalación. También, se ha definido un modelo numérico, basado en técnicas CFD (Computational Fluid Dynamics) a través del código comercial STAR-CCM+, para su futura aplicación en la mejora del diseño del dispositivo nebulizador propuesto. Tras el diseño y fabricación del prototipo nebulizador mediante técnicas de fabricación aditiva, se ha llevado a cabo un estudio experimental para analizar las características en tamaño y masa de las gotas transportadas en el aerosol. Por último, se han establecido pautas para la optimización de nuevos diseños de nebulizadores y se ha realizado la fabricación de varios prototipos.

Inicialmente se llevó a cabo un **estudio experimental** con un dispositivo de nebulización ya existente, el catéter de inhalación IC-1.1 (Aeroprobe, Trudell Medical International). Destacar que el uso de este catéter estaba limitado para su

uso en investigación o experimentación en animales y que fue retirado del mercado. Este catéter tiene una longitud de 1 metro y está formado por un lumen central, por donde se suministra el compuesto a nebulizar, y por seis lúmenes exteriores por donde se introduce aire comprimido (Ver Figura 1). El estudio se ha realizado empleando tres diferentes compuestos; agua destilada (H_2Od), perfluorodecalina (PFD) y FC75. Estos dos últimos compuestos son perflurocarbonos (PFC), los cuales han demostrado su eficacia en diversos estudios para el tratamiento del SDR.

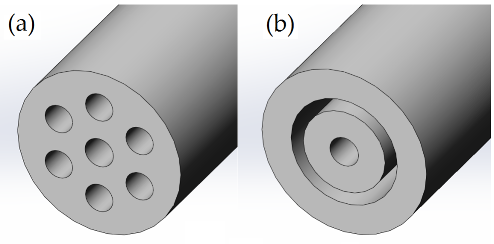

Figure 1: (a) Sección distal de la punta del IC-1.1 y (b) simplificación definida para la generación del dominio computacional axisimétrico.

Para la caracterización del tamaño y masa de las gotas generadas por el IC-1.1 se ha empleado un espectrómetro, concretamente el modelo APS 3321 con capacidad para medir partículas comprendidas entre 0-20 μm. Los parámetros que se han medido son el diámetro aerodinámico (D_a), el diámetro de la masa media aerodinámica (MMAD) y la desviación estándar geométrica (GSD). El D_a se define como el diámetro que tendría que tener la gota si fuera esférica y tuviera una densidad de 1 g/cm^3 para ir a la misma velocidad que la gota original. Por otro lado, el MMAD se define como el valor del diámetro aerodinámico que divide la masa del aerosol en partes iguales, es decir, el 50% de la masa del aerosol es transportada por gotas mayores o menores a ese valor. La GSD indica la dispersión del tamaño de las gotas. Si su valor es 1 significa que el aerosol está formado por gotas del mismo tamaño (aerosol monodisperso) mientras que un valor mayor que 1 indica que el aerosol está formado por gotas de diferentes tamaños (aerosol heterodisperso).

Los ensayos experimentales se han llevado a cabo con valores de presión entre 4 y 6 bares. Para cada compuesto y valor de presión se tomaron cinco muestras con un tiempo de muestreo para cada prueba de 10 segundos. Los resultados del D_a para el agua destilada mostraron un suave incremento proporcional a la presión mientras que los valores del MMAD variaban entre 10-11 μm. Por otra parte, para ambos PFCs, el valor del D_a descendió con un aumento de la presión de 4 a 5 bares. Respecto al MMAD, el PFD mostró valores estables con un incremento de presión. Sin embargo, el FC75 ofreció un descenso significativo en el valor del MMAD al aumentar la presión. En todos los casos se generaba un aerosol heterodisperso atendiendo a los resultados de la GSD. La Figura 2 recoge los resultados del valor medio del D_a y del MMAD obtenidos para cada compuesto.

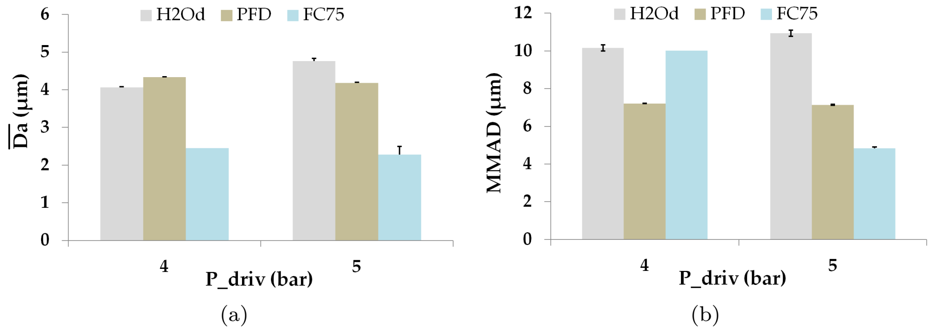

(a)

(b)

Figure 2: (a) Resultados del $\bar{D}_a$ y (b) MMAD obtenidos a la distancia óptima para cada compuesto y presión. Los valores están dados como media ± desviación estándar.

De forma complementaria al estudio experimental, se ha realizado un **estudio numérico con técnicas CFD** para estudiar las características del aerosol generado con el IC-1.1. Se ha definido un dominio computacional axisimétrico compuesto por los últimos 2 mm del IC-1.1 y la región aguas abajo del catéter. Para la definición de la fase discreta se han creado diez inyectores uniformemente distribuidos a lo largo de una línea de longitud igual al radio del lúmen central del IC-1.1 (34.3 μm). La velocidad de inyección de las gotas es igual a la velocidad de la fase continua en esa posición.

Tras el correspondiente estudio de dependencia de la malla, se ha generado un mallado no estructurado del dominio con un refinamiento en la región cercana a la punta del catéter y a lo largo de todo el eje central, donde se acumulará gran parte del aerosol. Para la resolución del flujo continuo de aire se ha utilizado el **enfoque euleriano**, mientras que para la resolución de las gotas del aerosol dispersas en el aire se ha empleado el **enfoque lagrangiano**. Se utilizaron las ecuaciones promediadas de Navier-Stokes para la resolución de los flujos turbulentos y más concretamente el modelo k-ϵ realizable. Del mismo modo, también se incluyó un modelo adicional para predecir la dispersión de la fase discreta por la turbulencia. Las trayectorias de las gotas inyectadas se resolvieron teniendo en cuenta la influencia de la fase discreta en el flujo continuo (two-way coupling) y el modelado de la rotura secundaria del aerosol se realizó a través del modelo Taylor Analogy Breakup. La Figura 3 ilustra la simulación del aerosol formado por el IC-1.1 para el compuesto FC75 y una presión de 4 bares. Para la validación de los resultados numéricos se han empleado los resultados experimentales realizados previamente.

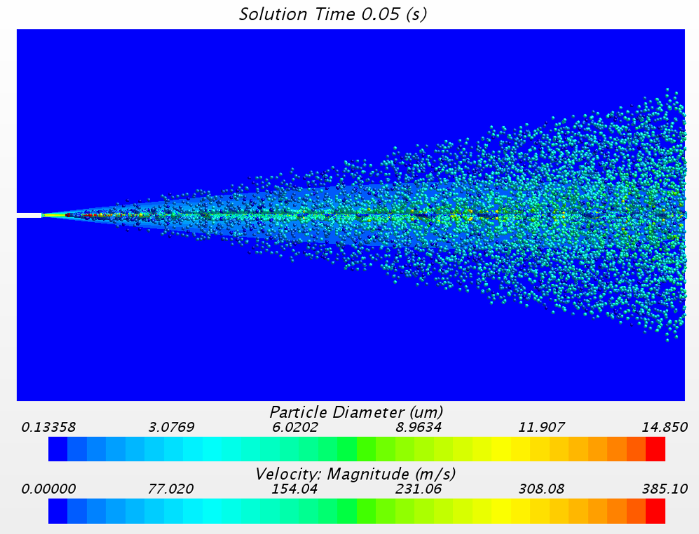

Figure 3: Visualización del aerosol de FC75 formado a una presión de 4 bares.

Este modelo numérico, desarrollado para la simulación del flujo de aerosol formado por el IC-1.1, servirá de base para futuros estudios computacionales con nuevos dispositivos nebulizadores como los que se presentan a continuación.

Inicialmente se ha estudiado la viabilidad y limitaciones actuales que ofrecen las **técnicas de fabricación aditiva** para el desarrollo de un prototipo nebulizador con capacidad para generar un aerosol de las características requeridas. Tras la realización de múltiples pruebas, se consideró la tecnología de impresión PolyJet como la solución óptima para llevar a cabo la fabricación de los dos prototipos propuestos. El diseño del **Prototipo 1** consiste en un lúmen central, por el que circula el compuesto a nebulizar, y seis lúmenes exteriores, por los que circula el aire comprimido. Por otro lado, en el **Prototipo 2**, los lúmenes exteriores han sido reemplazados por dos semi-anillos con un área equivalente. La Figura 4 muestra el resultado de la fabricación de los prototipos, con el detalle de la sección distal para cada uno de ellos.

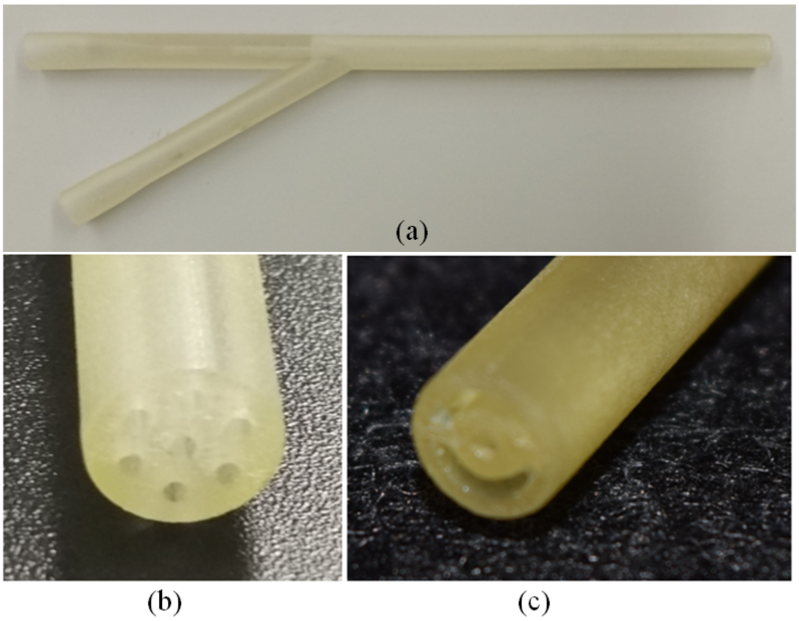

Figure 4: (a)Visualización general del prototipo nebulizador fabricado, detalle de la sección distal del (b) Prototipo 1 y (c) Prototipo 2.

Una vez fabricados los prototipos de forma satisfactoria se ha procedido a realizar una serie de **ensayos experimentales** con el objetivo de estudiar su funcionamiento y las características del aerosol generado. El montaje experimental empleado es similar al utilizado previamente en el estudio con el IC-1.1. Ambos prototipos han sido estudiados con agua destilada (H_2Od), PFD y FC75 y las propiedades del aerosol han sido estudiadas a través del D_a, el MMAD y el GSD.

Durante la nebulización de H_2Od, el MMAD de los aerosoles producidos con el Prototipo 1 proporcionó valores por debajo de 9 μm mientras que para el Prototipo 2 los valores del MMAD aumentaban hasta las 15 μm. En lo que respecta al D_a, los resultados obtenidos con el Prototipo 1 mantienen un valor estable independientemente de la presión aplicada mientras que para el Prototipo 2 se observó un ligero incremento en el valor del D_a proporcional a la presión.

La Figura 5 muestra los resultados del D_a y el MMAD obtenidos para los aresoles de PFD y FC75 producidos con cada uno de los prototipos. Con respecto al MMAD, los dos prototipos mostraron valores relativamente uniformes con ambos compuestos, cercanos a 12 μm, para los dos valores de presión estudiados (Ver Figura 5a). Los resultados del D_a de los aerosoles producidos con el Prototipo 2 fueron ligeramente menores que los obtenidos con el Prototipo 1, encontrándose en todos los casos por debajo de las 5 μm (Ver Figura 5b).

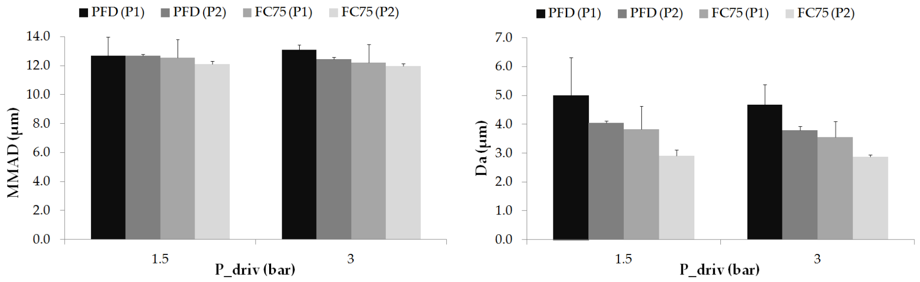

(a) (b)

Figure 5: (a) Valores del MMAD (μm) y (b) D_a (μm) para el Prototipo 1 y el Prototipo 2 en función de la presión aplicada con el compuesto PFD y FC75. Los valores están dados como media ± desviación estándar.

Tras los resultados obtenidos con estos dos prototipos, se han establecido las **directrices y pautas para la optimización del diseño del prototipo nebulizador**. Para ello, y teniendo en cuenta las limitaciones de la tecnología de fabricación aditiva empleada, se han propuesto una serie de modificaciones con el objetivo de mejorar el funcionamiento del prototipo y las características del aerosol generado.

A lo largo de este proceso se han fabricado cuatro nuevos prototipos que, al igual que con el Prototipo 1 y el Prototipo 2, fueron realizados en colaboración con la empresa OPTIMUS 3D. En el **Prototipo 4.2**, entre otros cambios, se ha modificado la longitud total del prototipo, se ha añadido un pequeño redondeo en la sección distal del semi-anillo por donde circula el aire comprimido y se ha incluido un estrechamiento en los últimos 2 mm del lúmen central con el objetivo de aumentar el tiempo del proceso de nebulización. Con este nuevo diseño se ha llevado a cabo un ensayo experimental con un neumotacógrafo para estudiar los valores de presión distal, ya que es de suma importancia que la presión intrapulmonar no supere los 10 cmH_2O. Trabajando con presiones máximas de 0.5 bares se consiguió un valor de presión distal de 5 cmH_2O y un tiempo de nebulización aproximado de cinco minutos y medio para los 5 ml de compuesto suministrado.

La siguiente etapa de optimización del diseño se centró en la mejora de la conectividad y manejo del prototipo nebulizador. Dada la fragilidad del material empleado para la fabricación de los prototipos, su conexión para el ensayo experimental era bastante delicada. Por ello, el **Prototipo 6** se fabricó conjuntamente con un **postizo roscado** para realizar la conexión por donde se suministra el compuesto a nebulizar. Adicionalmente, también se realizaron modificaciones en las dimensiones distales del prototipo. Una vez conseguida su fabricación de forma satisfactoria y realizadas pruebas experimentales se observó una obstrucción en el lúmen central y problemas de fabricación derivados por la limitación tecnológica para tal nivel de detalle.

Por dichos motivos, se decidió simplificar el diseño del prototipo nebulizador con el objetivo de reducir el número de variables que pueden afectar a la correcta fabricación del dispositivo, y por lo tanto, a su funcionamiento. Se han desarrollado dos últimos diseños (**Prototipo 8** y **Prototipo 9**) en los cuáles se ha eliminado el postizo conector y se ha aumentado el espesor de material entre el lúmen central y el semi-anillo. Adicionalmente se han rediseñado las pestañas que se incluyeron en ambas entradas del prototipo para mejorar su conexión dentro del montaje experimental. Ambos prototipos se consiguieron fabricar de forma satisfactoria y se comprobó que su funcionamiento era correcto y con potencial para generar un proceso de nebulización.

La presión aplicada al prototipo juega un papel determinante en el funcionamiento de los prototipos diseñados en la presente tesis. Por este motivo se ha implementado para futuros estudios un **sistema de control de presión** a través de dos válvulas proporcionales. Este sistema permite controlar en tiempo real tanto la presión aplicada al pistón situado dentro de la cámara de líquido como la presión de aire suministrado a través del semi-anillo.

Los resultados obtenidos mediante las técnicas desarrolladas en la presente tesis doctoral han sido publicados en varias revistas indexadas en la Journal Citation Report (JCR) de alto factor impacto. Asimismo, también se han presentado parte de los resultados en dos congresos internacionales (ver Apéndice B).

Contents

Acknowledgements **xv**

Resumen **xix**

List of Figures **xxxiii**

List of Tables **xxxix**

Acronyms **xliii**

Nomenclature **l**

1 INTRODUCTION **1**

1.1 Neonatal Respiratory Distress Syndrome 1

1.2 Pulmonary Surfactant 3

1.3 Current Medical Treatment 5

1.3.1 Surfactant Replacement Therapy 6

1.3.2 Ventilatory Support 10

1.4 State of the Art 12

1.4.1 Alternative Techniques of Surfactant Administration 12

1.4.1.1 INSURE Technique 12

1.4.1.2 Use of Perfluorocarbons 13

1.4.1.3 Minimally Invasive Surfactant Therapies (MIST) . 13

1.4.2 Aerosol Drug Delivery Devices 20

1.5 Application of CFD Techniques in Human Respiratory Airways . . 23

1.6 Thesis Motivation 26

1.7 Hypotheses 27

1.8 Objectives 28

1.9 Methodology 29

1.10 Contents and Structure of the Thesis 30

2 AEROSOL MODEL WITH INHALATION CATHETER 33

2.1 Experimental Model 33

2.1.1 Inhalation Catheter 33

2.1.2 Compounds Nebulized 34

2.1.3 Experimental Setup 35

2.1.4 Experimental Results 40

2.2 Numerical Model 45

2.2.1 Computational Domain and Boundary Conditions 47

2.2.2 Mesh Generation 51

2.2.3 Physics Models 54

2.2.3.1 Governing equations for the continuous phase . . . 54

2.2.3.2 Turbulence modeling 56

2.2.3.3 Discrete phase modeling: Lagrangian multiphase model 62

2.2.3.4 Droplet equations of motion 63

2.2.3.5 Turbulent dispersion 65

2.2.3.6 Secondary breakup 66

2.2.3.7 Interaction between continuous phase and dispersed phase 69

2.2.4 Numerical Procedure 70
2.2.5 Temporal and Discrete Phase Discretization 73
2.2.6 Continuous and Discrete Phase Simulation Results 75
2.2.7 Convergence Criteria 77
2.2.8 Validation of the Numerical Model 79
2.2.9 Conclusions 80

3 NEBULIZER PROTOTYPE DESIGN 83

3.1 Additive Manufacturing Techniques in Medical Applications 83
3.1.1 Additive Manufacturing Technologies 85
3.2 Application of 3D Printing Techniques to Manufacture a Nebulizer Prototype 87
3.2.1 Prototypes Manufacturing with PolyJet Technology 88
3.3 Experimental Setup with the Prototypes 94
3.4 Experimental Results with Distilled Water 97
3.5 Experimental Results with PFCs: PFD and FC75 99
3.6 Discussion and Conclusions 103

4 OPTIMIZATION OF NEBULIZER PROTOTYPE 107

4.1 Guidelines to Optimize the Design of the Nebulizer Prototype . . . 107
4.2 Design and Manufacturing of Prototype 4 108
4.3 Design and Manufacturing of Prototype 6 114
4.4 Design and Manufacturing of Prototype 8 and Prototype 9 117

5 CONCLUSIONS AND FUTURE WORK 121

5.1 Conclusions 121
5.2 Future Work 123
5.2.1 CFD Studies with the Nebulizer Prototypes 123
5.2.2 Pressure Control System 124
5.2.3 Digitalization of a Real Trachea Geometry 126

Appendices 131

A Nebulizer Prototypes Designs 131

B Publications and Conferences 141

B.1 Publications 141

B.2 Conferences 143

B.3 Book chapters 144

Bibliography 145

List of Figures

1.1 Human respiratory tract from the upper airways to the alveolar region 3

1.2 Reduced compliance of preterm infant suffering from RDS in comparison to a healthy term newborn baby. 5

1.3 Surfactant influence in the alveoli stability. 6

1.4 (a) Endotracheal tube with a catheter to instill the surfactant and (b) endotracheal tube position within the trachea. 7

1.5 Deposition mechanisms of particles in the respiratory tract. 19

1.6 Scheme of a Pressurized metered dose inhaler (pMDI). 21

1.7 Schematic of a conventional jet nebulizer 22

1.8 (a) *Saint* model of a 9 month-old infant upper airways and (b) nasal airways model from a 6 month-old infant 25

1.9 Flow chart of the methodology used. 29

2.1 Inhalation catheter (IC 1.1) with a cross section detail of the distal end. 34

2.2 Experimental setup used for the particle size characterization of the droplets generated with the IC-1.1. 36

2.3 Aerodynamic Particle Sizer (APS) Model 3321. 36

2.4 (a) Aerodynamic Particle Sizer (APS) operation scheme, (b) detail view with aerosol droplets crossing the overlapping beams and generating the double-crested signal. 37

2.5 Percentage of droplets classified in each event for one sample. . . . 38

2.6 Air pressure controller. 39

2.7 Distribution of compressed air to the piston of the liquid chamber and to the side connection of the IC-1.1. 39

2.8 Alignment of the IC-1.1. 40

2.9 (a) $\bar{\mathrm{D}}_a$ and (b) MMAD results obtained at the optimal distance for each compound and driving pressure. Values are given as mean ± standard deviation. 45

2.10 CFD analysis framework and the interconnectivity functions of the three main elements involved. 46

2.11 (a) Cross section of the IC-1.1 tip and (b) the assumption defined for the generation of the axisymmetrical computational domain. . . 47

2.12 Transformation of the six outer lumens into an outer ring to carry out the numerical study. 49

2.13 Computational domain and boundary conditions. 49

2.14 Mesh generated by means of polygonal cells and with a mesh refinement all along the central axis. 53

2.15 Subdivisions of the near-wall treatment. 61

2.16 Illustration of the droplet distortion. 67

2.17 (a) One-way coupling and (b) Two-way coupling interaction. 69

2.18 Numerical procedure followed for the resolution with the Coupled Flow model. 70

2.19 Steps carried out to run the numerical simulations. 71

2.20 Scheme of domain decomposition approaches. 73

2.21 Discrete phase dependency study. 75

2.22 Continuous-phase velocity magnitude with a pressure of P=4bar. . 76

2.23 Continuous-phase velocity magnitude with a pressure of P=5bar. . 76
2.24 Particle size distribution of the FC75 discrete droplets with a driving pressure of 4 bar. 77
2.25 Coordinates of the point chosen to monitor the evolution of the axial air velocity. 78
2.26 Axial air velocity values with pressures of 4 bar and 5 bar, considered to confirm the convergence of the numerical solution. 78
2.27 Experimental and numerical axial air velocity profiles at different distances from the IC-1.1 tip. 79
2.28 Experimental and numerical cumulative mass distribution based on droplet size for the PFD compound. 80
2.29 Experimental and numerical cumulative mass distribution based on droplet size for the FC75 compound. 80

3.1 Steps involved in the configuration and programming of the preprinting process. 84
3.2 Eight-generation neonate airway model created with additive manufacturing techniques 85
3.3 (a) Distal geometry dimensions of Prototype 1 and (b) Prototype 2. 88
3.4 (a) Stratasys Objet30 Pro 3D printer and (b) its specifications. . . 89
3.5 Definition of the tolerance cylinders to facilitate the extraction of the support material. 90
3.6 Preliminary tests carried out with the Objet30 Pro 3D printer. . . 91
3.7 (a) Stratasys Objet30 Pro 3D printer and (b) its specifications. . . 92
3.8 (a) General visualization of the nebulizer prototype design proposed, distal section of (b) Prototype 1, (c) Prototype 2. Manufacturing result of Prototype 1 (d), distal section detail of the manufactured (e) Prototype 1 and (f) Prototype 2. 93
3.9 Experimental setup used for the particle size characterization with the nebulizer prototypes. 94

3.10 (a) Air cylinder shoulder with the pressure reducer included and (b) detail of the connections to the air pressure controller. 95

3.11 (a) Setup of the nebulizer with the liquid chamber where the liquid is supplied and (b) detail of the connections to administer the compressed air and the liquid respectively. 96

3.12 (a) MMAD (μm) and (b) D_a (μm) values for Prototype 1 and Prototype 2 as a function of the driving pressure for distilled water (H_2Od). Values are given as mean ± standard deviation. 97

3.13 Mass and number distribution of an H_2Od aerosol sample with Prototype 1 (left) and Prototype 2 (right). (Screenshots taken directly from the Aerosol Instrument Manager software). 99

3.14 (a) MMAD (μm) and (b) D_a (μm) values for Prototype 1 and Prototype 2 as a function of the driving pressure for PFD and FC75. Values are given as mean ± standard deviation. 100

3.15 Mass and number distribution of a PFD aerosol sample with Prototype 1 (left) and Prototype 2 (right). 102

3.16 Mass and number distribution of a FC75 aerosol sample with Prototype 1 (left) and Prototype 2 (right). 102

3.17 (a) Nebulization case with Prototype 1 and (b) with Prototype 2. . 103

4.1 Distal section of Prototype 4.1. 108

4.2 Distal sections of the different designs proposed for the Prototype 4. (a) Prototype 4.2, (b) Prototype 4.3, (c) Prototype 4.4 and (d) Prototype 4.5. (All dimensions are given in milimeters.) 109

4.3 Prototype 4.2 distal dimensions. 110

4.4 Result of the manufactured Prototype 4.2 by additive manufacturing techniques. 110

4.5 Prototype 4.2 connected in an open circuit. 111

4.6 Prototype 4.2 connected in a close circuit. 112

4.7 Prototype 4.2 connected in an open circuit with the addition of an adapter of reduced cross section. 113
4.8 Threaded connector geometry and dimensions. 114
4.9 Threaded connector manufactured with additive manufacturing techniques. 115
4.10 Prototype 6 distal dimensions. 116
4.11 Result of the manufactured Prototype 6 by additive manufacturing techniques. 116
4.12 Wall thickness between the air chamber (highlighted in magenta color) and the central lumen (highlighted in green color) defined in Prototype 6. 117
4.13 (a) New wall thickness of 0.70 mm defined in Prototype 8 and (b) their distal dimensions. 118
4.14 (a) Result of the manufactured Prototype 8 by additive manufacturing techniques, (d) details of the small tabs placed in the connections and (c) distal section. 119
4.15 Distal section of the manufactured Prototype 9. 120
4.16 (a) Result of the manufactured Prototype 9 by additive manufacturing techniques, (d) details of the small tabs placed in the connections and (c) distal section. 120

5.1 Operating principle. 124
5.2 Experimental setup with the Sentronic valves. 125
5.3 Prototype connected with Sentronic valves. 126
5.4 Digitalization process to obtain the 3D geometry 127

List of Tables

1.1 Surfactant preparations and recommended doses. 9

2.1 Properties of H_2Od and PFCs. 35

2.2 H_2Od experimental results with driving pressures of P=4 bar and P=4.5 bar. 41

2.3 H_2Od experimental results with driving pressures of P=5 bar and P=6 bar. 42

2.4 PFD experimental results at h=30mm with driving pressures of P=4 bar and P=5 bar. 43

2.5 PFD experimental results at h=46mm with driving pressures of P=4 bar and P=5 bar. 43

2.6 PFD experimental results at h=60mm (optimal distance) with driving pressures of P=4 bar and P=5 bar. 44

2.7 FC75 experimental results at h=52mm (optimal distance) with driving pressures of P=4 bar and P=5 bar. 44

2.8 Droplet initial conditions for PFD and FC75 compounds obtained from experimental measurements. 51

2.9 Axial velocity values in the chosen point for each mesh level. . . . 52

2.10 Errors obtained for each mesh level. 53

2.11 Grid Convergence Index (GCI) results. 53

3.1 Material properties. 92

3.2 Properties of H_2Od and PFCs. 94

3.3 Geometric standard deviation (GSD) for both prototypes nebulizing H_2Od at different pressures. Values are given as mean ± standard deviation. 98

3.4 Geometric standard deviation (GSD) for both prototypes nebulizing PFD and FC75 at different pressures. Values are given as mean ± standard deviation. 101

4.1 Distal pressures obtained with each prototype in an open circuit. . 112

Acronyms

ABS	**A**crylonitrile **B**utadiene **S**tyrene
APS	**A**erodynamic **P**article **S**izer
BPD	**B**roncho**p**ulmonary **D**ysplasia
CFD	**C**omputational **F**luid **D**ynamics
CFL	**C**ourant **F**riedrichs **L**ewy number
CPAP	**C**ontinuous **P**ositive **A**irway **P**ressure
CPU	**C**entral **P**rocessing **U**nit
DAS	**D**ata **A**cquisiton **S**oftware
DNS	**D**irect **N**umerical **S**imulation
DPI	**D**ry **P**owder **I**nhaler
DPPC	**Dip**almitoyl **P**hoshatidyl**c**holine
EMP	**E**ulerian **M**ulti**P**hase model
EVM	**E**ddy **V**iscosity **M**odels
FDM	**F**used **D**eposition **M**odeling
FVM	**F**inite **V**olume **M**ethod

GCI	**G**rid **C**onvergence **I**ndex
H_2Od	**D**istilled **W**ater
HFNC	**H**igh **F**low **N**asal **C**annula
HPC	**H**igh **P**erformance **C**omputing
IC	**I**nhalation **C**atheter
INSURE	**In**halation **S**urfactant **E**xtubation
LES	**L**arge **E**ddy **S**imulation
LISA	**L**ess **I**nvasive **S**urfactant **A**dministration
LMP	**L**agrangian **M**ulti**P**hase model
MIST	**M**inimally **I**nvasive **S**urfactant **T**herapy
MJF	**M**ulti **J**et **F**usion
MV	**M**echanical **V**entilation
NAVA	**N**eurally **A**djusted **V**entilatory **A**ssist
NIPPV	**N**asal **I**ntermittent **P**ositive **P**ressure **V**entilation
PFC	**P**er**f**luoro**c**arbon
PFD	**P**er**f**luoro**d**ecalyn
PIP	**P**eak **I**nspiratory **P**ressure
pMDI	**p**ressurized **M**etered **D**ose **I**nhaler
RANS	**R**eynolds **A**verage **N**avier **S**tokes
RDS	**R**espiratory **D**istress **S**yndrome
RR	**R**espiratory **R**ate
RSTM	**R**eynolds **S**tress **T**ransport **M**odels
SLA	**St**ereolithography
SLM	**S**elective **L**aser **M**elting

SLS	**S**elective **L**aser **S**intering
TAB	**T**aylor **A**nalogy **B**reakup
VOF	**V**olume **O**f **F**luid model
WHO	**W**orld **H**ealth **O**rganization

Nomenclature

A_p	Projected area of the droplet	[m^2]
b_{lcen}	Distance between centers of outer and central lumens of the IC-1.1	[μm]
c	Speed of sound	[m/s]
c_p	Specific heat for constant pressure	[J/(kg·K)]
c_v	Specific heat for constant volume	[J/(kg·K)]
C_b, C_d, C_k	Empirical constant of the TAB model	[-]
C_D	Drag coefficient	[-]
C_v	Normal velocity coefficient	[-]
$C_{\epsilon 1}$, $C_{\epsilon 2}$, C_μ	K-ϵ turbulent model coefficients	[-]
d	Diameter of the outer lumens of the IC-1.1	[μm]
D_{32}	Sauter mean diameter	[m]
D_a	Aerodynamic diameter	[μm]
$\bar{D}_a$	Mean aerodynamic diameter	[μm]
D_{a1}	Aerodynamic diameter measured with the APS	[μm]

D_{a2}	Aerodynamic diameter with the Stokes correction	[μm]
D_g	Geometric diameter	[μm]
D_p	Droplet diameter	[m]
e	Specific internal energy	[J/kg]
f_c	Curvature correction factor	[-]
F_b	Resultant of the body forces that act on a droplet	[N]
F_D	Drag force	[N]
F_p	Pressure gradient force	[N]
F_{vm}	Virtual mass force	[N]
F_s	Resultant of the forces that act on the surface of a droplet	[N]
F	Source terms that model the exchange of momentum with the discrete phase	[N]
G_k	Production term to represent the turbulent production in the k-ϵ turbulence model	[kg/(m·s^3)]
GSD	Geometric Standard Deviation	[-]
h	Specific enthalpy	[J/kg]
h	Distance between the IC-1.1 and the APS inlet nozzle	[mm]
h_3, h_2, h_1	Coarse, medium and fine mesh levels	[-]
k	Turbulent kinetic energy	[m^2/s^2]
K	Ratio of the total energy in distortion and oscillation to the energy in the fundamental mode	[-]
l_ϵ	Length scale function	[m]

l_t	Length scale of the turbulence	[m]
L	Length of the computational domain	[mm]
L	Characteristic linear dimension to calculate the Reynolds number	[m]
$\dot{m}$	Liquid mass flow rate	[kg/s]
$\dot{m}_{air}$	Air mass flow rate	[kg/s]
m_p	Mass of a material droplet	[kg]
Ma	Mach number	[-]
$MMAD$	Mass Median Aerodynamic Diameter	[μm]
p	Order of convergence	[-]
P	Pressure	[bar]
P_{alv}	Alveolar pressure	[bar]
P_{driv}	Driving pressure	[bar]
Q	Source terms that model the exchange of energy with the discrete phase	[W]
r	Mesh refinement ratio	[-]
r_1	Inner radius of the ring	[μm]
r_2	Outer radius of the ring	[μm]
r_{alv}	Alveoli radius	[μm]
R	Ideal gas constant	[J/(mol·K)]
Re	Reynolds number	[-]
Re_d	Droplet Reynolds number	[-]
s_{ij}	Instantaneous strain-rate tensor	[s^{-1}]
S_{ij}	Mean strain-rate tensor	[s^{-1}]

t	Time	[s]
t_{ij}	Instantaneous viscous stress sensor	[Pa]
T	Temperature	[K]
T_0	Specific time-scale	[s]
T_ϵ	Large-eddy time scale	[s]
u	Velocity magnitude	[m/s]
u, v, w	Continuous flow velocity components	[m/s]
u^+, y^+	Dimensionless values used in the wall treatment	[-]
u_τ	Friction velocity	[m/s]
U	Mean flow velocity	[m/s]
U	Air flow velocity through the APS nozzle	[cm/s]
$v^{'}$	Eddy velocity fluctuation	[m/s]
$\bar{v}$	Reynolds-averaged velocity	[m/s]
v_{axial}	Axial air velocity	[m/s]
v_p	Instantaneous droplet velocity	[m/s]
v_{rel}	Relative velocity between the droplet and the air	[m/s]
V	Average droplet velocity measured with the APS	[cm/s]
We	Weber number	[-]
We_{crit}	Critical Weber number	[-]
x	Ring width to define the axisymmetrical condition	[μm]
x	Instantaneous displacement of the droplet equator from its equilibrium position	[m]
y	Distance from the wall	[m]

$\dot{y}_b$	Rate of distortion at the instant of breakup	[-]
Y_M	Production term to represent the compressibility modification in the k-ϵ turbulence model	[m^2/s^3]

GREEK SYMBOLS

α	Under-relaxation factor of the two-way coupling solver	[m/s]
Δx	Length interval	[m]
Δt	Time step	[s]
ϵ	Turbulent dissipation rate	[m^2/s^3]
ϵ_0	Ambient turbulence value in the source terms that counteracts turbulence decay	[m^2/s^3]
κ	Thermal conductivity	[W/(K·m)]
μ_t	Turbulent eddy viscosity	[kg/(m·s)]
μ_l	Droplet viscosity	[Pa·s]
ν	Kinematic viscosity	[cSt]
ρ	Density	[g/ml]
ρ_0	Unit density	[g/ml]
ρ_{air}	Air density	[g/ml]
$\rho_{droplet}$	Droplet density	[g/ml]
ρ_{FC75}	FC75 droplet density	[g/ml]
ρ_{PFD}	PFD droplet density	[g/ml]
ρ_{PSL}	Polystyrene latex particles density	[g/cm^3]
σ	Surface tension	[dyn/cm]
σ_k, σ_ϵ	K-ϵ turbulent model coefficients	[-]

τ_e	Eddy time scale	[s]
τ_t	Time scale of the turbulence	[s]
τ_v	Momentum relaxation time scale	[s]
τ_w	Wall shear stress	[Pa]
υ	Characteristic velocity of the object relative to the fluid to calculate the Reynolds number	[m/s]
ϕ	Flow variable	
$\bar{\phi}$	Flow variable average	
$\phi^{'}$	Flow variable fluctuation	
ϕ_c	Volume fraction of a Lagrangian phase	[-]
$\sum \phi$	Sum of the volume fractions of the relevant Lagrangian phases	[-]

CHAPTER 1

INTRODUCTION

1.1 Neonatal Respiratory Distress Syndrome

According to the World Health Organization (WHO), every year an estimated 15 million babies are born preterm, i.e. before 37 completed weeks of gestation, and this number is rising over the years due to several factors. Recently, Arroyo et al. [1, 2] studied the impact of air pollution on low birth weight in Spain and concluded that 1.35% of premature births that ocurred in Spain can be attributed to air pollution. There are sub-categories of preterm birth, based on gestational age: moderate to late preterm babies born between 32 and 37 completed weeks, very preterm babies born between 28 and 32 completed weeks and extremely preterm babies born earlier than the 28th week of the gestational age. Respiratory distress syndrome (RDS) of the newborn is the leading cause of death in premature infants [3]. Extremely and very preterm infants present cerebral and pulmonary issues due to the immaturity of the lungs, primarily due to lack of surfactant, a natural substance indispensable to breath. The respiratory tract esentially consists of a series of bifurcating pipes, with the pipes becoming smaller and smaller towards the alveolar region, where it takes place the gas exchange.

The risk and severity of respiratory distress syndrome is inversely proportional to the gestational age of infant birth. Young gestational age and very low birth weight (from 1001 to 1500g), or extremely low birth weight (from 500 to 1000g), respectively, are the biggest risk factors for RDS. There are also others risk factors for developing RDS, such as maternal diabetes, multiple births, male sex or second twin. For instance, RDS does not affect sex and races equally. Males are more predisposed than females, although the exact physiological cause is not yet understood. In the study of Miller et al. [4], the RDS incidence was more than three times higher in boys than in girls. Black fetuses, historically, have had a lower incidence of RDS and develop surfactant faster than white fetuses [5].

Any preterm newborn displaying some of these symptoms should be considered highly suspect for having RDS:

- Abnormal breathing patterns (such as tachypnea or apnea).
- Grunting (occurring during each exhalation by breathing against a partially closed glottis).
- See-saw breathing pattern (the stomach and chest are moving out of synch during breathing attempts).
- Substernal and/or intercostal retractions.
- Nasal flaring.
- Hypoxemia (low level of oxygen in the blood).
- Hypercarbia (high level of carbon dioxide in the blood).
- Cyanosis (appearance of blue or purple coloration of the skin).
- Atelectasis (collapse or closure of a lung resulting in reduced or absent gas exchange).

If the RDS remains on time, other adversities can be reported as bronchopulmonary dysplasia (BPD) [6], pulmonary hemorrhage, pneumothorax [7] or pulmonary vasoconstriction.

1.2 Pulmonary Surfactant

Three basic regions can be defined in the respiratory tract. Figure 1.1 shows the structure and elements of the respiratory system.

1. The extrathoracic region (also referred as 'upper airways'), which includes the oral cavity, the nasal cavity and the larynx (containing the vocal cords).
2. The tracheo-bronchial region (also referred as 'lower airways'), containing the trachea and the bronchi until the so-called 'terminal bronchioles'.
3. The alveolar region.

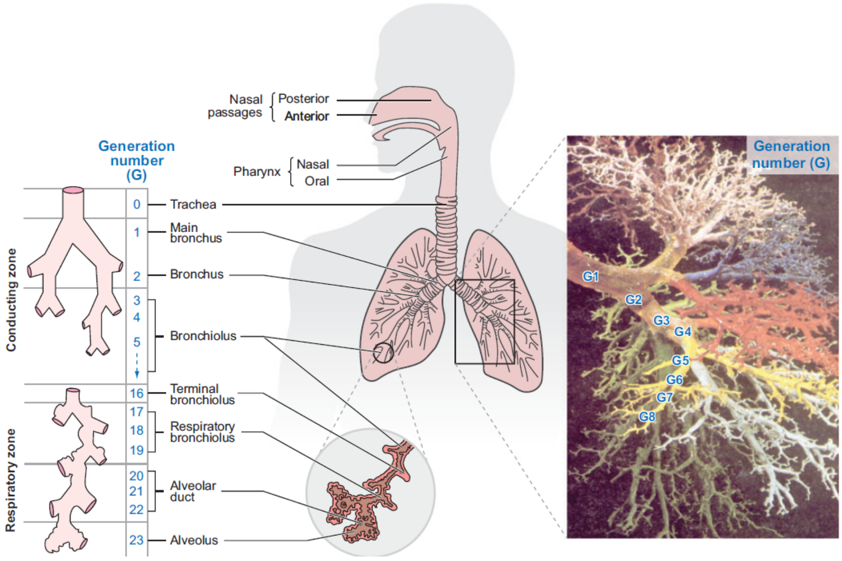
Nasal passages
Posterior
Anterior
Generation number (G)
Pharynx
Nasal
Oral
Trachea
Main bronchus
Bronchus
Bronchiolus
Terminal bronchiolus
Respiratory bronchiolus
Alveolar duct
Alveolus
0
1
2
3
4
5
16
17
18
19
20
21
22
23
Conducting zone
Respiratory zone
Generation number (G)
G1
G2
G3
G4
G5
G6
G7
G8

Figure 1.1: Human respiratory tract from the upper airways to the alveolar region. Source: Kleinstreuer et al. [8].

The alveoli are coated with pulmonary surfactant which is secreted by the type II alveolar cells. It reduces the surface tension and, therefore, it prevents the alveolar collapse at the end of the exhalation, retaining enough air (functional residual capacity) to start the next breath. Without the surfactant the surface tension at the alveoli would remain high and they would collapse.

Surfactant is a complex substance which appears in fetal development during the saccular phase (gestation weeks 24 to 34) and whose major components are lipids (90%) and proteins (10%) [9]. Most of the lipids are phospholipids being the dipalmitoylphosphatidylcholine (DPPC) the predominant one and the main component responsible for decreasing the surface tension. The proteins consist of four unique surfactant-associated proteins: SP-A, SP-B, SP-C and SP-D. Two of them (SP-A and SP-D) are hydrophilic proteins involved in pulmonary host defense [10] and the other two (SP-B and SP-C) play an intricate role in sustaining alveolar ventilation [11]. Parra and Pérez-Gil [12] made a detailed review of the composition, structure and properties of the surfactant and problems due to its inactivation. The pulmonary surfactant have three main functions:

1. Increase the pulmonary compliance.
2. Prevent the collapse of the lung at the end of expiration (atelectasis) by reducing the surface tension at the air-liquid interface of the alveolus.
3. Facilitate the recruitment of collapsed airways.

The lung compliance, which describes how volume changes for a given change in pressure, is an important parameter to check if the newborn has respiratory problems, taking into account that surfactant deficiency reduces this parameter as shown in Figure 1.2 [13]. The behavior of the alveoli is largely dictated by Laplace's Law, which relates the alveolar pressure, the surface tension and the alveoli radius by the Equation 1.1.

$$P_{alv} = \frac{2\sigma}{r_{alv}} \tag{1.1}$$

The surfactant capacity to reduce the surface tension allows to maintain the same alveolar internal pressure and, therefore, prevents the collapse. In cases of surfactant deficiency the surface tension remains high for all the alveoli and, according to the Laplace Law expressed by the Equation 1.1, the pressure in the smaller ones is higher. That means that the air is going from the smaller alveoli to a bigger one, causing the collapse of the first one at the end of the expiration. This

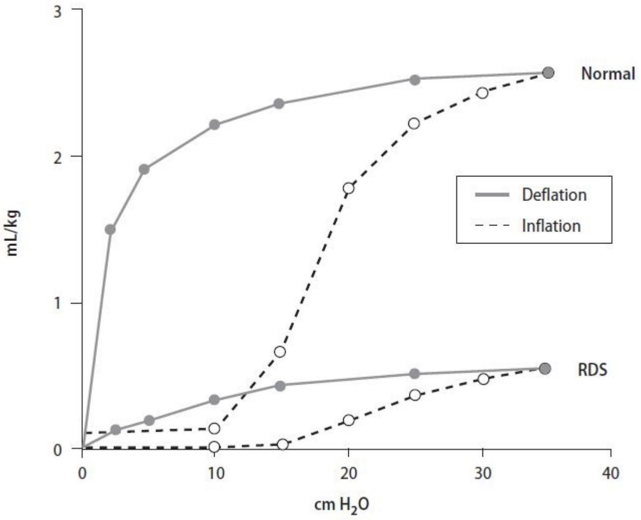

Figure 1.2: Reduced compliance of preterm infant suffering from RDS in comparison to a healthy term newborn baby. Source: Kramer et al. [13].

directly affects to the gas exchange produced in the alveolar region, the carbon dioxide increase (hypercarbia) and the oxygen supply decrease (hypoxia).

1.3 Current Medical Treatment

The nowadays known as RDS was first characterized in the early 20th century as hyaline membrane disease because most physicians in that time thought that newborn's death cause was the hyaline membranes which were found in their lungs at autopsy. However, in 1959 Avery and Mead [14] discovered that the surfactant deficiency was the responsible of this disease. This finding gave a chance to further studies and to develop the surfactant replacement therapy.

The treatment can start even before the delivery, with the use of antenatal corticosteroids in women at risk of preterm birth. Corticosteroids accelerate the surfactant development and the fetal lung maturation. Reviews of the literature show that a repeated dose of prenatal corticosteroids given to women who remain

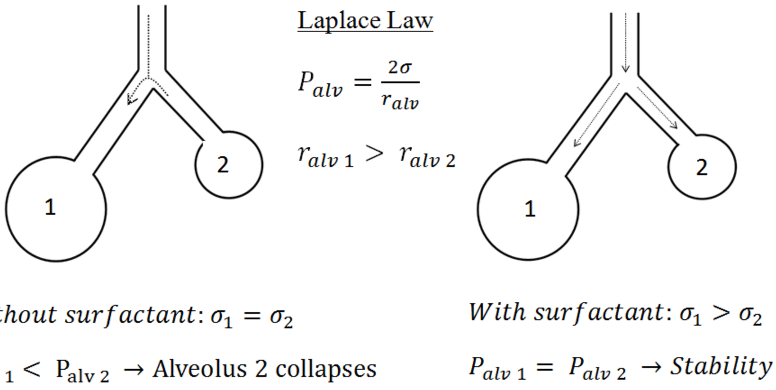
Laplace Law
$P_{alv} = \frac{2\sigma}{r_{alv}}$
$r_{alv\,1} > r_{alv\,2}$
1
2
1
2
$Without\ surfactant: \sigma_1 = \sigma_2$
$P_{alv\,1} < P_{alv\,2}$ → Alveolus 2 collapses
$With\ surfactant: \sigma_1 > \sigma_2$
$P_{alv\,1} = P_{alv\,2}$ → Stability

Figure 1.3: Surfactant influence in the alveoli stability.

at risk of an early birth helps the baby's lungs and reduces serious health problems in the first few weeks of life [15]. Nevertheless, there is currently no clear or agreed-upon best type of corticosteroid or dose. After delivery, the treatment includes the instillation of surfactant as well as ventilatory support techniques depending on the gestational age of the newborn and its clinical state.

1.3.1 Surfactant Replacement Therapy

In 1929, Von Neergaard [16] showed that more pressure was required to inflate lungs with air than with an aqueous solution like water. Throughout the Young-Laplace Law (Equation 1.1), he found that surface tension at the boundary of the moist tissue of the lung and the air was the reason for the difference in pressure needed for the lungs to expand. In 1955, Pattle [17] speculated that *'absence of the lining substance may sometimes be one of the difficulties with which a premature baby has to contend'*. In 1959, Avery and Mead discovered that RDS was caused by the absence of surfactant [14]. Just four years later, in 1963, the United States President John F. Kennedy's son death, due to RDS, two days after he was born, put a new focus on diseases of the newborn. Since then, different studies were carried out in order to find a treatment. In 1969 Robillard et al. [18] and later

Shannon and Bunnell [19] treated a small number of infants, but their results did not encourage them to continue these studies. Enhorning and Robertson in 1972 [20] showed a significant improvement in pulmonary mechanics using surfactant in prematurely born rabbit pups. It was not until 1980 when Fujiwara et al. [21] made the first successful clinical study with the **surfactant replacement therapy**. Some years later, in 1990, after an intense study and development, the guidelines on the management of surfactant replacement therapy were published and are constantly being updated after critical examination of the most up-to-date evidence available [22]. The aim of this management is to provide interventions that will maximize survival whilst minimizing potential adverse effects resulting in a considerably decrease on chronic lung diseases. The therapy consists in the introduction of exogenous surfactant (surfactant originated outside the lungs) in the preterm infant lung. Usually bovine or porcine natural surfactant administered by intratracheal instillation (also called *bolus*) through an endotracheal tube as the one illustrated in Figure 1.4a.

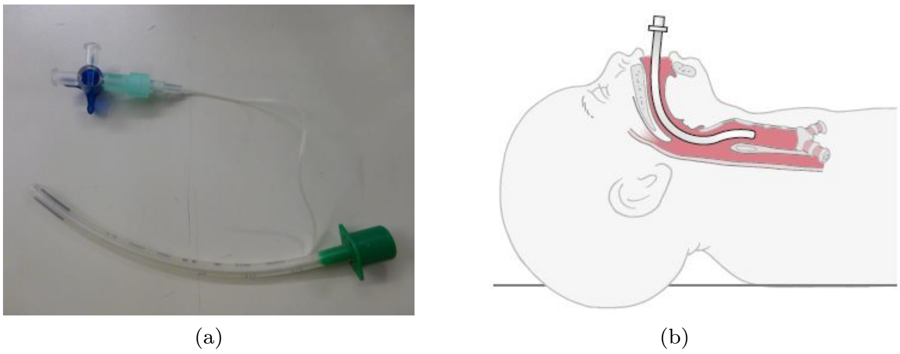

(a) (b)

Figure 1.4: (a) Endotracheal tube with a catheter to instill the surfactant and (b) endotracheal tube position within the trachea [23].

McDonald and Ainsworth [24] summarized information about the type of surfactant and dose recommended as well as the surfactant benefits in other neonatal lung diseases. Recently, Polin et al. [25] made a clinical report reviewing a number of important topics surrounding the use of surfactant, including prophylactic versus rescue replacement and preparations and administration techniques.

There are several types of surfactant preparations licensed for use in babies with RDS (See Table 1.1). Nowadays the guideline recommends the use of natural surfactant, instead of synthetic, as early as possible in the course of RDS. Ma et al. [26] summarized the results of a number of trials comparing natural versus synthetic surfactants and trials comparing different natural surfactants. It was also reported a survival advantage with higher initial doses of natural surfactant (200mg/kg better than 100mg/kg using poractant alfa) and a fewer requirement of a second dose [27]. Recently, Tridente et al. [28] performed a review to compare the efficiency between porcine and bovine surfactant to treat RDS in preterm infants. Their results showed that 200 mg/kg of poractant alfa is associated with better respiratory outcomes compared to bovine surfactants. Although there are a number of barriers involved in the development of a protein-containing synthetic surfactant, the quest to find a suitable preparation continues. It would present some advantages as the capacity to produce surfactant in large quantities, a cost reduction compared with natural surfactant and the opportunity to control its composition in order to reduce the risk of transmission of infections.

The timing of surfactant replacement therapy has been a controversial topic and research. There are two main strategies for initiation of surfactant replacement.

- **Prophylactic strategy**

  Therapy begins as soon as possible in newborns at high risk for developing RDS. This method has been shown to decrease the need for mechanical ventilation (MV) and lower the incidence of BPD and death.

- **Rescue strategy**

  Therapy begins when it exists a clear evidence of RDS. Evidences include oxygen requirements, and/or a chest radiography with characteristic RDS features. The benefit of this option includes the potential to avoid intubation in some patients and less time on MV.

Generic name	**Trade name**	**Source**	**Dose (Volume)**
Pumactant	ALEC	Synthetic	No longer manufactured
Bovactant	Alveofact	Bovine	50 mg/kg/dose (1.2 ml/kg)
Bovine lipid extract surfactant	BLES	Bovine	135 mg/kg/dose (5 ml/kg)
Poractant alfa	Curosurf	Porcine	100-200 mg/kg/dose (1.25-2.5 ml/kg)
Colfosceril palmitate	Exosurf	Synthetic	64 mg/kg/dose (5 ml/kg)
Calfactant	Exosurf	Synthetic	64 mg/kg/dose (5 ml/kg)
Surfactant-TA	Surfacten	Bovine	105 mg/kg/dose (3 ml/kg)
Lucinactant	Surfaxin	Synthetic	Not licensed
Beractant	Survanta	Bovine	100 mg/kg/dose (4 ml/kg)

Table 1.1: Surfactant preparations and recommended doses.

The surfactant replacement therapy has been proven effective but it also presents some important drawbacks. The main issue is that it requires the intubation of the newborn and the application of ventilatory support techniques, as mechanical ventilation, which may induce lung injuries and/or chronic diseases even in short periods of application. Other drawbacks are the impossibility to interact with the patient, a newborn, to execute the intubation maneuver and the administration of the dose in bolus form, that may affect cerebral and systemic hemodynamic parameters [29]. The bolus can also clogged the endotracheal tube and/or the upper airways, contributing to an oxygen deficiency and an increase in carbon dioxide values. Obladen and Halliday [30, 31] summarized the history of surfactant up to 1980 and from 1980 respectively, with the most important landmarks in the research of the RDS disease and its treatment.

1.3.2 Ventilatory Support

The aim of ventilatory support in neonates is the same as for any other patient. Facilitate alveolar ventilation, improve gas exchange, and reduce the work to breathe. Briefly, ventilatory supports are classified in two types.

- **Invasive ventilation:** where the intubation of the patient is made.
- **Non-invasive ventilation:** where other devices, as cannulas or masks, are used instead of intubation.

The invasive ventilation, also known as mechanical ventilation (MV), is an important resource to treat neonates with acute RDS, even though the use of antenatal corticosteroids and the improvement in non invasive ventilatory support techniques has decreased the use of this type of ventilation. A mechanical ventilator is an automated device that provides all, or part, of the work of breathing for patients with impaired respiratory or neurologic function. The MV allows to control the *peak inspiratory pressure* (PIP) in each inspiration or the *tidal volume* (V_t), known as the normal volume of air displaced between normal inhalation and exhalation when extra effort is not applied. This last one is the less harmful and most used parameter when MV is applied.

However, the use of MV has some side effects, especially in preterm infants because of their small lung size [32]. Some of them are the appearance of BPD, infections or even in some cases brain damage [33]. The optimal strategy for MV use in RDS is not clear, since it expands the lung and care should be taken to use minimal pressures and volumes not to force it. The use of MV can also affect the generation speed of surfactant and their properties [34]. For that reason, MV has to be removed as soon as possible when the neonate shows signs of recovery. Due to all of these adverse effects derived from MV, the non-invasive ventilation (NIV) techniques have become an extremely popular alternative for the RDS treatment.

The most known methods are the following:

- Continuous Positive Airway Pressure (CPAP).
- Nasal Intermittent Positive Pressure Ventilation (NIPPV).
- High Flow Nasal Cannula (HFNC).

The CPAP technique, firstly described by Gregory et al. [35], consists in the application of positive pressure (between 5-10 cmH_2O) to the airways of the spontaneously breathing patient throughout the respiratory cycle. It is applied via an endotracheal tube positioned in a non invasive way, by means of nasal cannulas or mask, among other devices. In this way, the work of breathing of the neonates decreases, assuring a certain pressure in the alveoli and achieving lung stability. It is crucial to control the pressure combined by the CPAP and the spontaneously breathing in order to be small enough to avoid lung injuries [36].

The NIPPV method, which adds a second level of pressure delivery at regular intervals to the patient, was found to be more effective than CPAP in weaning infants with RDS from MV [37]. Further studies and randomized control trials are required to use this method as an alternative to treat RDS [38]. About the HFNC, there are a number of concerns that make no advisable their use in neonates. The impossibility to control the pressure delivered to the infant, which may result in lung overexpansion, and the lack of randomized control trials to assess its safety and effectivity are the main ones [39].

Therefore, the most NIV method employed currently is the CPAP, even though it also has some **limitations**. CPAP should not be considered, for example, in infants who have already met the criteria for ventilatory failure or those who have an unstable respiratory drive with frequent episodes of apnea that cause desaturation and bradycardia. But the most important limitation is that **CPAP and surfactant replacement therapy are not compatible**. At this point, a question comes to mind to the neonatologists. Will initial stabilization of breathing with CPAP be better than early intubation and surfactant treatment for very preterm infants? [40].

Nowadays, the technological progress makes possible to synchronize these methods of NIV to the neonate spontaneously breathing. Neurally Adjusted Ventilatory Assist (NAVA) is a unique approach to MV based on neural respiratory output. The electrical activity of the diaphragm is captured, fed to the ventilator and used to assist the patient's breathing in synchrony and in proportion to the patient's own efforts. A desirable feature for the neonate to face the moment of weaning from the MV [41].

1.4 State of the Art

The surfactant replacement therapy, with the use of MV or CPAP, has been proven as a good treatment to reduce the incidence of RDS and mortality in preterm infants. However, the intubation and use in some cases of MV has contributed to an increase of deep lung and cerebral injuries. To avoid these side effects, new less invasive surfactant administration alternatives and directions are being studied [42].

1.4.1 Alternative Techniques of Surfactant Administration

1.4.1.1 INSURE Technique

One alternative therapy is the INSURE technique (INtubate, SURFactant, Extubate) firstly reported by Verder et al. [43] in 1994. It consists in intubating the preterm infant for surfactant administration with quick (within 10 minutes) extubation to CPAP. Dani et al. [44] made a clinical study with 125 infants classifying them into three groups; infants treated with MV, infants treated with INSURE technique and infants treated only with CPAP. They showed that most of the infants of their study could be treated with INSURE technique with a minimal failure percentage. Sandri et al. [45] published a randomized controlled trial to evaluate the efficacy of combining prophylactic surfactant and early selective surfactant, with CPAP in preterm infants. Their results showed that prophylactic surfactant given within 30 minutes of birth was not superior to early selective surfactant in terms of requirement of MV in the first 5 days of life.

1.4.1.2 Use of Perfluorocarbons

Another alternative is the use of perfluorocarbons (PFC) instead of surfactant. Burkhardt et al. [46] have demonstrated that are useful to improve surfactant distribution and that resulted in a improved oxygenation.

1.4.1.3 Minimally Invasive Surfactant Therapies (MIST)

The upsurge use of non invasive ventilation techniques in preterm babies, as CPAP, has led to the study of new minimally invasive surfactant therapies (MIST). These potential strategies of surfactant administration include:

- Intra-amniotic instillation.
- Pharyngeal instillation.
- Surfactant administration via a laryngeal mask airway surfactant.
- Surfactant administration via a thin endotracheal catheter without intermittent positive pressure ventilation.
- Nebulised surfactant administration in spontaneously breathing infants.

The **tracheal catheterization** is the most extensively method studied so far. Dargaville et al. [47] developed the Hobart method, where Curosurf surfactant at a dose of 100 mg/kg is administered using a semi-rigid vascular catheter briefly passed into the trachea beyond the vocal cords. The results showed that surfactant can be effectively delivered by this technique with a considerably reduction of intubation and MV in the first 72 hours [48]. Kribs et al. [49] are also pioneers in the use of MIST via tracheal catheterization. This approach was implemented in several centers across Germany producing good outcomes, including a reduction in MV [50]. In 2011, the results of an open-label randomised controlled trial with preterm infants between 26 and 28 weeks, showed the feasibility and subsequent reduction in MV, during day 2 or 3 after birth, with the application of surfactant to spontaneously breathing preterm infants by this procedure [51]. Recently, this group has carried out an additional randomized controlled trial comparing the results of two groups. The control group received conventional endotracheal intubation during MV and the intervention group received surfactant via a thin catheter according to their method. Although an increased rate of survival without BPD (which was the primary outcome of the study) was not demonstrated in the intervention group, an increased rate of survival without major complications was observed as well as a reduction in need and duration of MV [52]. Kanmaz et al. [53] have also been investigating the surfactant administration via thin catheter through a randomized controlled trial, the Take Care trial. They compared a group receiving the MIST with another one receiving the INSURE technique. Their results showed also a reduction in MV requirement in first 72 hours of life and lower BPD rate in comparison with INSURE technique. Herting et al. [54] summarized briefly the MIST technique, also known as LISA technique (Less Invasive Surfactant Administration) with the clinical results of some of the aforementioned clinical trials.

The development in the last years of new aerosol devices and surfactant formulations has increased the attention on inhalation therapies to replace and improve the current bolus instillation technique, as suggested in 2004 by Dhand [55]. The **administration of nebulised surfactant** is a promising technique to treat lung diseases and especially RDS even though there are still technical problems and challenges to lead. **Five clinical trials** have been published so far in which preterm infants have been treated with these techniques.

1. **Surfactant Aerosol Treatment of RDS in Spontaneously Breathing Premature infants.**
   This was the first study and it was carried out by Jorch et al. [56] in 1997. 20 preterm infants from 28 to 35 weeks were enrolled in the trial with a median birth weight of 1,680 g. Surfactant nebulization was done using a jet nebulizer via a nasopharyngeal tube. A commercially natural bovine

surfactant was used and a time of nebulization of 20-50 minutes with two doses of 150 mg/kg each one. The CPAP ventilation started between 1 and 7 hours of age and surfactant administration started between 2 and 9 hours of age. Once the nebulization of surfactant started it was noted an immediate improvement in oxygenation and alveolar ventilation. All infants survived and endotracheal intubation and MV was avoided in 70% of them. One limitation of this study is that only 10% of nebulized surfactant entered the pharyngeal tube.

2. **Inhalation of Aerosolized Surfactant to Neonates Treated with CPAP**.

   In this study carried out by Arroe et al. [57] in 1998, 22 preterm infants between 23 and 36 weeks were treated, delivering 108-864 mg of synthetic surfactant (Exosurf) via aerosol by a jet nebulizer and using CPAP as ventilatory support. No benefits were shown in the patients.

3. **Pilot Study of Nebulized Surfactant Therapy for Neonatal RDS.**

   In the clinical study of Berggren et al. [58] performed in 2000, 32 preterm infants between 27-34 weeks were randomized in two groups, 16 not receiving surfactant and 16 receiving 480 mg of nebulized surfactant. All of them were firstly supported with CPAP. Natural porcine surfactant (Curosurf) was used and the aerosol was generated with a jet nebulizer and administered via the CPAP equipment into the nostrils of the patient. No beneficial effects of aerosolized surfactant were demonstrated. One limitation of this study was the late administration of the surfactant, at a mean postnatal age of 19 hours.

4. **An Open Label, Pilot Study of Aerosurf Combined with nCPAP to Prevent RDS in Preterm Neonates.**

   Finer et al. [59] in 2010 evaluated the safety and feasibility of administering Aerosurf (synthetic surfactant) by a vibrating membrane aerosol generator, in combination with CPAP to 17 preterm infant of 28-32 weeks at risk for

RDS. 11 preterm infants were enrolled to the Treatment Group 1, receiving 20 mg/ml of Aerosurf constantly over 3 hours with three additional treatments allowed in the next 48 hours, with each treatment separated by at least 3 hours. The other 6 preterm infants were enrolled to the Treatment Group 2, receiving the same treatment but with the additional treatments separated by a minimum of only 1 hour. The treatment of both groups was initiated within 30 minutes of birth. It was shown that the administration of Aerosurf via nCPAP was safe and feasible but they were unable to conclude whether the patients improvement was due to the nCPAP or the administration of nebulized surfactant.

5. **Nebulised Surfactant to Reduce Severity of Respiratory Distress: A Blinded, Parallel, Randomised Controlled Trial.**
   Minocchieri et al. [60] in 2018 carried out a randomised control trial to evaluate the efficacy of nebulized surfactant treatment. 606 preterm infants with 29-33 weeks were assessed for eligibility but only 64 were enrolled in the study. 32 preterm infants were allocated to receive CPAP (control group) and other 32 to receive CPAP and nebulized surfactant via a customised vibrating membrane nebulizer. The efficiency of nebulized surfactant in the first 4 hours was evaluated and the results showed that surfactant nebulization reduced the requirement for intubation within 72 hours.

All these clinical trials have shown that surfactant administration by aerosolization is a safe and feasible technique, although only the studies of Jorch et al. [59] and Minocchieri et al. [60] have demonstrated the efficacy and benefits of surfactant administration via aerosol. Currently, Dargaville et al. [61] are working in another clinical study, the OPTIMIST-A trial, which is expected to be completed in December 2021. In this study, the control group will be treated only with CPAP whereas the intervention group will receive 200 mg/kg of poractant alfa (Curosurf) administered under direct laryngoscopy using a surfactant instillation catheter. Furthermore, Sood et al. [62] are performing a randomized clinical trial to analyze the efficacy of bovine surfactant aerosol administration and they have already published the results of Phase I. The aerosol was administered through short binasal prongs from a low flow jet nebulizer placed in the inspiratory limb. 17 preterm infants were enrolled, tolerated the aerosol treatment and 15 of them completed the study with a significant improvement in physiological parameters.

One of the main reasons of the **low efficiency of nebulized surfactants** in the clinical trials is the relative low lung deposition rates (less than 1% of the mass nebulized) with conventional jet and ultrasonic nebulizers [63, 64]. Recently, Tiemersma et al. [65] have checked that the lung deposition with a vibrating mesh nebulizer prototype for babies is quite higher (between 18% and 20.5%). Several factors influence in this lack of lung deposition in preterm infants:

1. Particles tend to deposit in the walls of the respiratory tract due to the small dimensions of preterm infants airways.
2. Particles too small could be exhalated due to their high respiratory rate.
3. Their small lung volume.
4. No possible interaction and communication with the patient.
5. The requirement of specialized medical devices for their use in neonates.
6. The viscous characteristics of the surfactant which worsen the efficiency of nebulizers.
7. Nebulizers could inactivate the properties of the surfactant.

To achieve satisfactory results with nebulized surfactant therapy it is important to take into account some aspects as:

1. Size of the particles.
2. Type of surfactant.
3. Choice of surfactant nebulizer.
4. Length of treatment.
5. Dose of surfactant.

The **size of the particles** have a major importance in terms of lung deposition. Inhaled particles may deposit in various regions of the respiratory system mainly by three deposition mechanisms: inertial impaction, gravitational settling and diffusion, as shown in Figure 1.5. Each time the airflow changes due to a bifurcation in the airways, the suspended particles tend to travel along their original path due to inertia and may impact on an airway surface. *Inertial impaction* occurs mostly with larger particles that are very close to airway walls, near the first airway bifurcations. Therefore, deposition by impaction is usually produced in the bronchial region. Deposition by *sedimentation* occurs in the smaller airways of the bronchioles and alveoli, where the air flow is low and airway dimensions are small. The sedimentation rate is dependent on the terminal settling velocity of the particles, so sedimentation plays a greater role in deposition of particles with larger aerodynamic diameters. *Diffusion* is the primary mechanism of deposition for particles less than 0.5 μm in diameter. Diffusion is the net transport of particles from a region of high concentration to a region of lower concentration due to Brownian motion, which is the random wiggling motion of a particle due to the constant bombardment of air molecules. Diffusional deposition occurs mostly when particles have just entered the nasopharynx, and it is also most likely to occur in the smaller airways of the pulmonary region, where air flow is low.

Stahlhofen et al. [67] measured the total lung deposition as a function of particle size. Radioactively labeled particles between 1-10 μm were administered in three male adults measuring the particle sizes through a photometer technique. The results showed that, for particles larger than 10 μm, deposition occurred due to inertial impaction in the oropharyngeal region whereas particles of 5-10 μm tended to be deposited in the tracheo-bronchial region. Only particles with less than 5 μm reached the alveolar region. Salma et al. [68] also studied the effect of particle mass size distribution on the deposition of aerosols in the respiratory system for adults and a 5-year-old child. Particles in the aerodynamic size range of 1-5 μm are considered respirable. However, small particles in combination with short and low inspiratory flows increase the risk of exhalation drug losses.

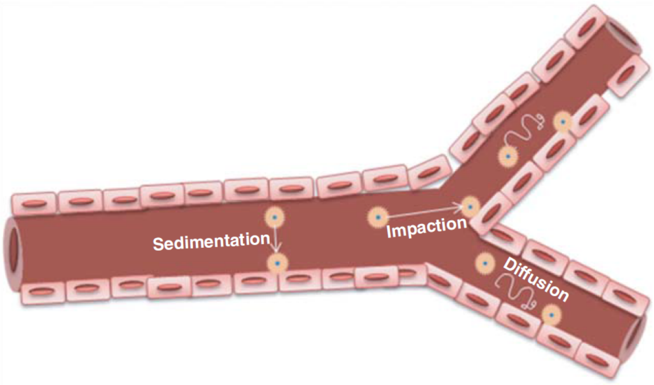

Figure 1.5: Deposition mechanisms of particles in the respiratory tract.
Source: Verma et al. [66].

The **ventilation set-up and the position of the nebulizers** in the ventilator circuit also affect on aerosol drug delivery and their lung deposition. Winterhalter et al. [69] established an *in vitro* model to evaluate the amount of aerosol delivered through an endotracheal tube. They also studied whether or not different ventilator modes and types of endotracheal tubes influence the aerosol delivery performance. Two methods were applied to integrate the nebulizer into the ventilation circuit. In the first one (set-up A) the ultrasonic nebulizer is placed between the endotracheal tube and the ventilator circuit whereas in the second one (set-up B) it is placed at the same way but using a bypass. The results showed that set-up B was not clearly superior to set-up A with respect to the total output at the tip of the endotracheal tube. The reason of these results was that the advantage provided by the bypass circuit, releasing aerosol during inhalation, was almost eliminated because a large amount of aerosol was accumulated inside the additional tubing. Ari et al. [70] assessed different aerosol generator devices at 3 locations in humidified and non-humidified circuits during adult mechanical ventilation: between the endotracheal tube and the Y-piece; 15 cm from Y-piece; and 15 cm from the ventilator. The results showed that during mechanical ventilation the optimal drug delivery efficiency depends on the aerosol generator, the ventilator circuit, and the aerosol generator position. Murgia et al. [71], recently, studied the influence of four different ventilation strategies on aerosol production rate. Surfactant and three PFCs were aerosolized during mechanical ventilation by means of three intratracheal inhalation catheters (IC) with different air flow rates. The results showed that higher respiratory rates (RR) and higher peak inspiratory pressures (PIP) might enhance surfactant and PFC delivery to the lungs but might also increase compound loss during the expiratory phase.

1.4.2 Aerosol Drug Delivery Devices

The main goal of these devices is to produce an aerosol with the sufficient size and mass in their droplets and therefore, to be carried to the distal lung or deposited on proximal airways to give rise to a therapeutic effect. This route of administration provides low doses of an aerosolize drug with a quick clinical response without many side effects. They are commonly divided into three types, as described by Martin et al. [72]:

1. Pressurized metered dose inhaler (pMDI).
2. Dry powder inhaler (DPI).
3. Nebulizers.
    - Jet nebulizers.
    - Ultrasonic nebulizers.
    - Vibrating mesh nebulizers.

The **pMDI device** consists of a canister, a metering chamber, and an actuator with a mouthpiece, as illustrated in Figure 1.6. Medication is found in solution with a liquified gas propellant (hydrofluoroalkane [HFA]) and is housed in a pressured canister fitted with a metering valve. The pressure needed for the aerosolization of the medication is created in the canister by shaking the device to disperse the liquefied gas propellant into the medication solution. As the canister is depressed into the plastic actuator, one metered dose of medication is delivered in a high-velocity spray via the actuator nozzle to the mouthpiece.

The high-velocity aerosol plume only lasts $100 - 400$ milliseconds as the size of particles continues to diminish due to the evaporation of the HFA propellant. Aerosolized particles may diminish in size from 45 μm at the actuator nozzle to 0.5 μm 6 inches from the mouthpiece. Particle size is a key determinant of the respirable dose. Larger particles ($>$10 μm) are highly likely to remain in the oropharynx; midsized particles (5-10 μm) remain in the upper large bronchial tree, while those of optimum size (1-5 μm) reach the lower airways. Smaller particles ($\leq$ 0.5 μm) are not deposited in the lungs but are instead exhaled as a gas. However, even with a correct inhaler technique, most pMDIs only deposit 10-20% of the labeled dose in the lungs; much of the medication remains in the mouth and oropharynx, potentially leading to local and systemic adverse effects.

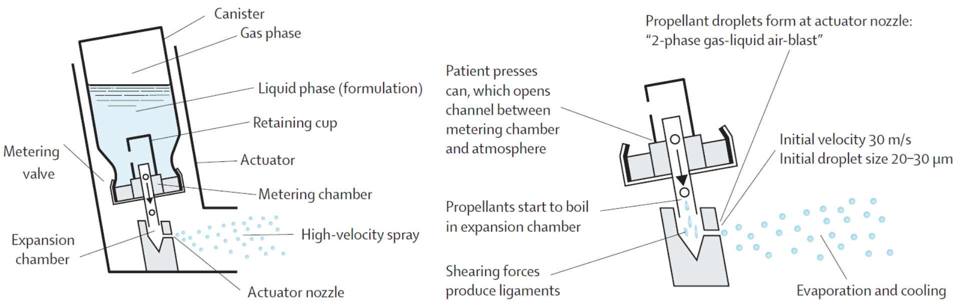
Canister
Gas phase
Liquid phase (formulation)
Retaining cup
Metering valve
Actuator
Metering chamber
High-velocity spray
Expansion chamber
Actuator nozzle
Propellant droplets form at actuator nozzle: "2-phase gas-liquid air-blast"
Patient presses can, which opens channel between metering chamber and atmosphere
Initial velocity 30 m/s
Initial droplet size 20–30 μm
Propellants start to boil in expansion chamber
Shearing forces produce ligaments
Evaporation and cooling

Figure 1.6: Scheme of a pressurized metered dose inhaler (pMDI). Source: Dolovich et al. [73].

The purpose of the **Dry Powder Inhalers (DPI)** is to insert a prescribed dose of powder aerosol into the air inhaled by a patient during a single breath [74]. Normally, the powder is delivered during a single, large breath. So it also requires a good coordination by the patient to use it appropiately and, therefore, it is not suitable to be used in neonatal population.

Nebulizers are devices that convert a liquid in solution or suspension into small droplets. The main advantage in the face of pDMI and DPI is that they do not need the interaction of the patient as well as the coordination of inhalation/exhalation to obtain an optimum delivery. As it has been seen above, they can be sorted in three different types according to the power source used to produce the breakup of the liquid [75]. O'Callaghan and Barry [76] analyzed how they work and described some of the most important parameters to define an aerosol and some methods of measuring particle size, aerosol deposition and nebulizer output.

Jet nebulizers are based on the Bernoulli principle. A pressurized flow of gas, generally air, is directed through a constricted orifice where the velocity of the airflow is increased to create a jet stream. This jet stream creates a sub-atmospheric pressure zone (vacuum) which draws the fluid up the capillary tube. The impact of a jet stream with the liquid and the extreme difference in velocity between them produces aerosol particles or droplets.

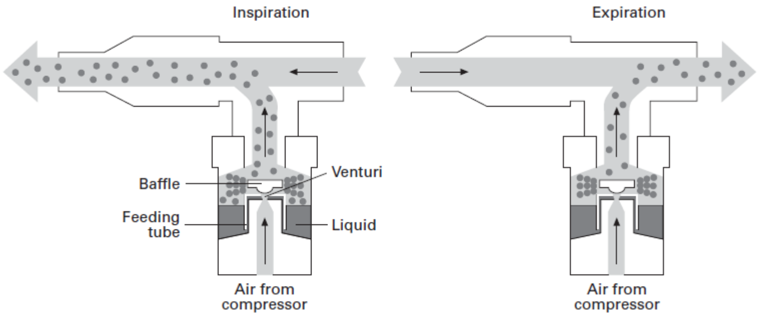

Figure 1.7: Schematic of a conventional jet nebulizer. Source: Martin et al. [72].

Ultrasonic nebulizers remove the need for a compressed air source and, instead, a high-frequency vibration generated by a piezoelectric crystal is used to the formation of droplets. They present some troubles, as the significant heating of the nebulizer solution and difficulties with nebulizing high-viscosity liquids. For these reasons, this type of nebulizer was rapidly dismissed as an option for our case due to the viscous characteristics and heat-sensitive of the surfactants.

Vibrating mesh nebulizers force liquid medications through multiple apertures in a mesh or aperture plate in order to generate an aerosol. They present 2-3 times higher lung depositions than classic jet nebulizers and are able to nebulize in low drug volumes. Despite all of these advantages they still present some challenges. For instance, viscous drugs can clog the pores, cleaning the mesh can be difficult and are more expensive than the other alternatives. Tiemersma et al. [65] evaluated lung deposition of salbutamol using two vibrating mesh nebulizers, designed specifically for use in preterm infants, and they compared them with a jet nebulizer and a pMDI. The results showed that lung deposition was significantly higher for the investigational vibrating mesh nebulizers in an *in vitro* model of a preterm infant of 32-weeks gestational age.

Recently, Syedain et al. [77] developed a novel aerosol generator for surfactant aerosol delivery in preterm infants. Even though this device still requires the intubation of the neonate it showed promising results, with the generation of small aerosol droplets and operating with low airflow. Milesi et al. [78] have also worked in this direction developing a new atomizing device, consisting of a small multilumen catheter, for intracorporeal nebulization of surfactant during CPAP. In a recent research, they conducted a study to deliver nebulized surfactant without the need of intubation in spontaneously breathing preterm lambs, showing encouraging results [79].

1.5 Application of CFD Techniques in Human Respiratory Airways

The definition of numerical models by means of Computational Fluid Dynamics (CFD) tools provides a helpful methodology to analyze several health issues. Specifically, in the study of respiratory diseases as the RDS, a numerical model validated with experimental data is a highly valuable source of information about the aerosol particles behavior within the respiratory tract.

Relatively little work has been performed in modeling pharmaceutical aerosols in neonatal subjects. The smaller size of the preterm infants' airways and the difference of breathing conditions affect parameters such as the air flow velocity and particle transport and, therefore, do not make it possible to extrapolate the results obtained from adult airways. Allen et al. [80] studied in 2004, with the help of CFD tools, the airflow in an *in vitro* model of a five-year-old pediatric subject. In the treatment of respiratory diseases, Longest et al. [81] in 2006 created a CFD numerical model to evaluate the deposition patterns in the airways of a four-year-old child under healthy and constricted conditions. De Jongh et al. [82] obtained, by means of computed tomography, the geometry of the upper airways of a nine-month-old infant to calculate the deposition of microparticles and compared them with experimental results (See Figure 2.9a). Liu et al. [83] studied, with a CFD model, the airflow patterns and the deposition of particles in the first three generations of a pediatric upper respiratory tract. Their results showed higher velocity fields, deposition rates and impaction numbers in comparison with those observed in adults. This numerical model was validated with experimental data taken from the study of Golshahi et al. [84].

In the last years, Tsega [85] has compared the respiratory airflow characteristics in tracheobronchial airways of infant (6 months old), child (5-years-old) and adult (25-years-old) reflecting that as age increases, airflow velocity, pressure and wall shear stress decrease for both inspiration and expiration in this subregion of the respiratory tract. Similarly, Deng et al. [86] have compared the particle deposition in upper and lower airways in an infant (7-months-old), a child (4-years-old) and an adult (20-years-old). They observed that the highest deposition values were obtained in an infant, with most of the particles deposited in the upper airways due to inertial impaction. Bass et al. [87] printed a 3D model with the nasal airways of a 6-months-old infant to carry out *in vitro* experiments, as illustrated in Figure 2.9b, and used a CFD model to study the transport and deposition of micrometer-sized aerosol particles. The CFD results were validated with the *in vitro* experiments and concluded that aerosol particles with an aerodynamic diameter around 1.5 μm are ideal to be delivered through an infant nasal cannula with high-efficiency lung delivery. The aerosolization of surfactant was also analyzed with a CFD model by Goikoetxea et al. [88] using a multi-lumen inhalation catheter with minimal manipulation of the airways. They corroborated the feasibility of this device to generate a surfactant aerosol with an adequate size and validated the CFD model with experimental data, providing optimization guidelines.

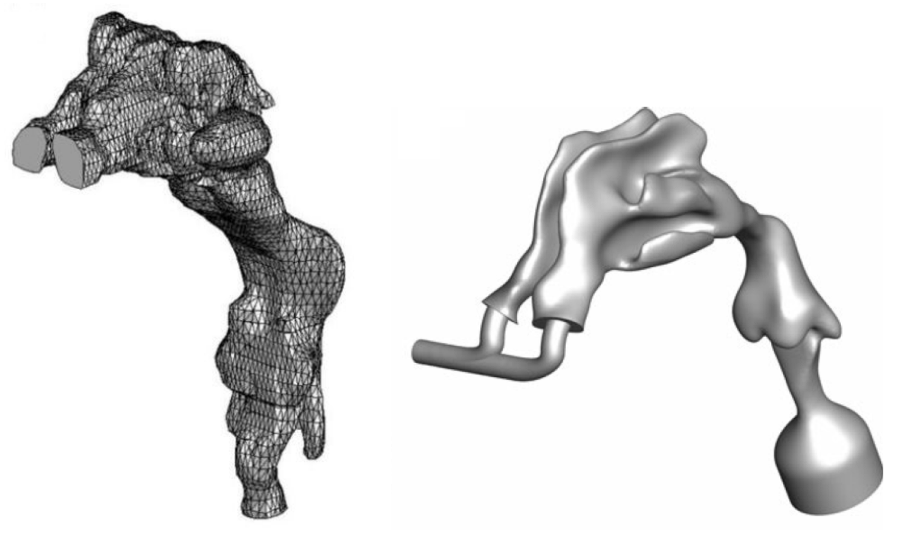
(a) *Saint* model.

(b) Bass model.

Figure 1.8: *Saint* model of a 9 month-old infant upper airways [82] and (b) nasal airways model from a 6 month-old infant [87].

The research in this field is more extensive in adult airways, using CFD tools to study the influence of modified geometries, respiratory patterns, particle sizes and different types of devices in lung deposition. Oldham et al. [89] studied the influence of parameters such as the breathing rate and the particle size on particle deposition in the respiratory tract. Koombua et al. [90] explored the influence of airway wall elasticity analyzing two cases, rigid and flexible wall, respectively. It was observed that the pressure within the airways was affected, but not the air flow velocity or the wall shear stress. Recently, Elcner et al. [91] developed a CFD model validated with experimental results of the inspiratory airflow in a model from the throat to the fourth generation of the respiratory tract. Feng and Kleinstreuer [92] studied the deposition, interaction, and transport of particles in triple bifurcations, by means of the dense discrete phase model and the discrete element method. Walenga et al. [93] evaluated with a CFD study the deposition fraction delivered with a pMDI and a DPI to healthy and constricted airways. Both inhalers provided very low drug dose (1.13% and 1.08% respectively) and was even lower in constricted airways. Delvadia et al. [94] varied the angle in the positioning of a pMDI and DPI device. They highlighted the influence of this inclination on the speed, size and, therefore, on the deposition of particles.

1.6 Thesis Motivation

The Department of Neonatal Physiology of the BioCruces Health Research Institute is working since 1988 in the study of the RDS and the postnatal lung maturity. The research staff have more than 20 years of experience in the administration of surfactant experimentally and clinically, evaluating new minimally invasive surfactant therapies in order to improve the RDS treatment in preterm infants. As a result, they are authors of high quality contributions in the field. They were the first to compare the administration of natural versus synthetic surfactant in immature lambs [95]. Additionally, they have observed for the first time that a standard dose of surfactant for established RDS delivered as an aerosol can produce similar response to rapid intratracheal bolus instillation of the same dose [96]. They also have studied recently the impact of different surfactant administration techniques on the cerebral oxygenation [97].

Since 2008, as a result of some research projects (SAIOTEK) funded by the Basque Government (Spain), they explored the administration of aerosolized surfactant. Given the necessity for a specific nebulizer to nebulize surfactant in the pediatric population, the research group came to the conclusion in 2011 to **develop a nebulizer prototype**. The manufacturing of a device able to generate an aerosol of surfactant in pediatric population would mark a milestone in the treatment of preterm infants affected with RDS. In fact, taking into account the low efficiency of conventional nebulizers in the neonatal population, this device could be helpful in the nebulization of other medical substances (bronchodilators, steroids, antibiotics, etc.). To that end, a multidisciplinary group has been assembled in the last years formed by the Cruces University Hospital-BIOEF (Basque Foundation for Health Innovation and Research), the Department of Nautical Science and Marine Systems and the Nuclear Engineering and Fluid Mechanics Department (UPV/EHU, University of the Basque Country).

Therefore, working in this direction and after evaluating all the different techniques that are able to administer surfactant in a non-invasive way and the research carried out in this field, it has been concluded that the combination of surfactant in aerosol form along with the application of CPAP would be an optimal choice. It has been observed that most of the current devices generate extracorporeal aerosols, leading to low lung deposition values. For that reason, they started to consider alternatives to generate an intracorporeal aerosol, as the inhalation catheter studied deeply by Goikoetxea et al. [88, 98] both experimentally and numerically with CFD techniques. Their study demonstrated the feasibility of this device to deliver large amounts of surfactant and PFC to the lungs and provided the basis to design a new specific device to treat the RDS in preterm infants.

The motivation of the current thesis is to design and manufacture a novel nebulizer prototype and to evaluate the feasibility to generate droplets with potential to be delivered in the supraglottic region. Additionally, a numerical model is developed and validated with experimental data to facilitate further parametric studies of optimal nebulizers in preterm babies with RDS.

1.7 Hypotheses

Two hypotheses have been considered in the development of this research. On the one hand, it is argued that the non-invasive intracorporeal administration of nebulized surfactant can be combined with a non-invasive ventilatory support such as CPAP. The nebulizer prototypes proposed in this thesis are intended to be placed in the supraglottic region, bypassing the upper airways, and directly atomizing into the pharynx, avoiding the need for intubation and making them compatible with the use of CPAP.

On the other hand, it is argued that once the surfactant reaches the third generation of the airways, and even to the trachea, it is easily distributed to the more distal generations. This is due to the high viscosity of the surfactant and the ability to spread once deposited on the walls. Therefore, a good distribution through the lungs is ensured once the surfactant reaches the trachea.

1.8 Objectives

The main goal of this thesis is the design and development of a novel nebulizer prototype able to generate aerosols to be inhaled by preterm infants. The specific objectives that have been set to achieve this goal are the following:

- Characterization of the aerosol obtained with an inhalation catheter IC-1.1 by means of experimental measurements.
- Development of a numerical model with CFD tools of the aerosol produced with the inhalation catheter IC-1.1.
- Validation of the CFD numerical model with experimental data.
- Study the feasibility of additive manufacturing techniques to fabricate a prototype able to generate a nebulization process.
- Design a prototype allowing the aerosol generation and offering potential to drug delivery without the need of intubation.
- Manufacture a nebulizer prototype with additive manufacturing techniques.
- Characterization of the aerosol obtained with the prototypes manufactured by means of experimental measurements.
- Discuss the feasibility and limitations of the prototypes manufactured after analyzing the experimental results obtained.
- Establish guidelines to optimize the design of the nebulizer prototype to improve the aerosol characteristics, the distal pressure values and the
- Design a pressure control system able to control the liquid administration velocity and the pressure applied throughout the prototype.

1.9 Methodology

The methodology followed to complete these objectives consists in the application of CFD techniques to develop a numerical model able to characterize the aerosol particle size distribution, the design and manufacturing of optimized nebulizer prototypes and the execution of experimental measurements (See Figure 1.9).

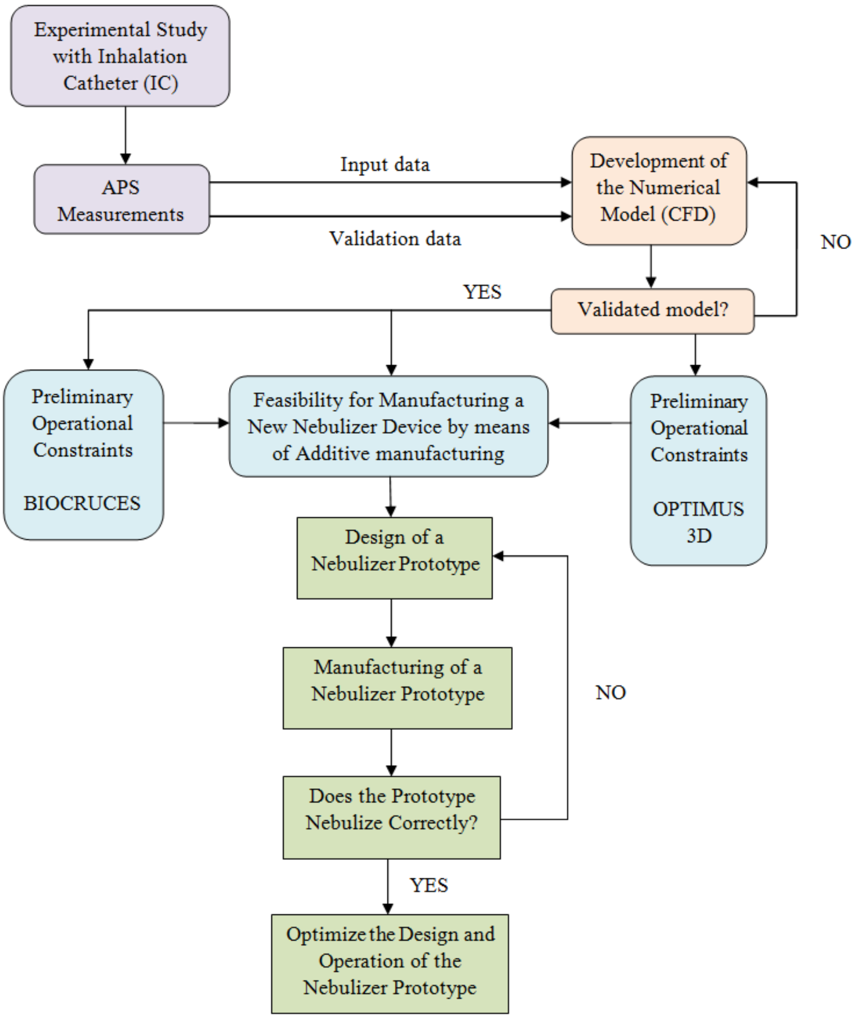
Experimental Study with Inhalation Catheter (IC)
APS Measurements
Input data
Validation data
Development of the Numerical Model (CFD)
NO
YES
Validated model?
Preliminary Operational Constraints BIOCRUCES
Feasibility for Manufacturing a New Nebulizer Device by means of Additive manufacturing
Preliminary Operational Constraints OPTIMUS 3D
Design of a Nebulizer Prototype
Manufacturing of a Nebulizer Prototype
NO
Does the Prototype Nebulize Correctly?
YES
Optimize the Design and Operation of the Nebulizer Prototype

Figure 1.9: Flow chart of the methodology used.

1.10 Contents and Structure of the Thesis

The current thesis has been structured with the following chapters:

- **CHAPTER 1: Introduction.** It contains a description of the RDS and the current medical treatment, that involves the surfactant replacement therapy and the use of ventilatory support. New minimally invasive surfactant therapies (MIST) are described and, in particular, the surfactant nebulization with new aerosol devices. Finally, the use of CFD tools in the modeling of human respiratory airways and pharmaceutical aerosols is described.

- **CHAPTER 2: Aerosol Model with Inhalation Catheter.** This chapter presents an experimental and numerical model of the aerosol produced by means of the inhalation catheter IC-1.1 (Aeroprobe, Trudell Medical International). The nebulization produced with three different compounds is studied: distilled water (H_2Od) and two perfluorocarbons (PFC); perfluorodecalyn (PFD) and FC75. An Aerodynamic Particle Sizer (APS) spectrometer is used to carry out the particle size characterization of the droplets generated with the IC-1.1. Additionally, a 2D axisymmetrical numerical model is developed with CFD techniques and validated with experimental data.

- **CHAPTER 3: Nebulizer Prototype Design.** This chapter, initially, describes the use of additive manufacturing techniques in medical applications, the main technologies currently used and their characteristics. Then, two nebulizer prototypes are designed and manufactured by means of the PolyJet technology. Experimental measurements are taken with the APS for both prototypes using H_2Od, PFD and FC75. Finally, the droplet size and mass characterization results are compared and discussed.

- **CHAPTER 4: Optimization of Nebulizer Prototype.** This chapter contains guidelines to optimize the design of the nebulizer prototype. Some modifications in the design of the prototypes are included with the aim of improving the nebulization process and to reduce the pressure at the distal end of the prototypes. New prototypes are manufactured and experiments are made to control the distal pressure and the nebulization velocity.

- **CHAPTER 5: Conclusions and Future Work.** To conclude, this chapter presents the main conclusions of the research work carried out and proposes future lines and considerations to advance in the investigation of this subject area.

Additionally, two Appendices have been introduced:

- **APPENDIX A: Nebulizer Prootypes Designs.** It contains all the drawings corresponding to the nebulizer prototypes designed throughout this thesis.
- **APPENDIX B: Publication and Conferences.** The results and conclusions obtained in the current thesis have been published in two JCR indexed journals: *International Journal of Environmental Research and Public Health* (IF 2.468) and *Pharmaceutics* (IF 4.773). In addition, two contributions were presented in two different international conferences.

CHAPTER 2

AEROSOL MODEL WITH INHALATION CATHETER

2.1 Experimental Model

This section presents, initially, the inhalation catheter used for the aerosol generation, the compounds studied and the experimental setup installed to measure the mass and size particle distribution. Finally, the experimental results obtained are presented for each compound and pressure studied.

2.1.1 Inhalation Catheter

The inhalation catheter IC-1.1 (Aeroprobe, Trudell Medical International) has been used to model the aerosol generation. This type of catheter, which has already been tested in different studies [98, 99], allows the generation of intracorporeal aerosols avoiding the deposition of aerosol droplets in the nasopharyngeal region. Additionally, it can be placed in a non-invasive manner and does not involve an increase in the temperature of the compound to be nebulized, as opposed as vibrating mesh nebulizers. The total length of the IC-1.1 is 1 meter and consists of a central lumen, where the liquid to be nebulized is delivered, and six outer lumens where compressed air is dispensed, as illustrated in Figure 2.1.

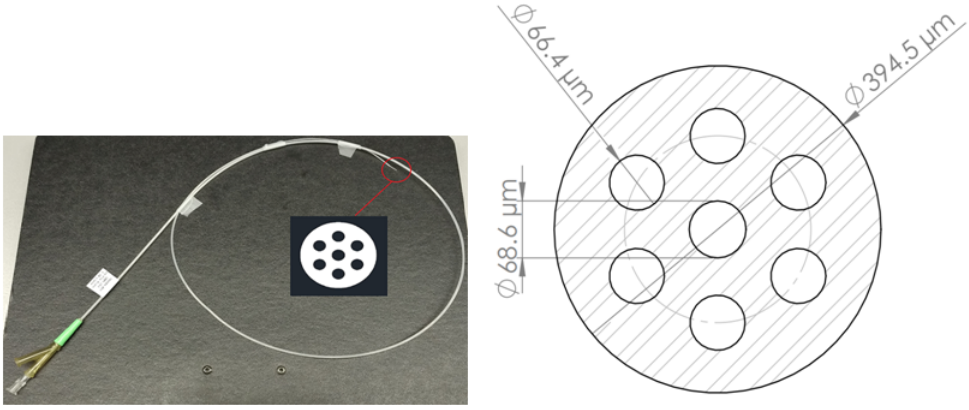

Figure 2.1: Inhalation catheter (IC 1.1) with a cross section detail of the distal end.

The diameter of these lumens becomes smaller as it approximates to the catheter tip. The proximal diameter of both central and outer lumens is 330 μm, while in the catheter tip the diameter corresponds to 68.6 μm and 66.4 μm for the central and outer lumens, respectively. The high air velocity produced due to the diameter reduction, along with the closeness of the lumens, leads to the nebulization of the liquid.

2.1.2 Compounds Nebulized

Three different compounds have been used in order to analyze the aerosol generation with the IC-1.1. Distilled water (H_2Od) and two different perfluorocarbons (PFC); perfluorodecalyn (PFD; $C_{10}F_{18}$, F2 Chemicals Ltd., Lancashire, UK) and FC75 ($C_8F_{16}O$, Fluorinert, 3M, Neuss, Germany). Their properties can be seen in Table 2.1. Distilled water is used for drug dilution and the aerosolization of aqueous medications whereas the biophysical properties of PFCs have shown to improve oxygenation and to reduce lung injury in cases of severe respiratory insufficiency, as studied by Guo et al. [100]. Partial liquid ventilation with PFCs has been used in the experimental field and proven effective in the treatment of various lung diseases in a wide range of animal models, reaching human clinical trials [101]. The aerosol delivery of PFCs has been suggested as a promising method over instillation to improve lung function [102]. Von der Hardt et al. [103] compared different PFCs in surfactant-depleted rabbits showing their effectiveness and suitability for aerosol treatment.

Parameter	**H_2Od**	**PFD**	**FC75**
Density (ρ) [g/ml]	0.99	1.95	1.78
Kinematic viscosity (υ) [cSt]	1.003	2.70	0.81
Surface tension (σ) [dyn/cm]	73	15	15

Table 2.1: Properties of H_2Od and PFCs.

2.1.3 Experimental Setup

Figure 2.2 shows the experimental setup installed to measure the particle size distribution of the aerosols generated with the IC-1.1. The mean aerodynamic diameter (D_a), the mass median aerodynamic diameter (MMAD) and the geometric standard deviation (GSD) have been analyzed.

The aerosol parameters obtained with the IC-1.1 were measured with the help of the **Aerodynamic Particle Sizer (APS)** spectrometer illustrated in Figure 2.3, which provides high-resolution measurements of aerosol droplets from 0.5 μm to 20 μm. The distance between the catheter tip of the IC-1.1 and the inlet nozzle of the APS was checked in order to obtain the average 1000 droplets/cm^3 concentration recommended by the manufacturer. The APS uses a patented double-crested optical system for unmatched sizing accuracy and, by means of two laser beams, it generates a signal when a droplet passes through them (See Figure 2.4). The acceleration of droplets, that will be smaller for bigger droplets because of their larger inertia, is obtained from the time between the peaks of the sig-

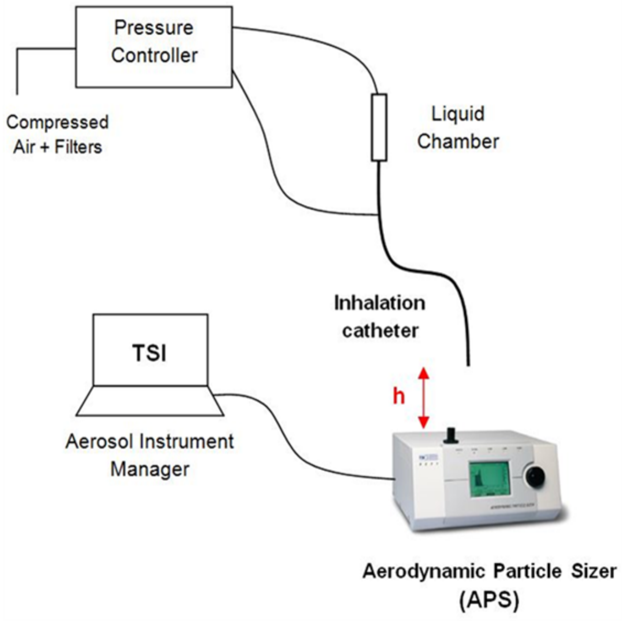
Pressure Controller
Compressed Air + Filters
Liquid Chamber
Inhalation catheter
TSI
h
Aerosol Instrument Manager
Aerodynamic Particle Sizer (APS)

Figure 2.2: Experimental setup used for the particle size characterization of the droplets generated with the IC-1.1.

nal, also known as time-of-flight. Then, with the sphere calibration stored in the spectrometer memory, the APS converts each time-of-flight measurement to its corresponding aerodynamic particle diameter (D_a), described as the diameter of a spherical droplet with a density of a water droplet (1000 kg/m^3) that has the same settling velocity as the measured droplet.

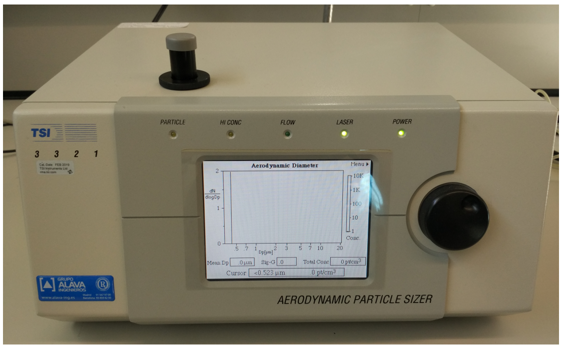
TSI
3 3 2 1
PARTICLE
HI CONC
FLOW
LASER
POWER
Aerodynamic Diameter
AERODYNAMIC PARTICLE SIZER

Figure 2.3: Aerodynamic Particle Sizer (APS) Model 3321.

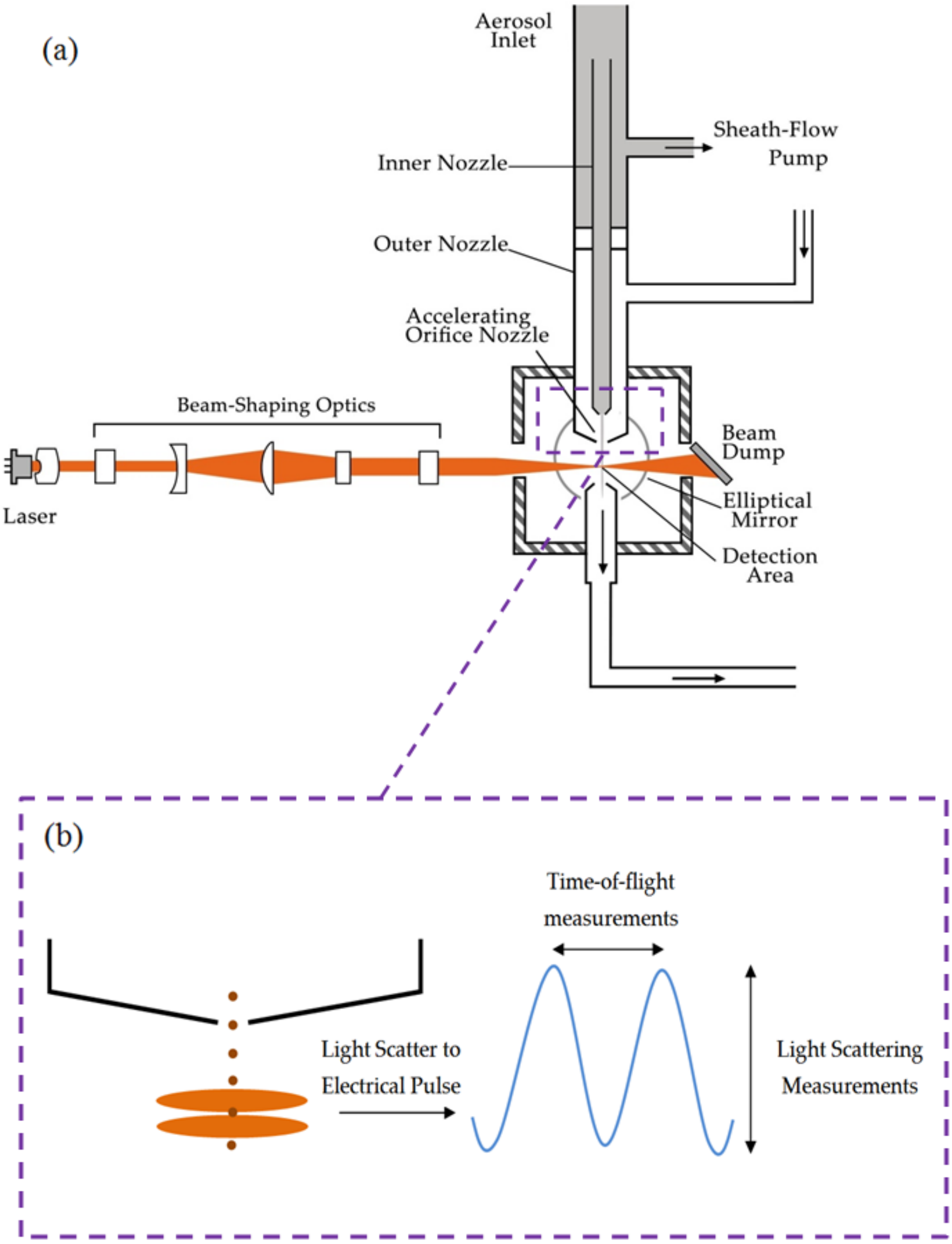
(a)
Aerosol Inlet
Sheath-Flow Pump
Inner Nozzle
Outer Nozzle
Accelerating Orifice Nozzle
Beam-Shaping Optics
Beam Dump
Laser
Elliptical Mirror
Detection Area
(b)
Time-of-flight measurements
Light Scatter to Electrical Pulse
Light Scattering Measurements

Figure 2.4: (a) Aerodynamic Particle Sizer (APS) operation scheme, (b) detail view with aerosol droplets crossing the overlapping beams and generating the double-crested signal.

The APS measures and classifies the droplets in **four events** according to their aerodynamic diameter, as can be seen in Figure 2.5. The first one groups the droplets with a diameter smaller than 0.5 μm, the second one classifies the droplets that are in the spectrometer measuring range from 0.5 μm to 20 μm. The third event considers those particles that cross the laser beams at the same time, and the last event group droplets bigger than 20 μm.

Therefore, in order to have a sample measured accurately, it is important to have most of the particles classified in the first two events and, above all, in the second event where droplets from 0.5 μm to 20 μm are measured. In other words, it is convenient to obtain a negligible percentage at events three and four to consider the measurement reliable, where particle coincidence and particles out of the range of measurement are classified, respectively. All data and information captured by the APS is recorded and visualized by the Aerosol Instrument Manager software.

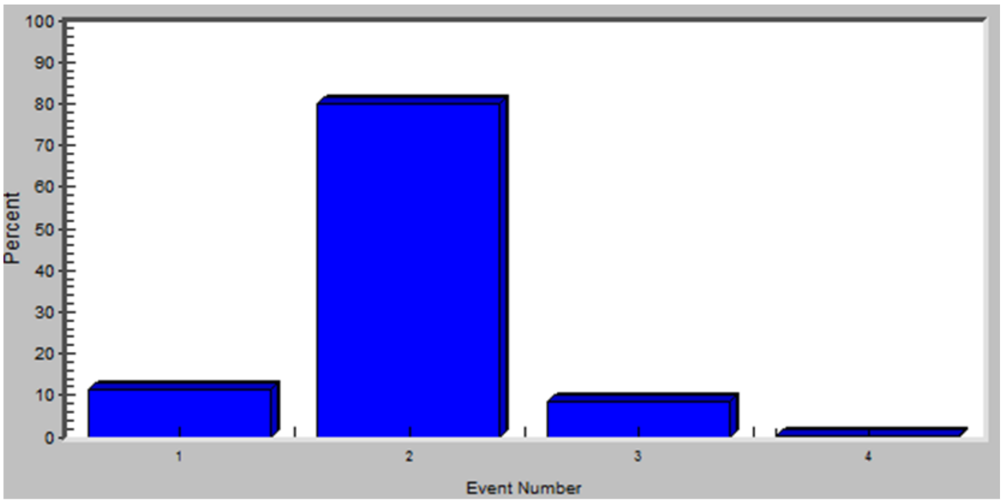

Figure 2.5: Percentage of droplets classified in each event for one sample.

The **air pressure controller** shown in Figure 2.6 (LABneb, Trudell Medical International), with an operating range of 0-7 bar, has been used to provide compressed air to both the small piston placed within the liquid chamber and to the side connection of the IC-1.1.

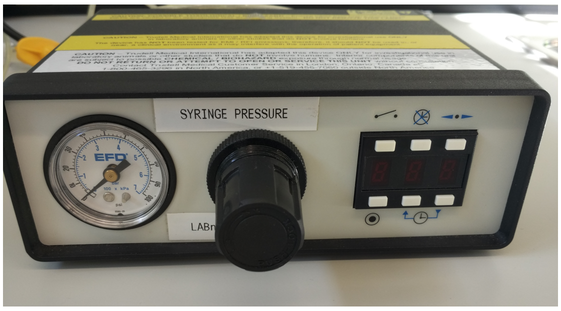
SYRINGE PRESSURE
EFD

Figure 2.6: Air pressure controller.

Figure 2.7 shows the **liquid chamber** filled with the liquid desired to be nebulized, the three-way valve to control the liquid distribution and the two connections to deliver the liquid and the compressed air to the central and outer lumens of the IC-1.1.

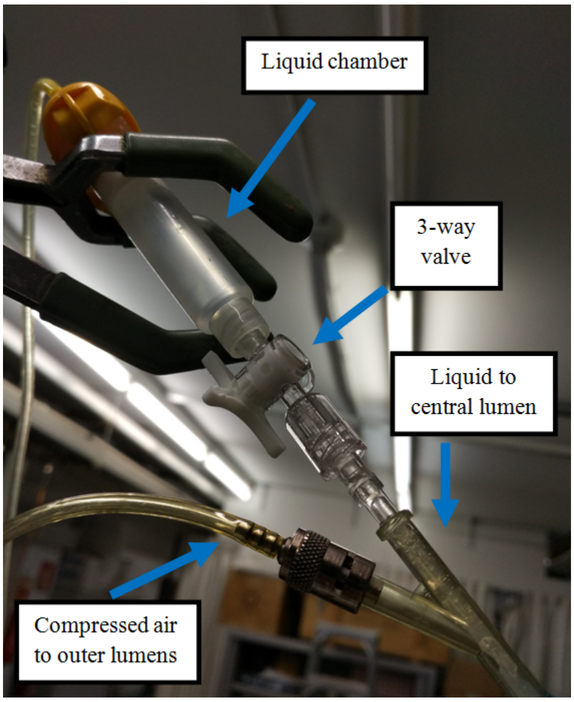
Liquid chamber
3-way valve
Liquid to central lumen
Compressed air to outer lumens

Figure 2.7: Distribution of compressed air to the piston of the liquid chamber and to the side connection of the IC-1.1.

The catheter has been aligned with the APS nozzle in the vertical direction to obtain accurate measurements of the aerosols generated. Initially, due to the length of the IC-1.1 and the small dimensions of the distal tip, the catheter presented some alignment issues during the nebulization process. In order to avoid that, the distal end of the catheter has been passed through a cylindrical plastic guide with a drill of 1 mm, as can be observed in Figure 2.8.

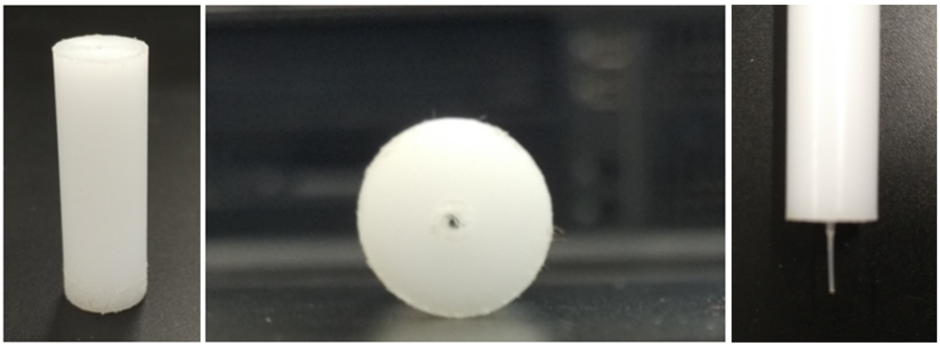

Figure 2.8: Alignment of the IC-1.1.

2.1.4 Experimental Results

The characterization of the aerosols formed with the IC-1.1 was studied by means of the D_a, the MMAD and the GSD. The relationship between the aerodynamic droplet diameter (D_a) measured by the APS and the geometric droplet diameter (D_g) is given by Equation 2.1.

$$D_g = D_a\sqrt{\frac{\rho_0}{\rho}} \tag{2.1}$$

where ρ_0 is the unit density (1 g/cm^3) and ρ the density of the compound to be nebulized.

The MMAD measures the aerodynamic diameter (D_a) at which 50% of the aerosol mass is present in droplets below or above this value. Finally, the GSD is a dimensionless number which gives an indication of the spread of sizes of droplets that form the aerosol. A GSD value below 1.2 indicates that the aerosol is formed by droplets with the same or very nearly size (monodisperse aerosol) whereas a value above 1.2 shows that the aerosol contains droplets of many different sizes (heterodisperse aerosol) [76].

Different distances between the distal end of the catheter and the APS nozzle were tested in order to obtain an aerosol with a concentration as close as possible to the recommended value of 1000 droplets/cm^3. In the case of H_2Od, it was found that the optimal distance was 42 cm. A sample time of 10 seconds was set, recording five samples for each pressure and verifying that in each sample most of the droplets were classified within the second event. Tables 2.2 and 2.3 show the results nebulizing H_2Od at four different driving pressures from P=4 bar to P=6 bar. It was observed a smooth proportional increase in the D_a value with the driving pressure, from 4.06±0.05 μm (4 bar) to 4.84±0.05 μm (6 bar). The MMAD values varied between 10-11 μm and in all cases the IC-1.1 produced heterodisperse aerosols, with a GSD between 1.89±0.06 (6 bar) and 2.18±0.03 (4 bar).

H_2Od P=4 bar (h=42cm)				**H_2Od P=4.5 bar (h=42cm)**			
Sample	**Da (μm)**	**MMAD (μm)**	**GSD**	**Sample**	**Da (μm)**	**MMAD (μm)**	**GSD**
11	4.00	10.3	2.20	16	4.55	10.8	2.09
12	4.09	10.3	2.19	17	4.24	10.2	2.14
13	4.08	10.1	2.15	18	4.33	10.6	2.16
14	4.12	9.89	2.14	19	4.51	10.5	2.06
15	4.01	10.2	2.21	20	4.67	10.9	2.08
MEAN	**4.06**	**10.16**	**2.18**	**MEAN**	**4.46**	**10.60**	**2.11**
SD	**0.05**	**0.17**	**0.03**	**SD**	**0.17**	**0.27**	**0.04**

Table 2.2: H_2Od experimental results with driving pressures of P=4 bar and P=4.5 bar.

H_2Od P=5 bar (h=42cm)				**H_2Od P=6 bar (h=42cm)**			
Sample	**Da (μm)**	**MMAD (μm)**	**GSD**	**Sample**	**Da (μm)**	**MMAD (μm)**	**GSD**
21	4.54	10.4	2.09	26	4.79	11.1	2.00
22	4.77	11.1	2.08	27	4.88	10.7	1.89
23	4.76	11.0	2.08	28	4.86	10.5	1.86
24	4.83	11.1	2.04	29	4.89	10.1	1.84
25	4.91	11.1	1.98	30	4.79	10.4	1.87
MEAN	**4.76**	**10.94**	**2.18**	**MEAN**	**4.84**	**10.56**	**1.89**
SD	**0.14**	**0.30**	**0.03**	**SD**	**0.05**	**0.37**	**0.06**

Table 2.3: H_2Od experimental results with driving pressures of P=5 bar and P=6 bar.

Both PFC compounds, PFD and FC75, were tested at driving pressures of 4-5 bar, as shown in Tables 2.4 - 2.7. The optimal distance to get a concentration close to the 1000 droplets/cm^3 recommended was 60 mm and 52 mm, for PFD and FC75 respectively. Initially, for FC75, measurements were taken at higher distances. However, a very low droplet concentration was observed that could be explained by the high volatility of the compound. For both PFCs, the D_a value decreased when the driving pressure was increased from 4 bar to 5 bar at the optimal distance (See Tables 2.6-2.7). From 4.33±0.03 μm to 4.18±0.03 μm with PFD and from 2.45±0.01 μm to 2.28±0.02 μm with FC75. Regarding the MMAD, PFD showed more stable values with an increase in the driving pressure applied to the IC-1.1, from 7.21±0.02 μm (4 bar) to 7.14±0.05 μm (5 bar). However, with FC75, the MMAD value showed a significantly decrease with an increase in the driving pressure, from 10.01±0.44 μm (4 bar) to 4.83±0.17 μm (5 bar).

Additionally, measurements at 30 mm and 46 mm were taken for the PFD compound to study the influence of the distance between the distal tip of the IC-1.1 and the APS inlet nozzle and to compare the results with the numerical model presented in the next section.

PFD P=4 bar (h=30mm)				**PFD P=5 bar (h=30mm)**			
Sample	**Da (μm)**	**MMAD (μm)**	**GSD**	**Sample**	**Da (μm)**	**MMAD (μm)**	**GSD**
1	3.96	7.07	1.99	6	3.97	6.27	1.80
2	4.13	6.61	1.76	7	3.99	6.33	1.82
3	4.09	6.46	1.73	8	3.98	6.32	1.82
4	4.12	6.55	1.74	9	3.93	6.21	1.82
5	4.09	6.50	1.74	10	3.96	6.36	1.84
MEAN	**4.08**	**6.64**	**1.79**	**MEAN**	**3.97**	**6.30**	**1.82**
SD	**0.07**	**0.25**	**0.11**	**SD**	**0.02**	**0.06**	**0.01**

Table 2.4: PFD experimental results at h=30mm with driving pressures of P=4 bar and P=5 bar.

PFD P=4 bar (h=46mm)				**PFD P=5 bar (h=46mm)**			
Sample	**Da (μm)**	**MMAD (μm)**	**GSD**	**Sample**	**Da (μm)**	**MMAD (μm)**	**GSD**
11	4.24	7.37	2.03	16	4.18	6.84	1.85
12	4.31	7.46	2.06	17	4.22	7.14	1.94
13	4.24	7.44	2.03	18	4.20	7.24	2.01
14	4.26	7.45	2.04	19	4.16	7.30	2.07
15	4.31	7.48	2.02	20	4.16	7.37	2.09
				21	4.28	7.44	2.11
				22	4.10	6.83	1.85
				23	4.13	6.91	1.86
MEAN	**4.27**	**7.44**	**2.04**	**MEAN**	**4.22**	**7.13**	**1.97**
SD	**0.04**	**0.04**	**0.02**	**SD**	**0.08**	**0.24**	**0.11**

Table 2.5: PFD experimental results at h=46mm with driving pressures of P=4 bar and P=5 bar.

PFD P=4 bar (h=60mm)				**PFD P=5 bar (h=60mm)**			
Sample	**Da (μm)**	**MMAD (μm)**	**GSD**	**Sample**	**Da (μm)**	**MMAD (μm)**	**GSD**
24	4.30	7.24	1.95	29	4.18	7.20	1.99
25	4.36	7.22	1.89	30	4.22	7.12	1.95
26	4.30	7.19	1.93	31	4.20	7.17	1.95
27	4.33	7.21	1.91	32	4.16	7.10	1.93
28	4.35	7.20	1.91	33	4.16	7.09	1.94
MEAN	**4.33**	**7.21**	**1.92**	**MEAN**	**4.18**	**7.14**	**1.95**
SD	**0.03**	**0.02**	**0.02**	**SD**	**0.03**	**0.05**	**0.02**

Table 2.6: PFD experimental results at h=60mm (optimal distance) with driving pressures of P=4 bar and P=5 bar.

FC75 P=4 bar (h=52mm)				**FC75 P=5 bar (h=52mm)**			
Sample	**Da (μm)**	**MMAD (μm)**	**GSD**	**Sample**	**Da (μm)**	**MMAD (μm)**	**GSD**
1	2.47	10.50	1.70	6	2.28	5.06	1.62
2	2.45	10.10	1.69	7	2.32	4.89	1.62
3	2.44	10.30	1.70	8	2.27	4.88	1.60
4	2.45	9.73	1.68	9	2.27	4.60	1.60
5	2.43	9.42	1.68	10	2.27	4.74	1.60
MEAN	**2.45**	**10.01**	**1.69**	**MEAN**	**2.28**	**4.83**	**1.61**
SD	**0.01**	**0.44**	**0.01**	**SD**	**0.02**	**0.17**	**0.01**

Table 2.7: FC75 experimental results at h=52mm (optimal distance) with driving pressures of P=4 bar and P=5 bar.

Figure 2.9 summarizes the $\bar{\mathrm{D}}_a$ and MMAD results obtained with the IC-1.1 for the three compounds studied, H_2Od, PFD and FC75.

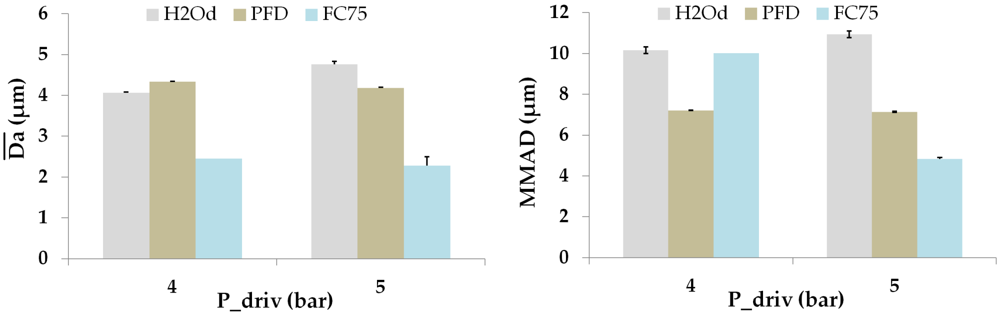

(a)

(b)

Figure 2.9: (a) $\bar{\mathrm{D}}_a$ and (b) MMAD results obtained at the optimal distance for each compound and driving pressure. Values are given as mean ± standard deviation.

These experimental results were used subsequently to validate the numerical model presented in Section 2.2 of the current chapter. Furthermore, measurements at nozzle level (h=0) were taken to define the initial conditions of the injectors that will represent the population of droplets in the numerical model. Even though the average droplet concentration measured at this point was higher than the recommended, the vast majority of them were grouped in the second event, which classifies the droplets within the measurement range from 0.5 μm to 20 μm.

2.2 Numerical Model

In addition to the experimental model, CFD tools have been used to study more in detail the aerosol characteristics produced with the IC-1.1. This numerical model, which has been validated with the experimental data obtained in the previous section, will be helpful in the study of future nebulizer prototypes as well as to carry out parametric studies to achieve the optimal aerosol delivery in preterm babies with RDS. The CFD analysis to study the flow behavior involves three main elements: pre-processor, solver and post-processor (See Figure 2.10).

The **pre-processing** consists in the definition of the geometry of the region of interest (*computational domain*), the discretization of this domain into a number of smaller, non-overlapping subdomains (*mesh generation*) and the specification of appropiate *boundary conditions*. Then, the **solver** proceeds to the discretization of the differential equations of the flow by means of the *Finite Volume Method (FVM)* along with the definition of interpolation schemes. In the case of unsteady flows, as the aerosols developed with the IC-1.1, a *temporal discretization* is also necessary as well as a *parcel discretization* which represents the discrete phase. The resolution of the numerical model requires an iterative process and the *convergence* of the solution is commonly assesed by progressively tracking the imbalances of the algebraic equations through each iteration step. The **post-process** involves the quantification of the results and their validation with the experimental results obtained previously.

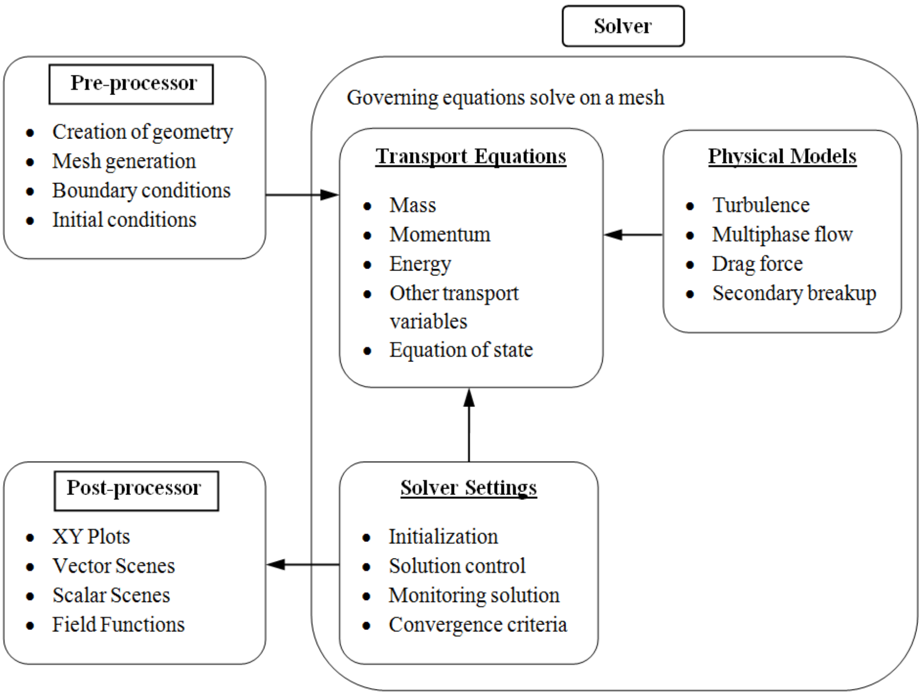
Solver
Pre-processor
Creation of geometry
Mesh generation
Boundary conditions
Initial conditions
Governing equations solve on a mesh
Transport Equations
Mass
Momentum
Energy
Other transport variables
Equation of state
Physical Models
Turbulence
Multiphase flow
Drag force
Secondary breakup
Post-processor
XY Plots
Vector Scenes
Scalar Scenes
Field Functions
Solver Settings
Initialization
Solution control
Monitoring solution
Convergence criteria

Figure 2.10: CFD analysis framework and the interconnectivity functions of the three main elements involved.

CFD tools have emerged as a viable approach for either industrial and research applications as a result of the constant improvement of digital workstations and computational resources. With the introduction of new solvers and theoretical physics models, CFD techniques allow to study alternative designs under a wide range of parameters and conditions. In the current thesis, the CFD commercial code STAR-CCM+ v.11.06 [104] has been used to develop all the steps of the numerical model. An Intel Xeon E5-2630 v3 2.4 GHz CPU computer with 32 GB RAM has been used to run all the simulations.

2.2.1 Computational Domain and Boundary Conditions

The first step in any CFD analysis is the definition and creation of the computational domain. The Lagrangian multiphase simulations that are needed to simulate an aerosol of these characteristics involve a high computational cost due to the solution of the trajectory of each of the discrete droplets of the aerosol. For that reason, it has been assumed an **axisymmetrical computational domain** with an outer ring instead of the six original lumens, as illustrated in Figure 2.11.

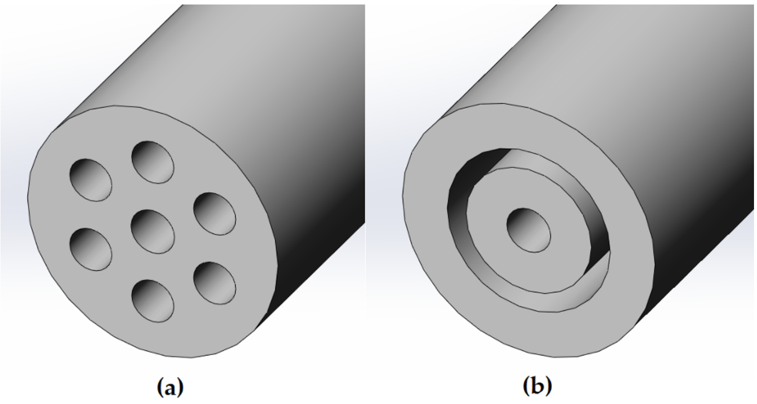

Figure 2.11: (a) Cross section of the IC-1.1 tip and (b) the assumption defined for the generation of the axisymmetrical computational domain.

The width of this ring was calculated in order to have the same area of the six original outer lumens and, therefore, to supply the same air mass flow.

Original outer lumen area

$$\frac{\pi \cdot d^2}{4} = \frac{\pi \cdot 66.4^2 \mu m}{4} = 3462,789\, \mu m^2$$

$$\text{With 6 lumens: } 3462,789 \frac{\mu m^2}{lumen} \cdot 6 \text{ lumens} = \mathbf{20776,73\, \mu m^2}$$

where d is the diameter of each of the six outer lumens in the distal tip.

Assumed ring area

$$\frac{\pi \cdot [(2 \cdot b_{lcen}) + d]^2}{4} = \frac{\pi \cdot (225.2 + 66.4)^2 \mu m}{4} = 66782,845\, \mu m^2$$

$$\frac{\pi \cdot [(2 \cdot b_{lcen}) - d]^2}{4} = \frac{\pi \cdot (225.2 - 66.4)^2 \mu m}{4} = 19805,731\, \mu m^2$$

$$66782,845\, \mu m^2 - 19805,731\, \mu m^2 = \mathbf{46977,11\, \mu m^2}$$

where b_{lcen}, which defines the position of the outer lumen, has been maintained with respect to the original geometry. Then, to calculate the ring width keeping the original total outer lumen area:

$$\frac{\pi \cdot (225,2 + x)^2}{4} - \frac{\pi \cdot (225.2 - x)^2}{4} = 20776,73\, \mu m^2$$

$$x = 29,3669\, \mu m \approx \mathbf{29,4\, \mu m = ring\ width}$$

Thus, the ring, defined as $(r_2 - r_1)$ has a width of 29,4 μm, where

$$r_1 = 112,6\, \mu m - \frac{29,4\, \mu m}{2} = 97,9\, \mu m$$

$$r_2 = 112,6\, \mu m + \frac{29,4\, \mu m}{2} = 127,3\, \mu m$$

Figure 2.12 shows the original geometry of the IC-1.1 and how it has been transformed in order to replace the six outer lumens with an outer ring of the same area.

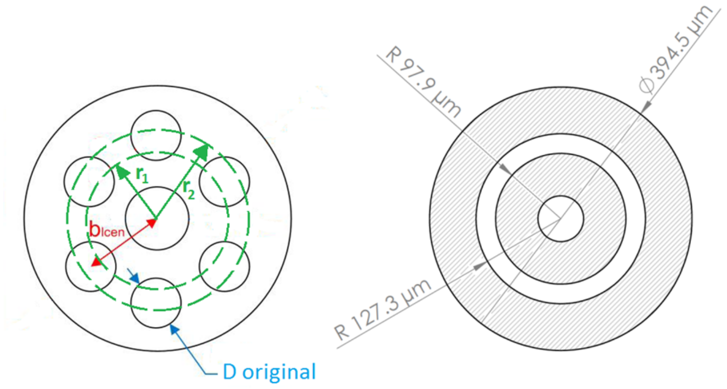
r1
r2
blcen
D original
R 97.9 µm
Ø394.5 µm
R 127.3 µm

Figure 2.12: Transformation of the six outer lumens into an outer ring to carry out the numerical study.

The computational domain consists of the last 2 mm of the IC-1.1 and the downstream region beyond the catheter tip, as shown in Figure 2.13. The optimal distance used in the experimental setup to obtain the average recommended particle concentration with the APS has been used to define the outlet boundary condition, which has been located at L=60 mm and L=52 mm for PFD and FC75, respectively.

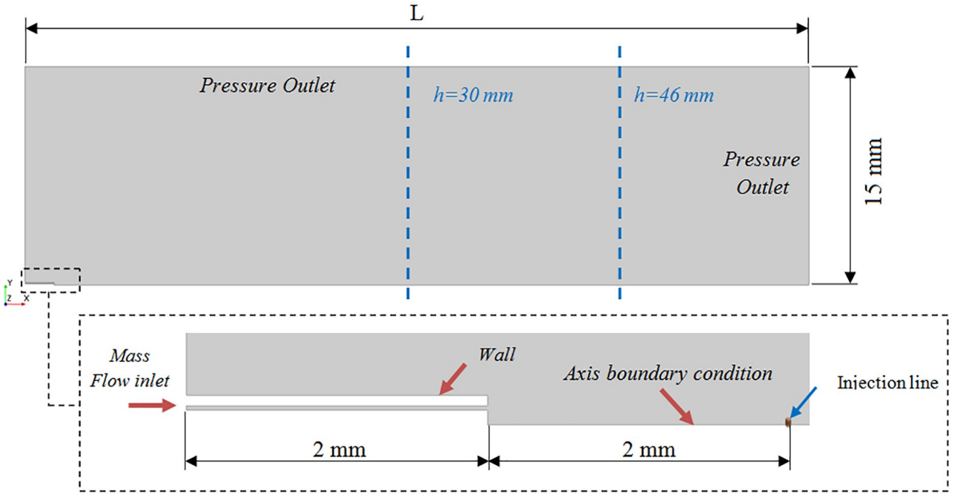
L
Pressure Outlet
h=30 mm
h=46 mm
Pressure Outlet
15 mm
Y
Z X
Mass Flow inlet
Wall
Axis boundary condition
Injection line
2 mm
2 mm

Figure 2.13: Computational domain and boundary conditions.

An air mass flow rate of $\dot{m}_{air}$=1.1344$\cdot 10^{-5}$ kg/s, previously measured with a pressure of 4 bar in the study of Goikoetxea et al. [98], and of $\dot{m}_{air}$=1.14766$\cdot 10^{-5}$ kg/s with a pressure of 5 bar has been used to define the inlet boundary condition. In addition, an axisymmetrical boundary condition has been fixed along the central axis and an atmospheric pressure outlet condition has been set for the downstream boundaries.

For the representation of the discrete phase droplets, ten droplet injectors have been created and uniformly distributed through an injection line, whose length is equal to the radius of the central lumen of the IC-1.1 (34.3 μm). The ten injections have been defined using the experimental results obtained with the APS at the nozzle level (h=0) and interpolating the data from the 52 intervals of the APS sample chosen. They were set at a distance of 2 mm from the catheter tip as an approximated value between the APS nozzle, where the catheter tip was placed to take the measurements, and the APS laser beams which measure the distribution of the droplets.

The non-slip condition has been established on the walls. According to this condition, the flow adjacent to the wall has the same velocity as the wall, in this case null. The temperature of the walls has been set to 293K and a turbulence intensity of 0.07 has been defined, based on the hydraulic diameter (D$_h$) calculated as the difference of the outer and inner diameter of the ring.

$$I = 0.16 \left(Re_{Dh}\right)^{-1/8} \tag{2.2}$$

Other possible interaction mechanisms, which have not been considered in the current numerical model, are the collision of the droplets as well as the formation of a liquid film.

The velocity of the droplets injected through the injection line has been set equal to the velocity of the airflow at this position. The droplet mass and size distribution values of these initial injections, obtained from the experimental measurements, are defined in Table 2.8 for each PFC compound.

	PFD			**FC75**		
INJ	**Dg (μm)**	**$\dot{m}$ (kg/s)**		**Dg (μm)**	**$\dot{m}$ (kg/s)**	
		4 bar	**5 bar**		**4 bar**	**5 bar**
1	0.375	$1.43 \cdot 10^{-9}$	$6.08 \cdot 10^{-12}$	0.392	$5.44 \cdot 10^{-9}$	$2.53 \cdot 10^{-11}$
2	0.577	$9.02 \cdot 10^{-10}$	$1.49 \cdot 10^{-11}$	0.604	$4.27 \cdot 10^{-9}$	$8.35 \cdot 10^{-11}$
3	0.828	$1.18 \cdot 10^{-8}$	$2.77 \cdot 10^{-10}$	0.866	$5.04 \cdot 10^{-8}$	$1.48 \cdot 10^{-9}$
4	1.275	$9.35 \cdot 10^{-8}$	$4.82 \cdot 10^{-9}$	1.335	$3.84 \cdot 10^{-7}$	$2.48 \cdot 10^{-8}$
5	1.825	$2.87 \cdot 10^{-7}$	$3.30 \cdot 10^{-8}$	1.910	$1.09 \cdot 10^{-6}$	$1.61 \cdot 10^{-7}$
6	2.810	$5.14 \cdot 10^{-7}$	$1.91 \cdot 10^{-7}$	2.945	$1.91 \cdot 10^{-6}$	$9.76 \cdot 10^{-7}$
7	4.330	$1.79 \cdot 10^{-7}$	$5.77 \cdot 10^{-7}$	4.535	$1.00 \cdot 10^{-6}$	$2.49 \cdot 10^{-6}$
8	6.205	$5.26 \cdot 10^{-8}$	$4.64 \cdot 10^{-7}$	6.495	$2.46 \cdot 10^{-7}$	$1.93 \cdot 10^{-6}$
9	9.555	$1.21 \cdot 10^{-7}$	$1.44 \cdot 10^{-7}$	10.000	$2.57 \cdot 10^{-7}$	$5.52 \cdot 10^{-7}$
10	14.19	$2.31 \cdot 10^{-8}$	$1.72 \cdot 10^{-8}$	14.850	$7.81 \cdot 10^{-8}$	$6.37 \cdot 10^{-8}$
Total mass flow rate		$1.28 \cdot 10^{-6}$	$1.43 \cdot 10^{-6}$		$5.03 \cdot 10^{-6}$	$6.20 \cdot 10^{-6}$

Table 2.8: Droplet initial conditions for PFD and FC75 compounds obtained from experimental measurements.

2.2.2 Mesh Generation

The mesh generation represents one of the most important steps during the pre-process part before running the numerical solution. The CFD code requires the division of the computational domain in smaller subdomains in order to solve the flow physics. In this thesis, polygonal cells have been used with a mesh refinement in the region close to the catheter tip and all along the central axis, as shown in Figure 2.14. To ensure that the numerical solution is independent of the mesh size, a mesh dependency study has been carried out following the procedure of Richardson's extrapolation [105]. Three different mesh levels were created (coarse, medium and fine) with mesh sizes h_3, h_2 and h_1, respectively. The mesh refinement ratio is given by the Equation 2.3.

$$\text{Mesh refinement ratio} = r = \frac{h_2}{h_1} \tag{2.3}$$

The axial velocity in a point at the outlet was the parameter chosen to control the study. Tables 2.9 - 2.11 show the results obtained for the FC75 compound with a driving pressure of 5 bar.

Mesh	**Number of cells**	$\mathbf{v_{axial}}$**(m/s)**
M1	404.620	9.58
M2	196.107	9.41
M3	98.854	8.92

Table 2.9: Axial velocity values in the chosen point for each mesh level.

The extrapolated axial velocity value was calculated by Equation 2.4

$$(v_{axial})_{h=0} = (v_{axial})_1 + \frac{(v_{axial})_1 - (v_{axial})_2}{r^p - 1} \tag{2.4}$$

where p is the order of convergence, defined as:

$$p = \frac{ln\left(\frac{(v_{axial})_3 - (v_{axial})_2}{(v_{axial})_2 - (v_{axial})_1}\right)}{ln2} \tag{2.5}$$

The discretization error of the computed solution was calculated using the grid convergence index (GCI) with the three levels of mesh previously defined (See Equations 2.6 - 2.7). A small value of GCI indicates that the solution is within the asymptotic range of convergence [106].

$$\begin{aligned} GCI_{12} &= F_s \frac{\left|(v_{axial})_1 - \frac{(v_{axial})_2}{(v_{axial})_1}\right|}{r^p - 1} \cdot 100 \\ GCI_{23} &= F_s \frac{\left|(v_{axial})_2 - \frac{(v_{axial})_3}{(v_{axial})_2}\right|}{r^p - 1} \cdot 100 \end{aligned} \tag{2.6}$$

$$\frac{GCI_{23}}{r^p \cdot GCI_{12}} \approx 1 \tag{2.7}$$

	$\mathbf{V_{axial}}$(m/s)	**Error (%)**
$(\mathbf{v_{axial}})_{\mathbf{h=0}}$ **(m/s)**	9.67	
M1	9.58	0.93
M2	9.41	2.69
M3	8.92	7.76

Table 2.10: Errors obtained for each mesh level.

	Domain
$\mathbf{GCI_{12}}$ **(%)**	1.21
$\mathbf{GCI_{23}}$ **(%)**	3.65
$\frac{\mathbf{GCI_{23}}}{\mathbf{r^p \cdot GCI_{12}}}$ **(-)**	1.05

Table 2.11: Grid Convergence Index (GCI) results.

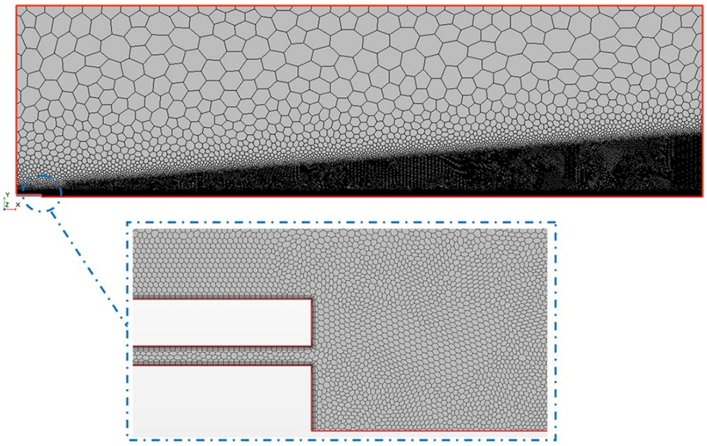

Figure 2.14: Mesh generated by means of polygonal cells and with a mesh refinement all along the central axis.

The mesh level M1, with 404.620 cells, was chosen to create the numerical model taking into consideration the error obtained for each mesh level, and that the $GCI_{23}/r^p \cdot GCI_{12}$ relation was close to 1 (See Tables 2.10 - 2.11).

2.2.3 Physics Models

This section describes the physics models that have been introduced to define the numerical model. The aerosol produced with the IC-1.1 generates a **multiphase flow** with a continuous phase (air flow) and a discrete phase (PFC droplets). The Eulerian approach has been used to define the continuous phase whereas the Lagrangian approach has been used to define the discrete phase formed by the PFC droplets. Initially, the governing equations for the continuous phase are described along with the turbulence modeling. Then, the discrete phase modeling is discussed, with the definition of the Lagrangian multiphase model employed, the governing equations for the discrete phase, the turbulent dispersion and the interaction between the continuous and dispersed phase.

2.2.3.1 Governing equations for the continuous phase

The **Eulerian approach** has been used for the resolution of the continuous phase, which consists of analyzing the airflow in a control volume or flow domain. The main variables that arise when solving a continuous flow are the velocity fields (u, v, w) and pressure (P). In this specific case, the velocities reached by the IC-1.1 in the distal region of the catheter make it necessary to consider the effects of air compressibility and, therefore, consider that the density of the fluid is function of temperature and pressure. Hence, along with pressure and velocity new flow variables appear as the temperature (T), density (ρ), specific internal energy (e) and specific enthalpy (h).

These flow variables appear in the Navier-Stokes equations, which describe the motion of fluid droplets. For motion in a compressible medium, the CFD code must solve the governing equations of conservation of mass, momentum and energy (See Equations 2.8 - 2.10) [107].

$$\frac{\partial \rho}{\partial t} + \frac{\partial (\rho u_i)}{\partial x_i} = 0 \tag{2.8}$$

$$\frac{\partial (\rho u_i)}{\partial t} + \frac{\partial (\rho u_i u_j)}{\partial x_j} = -\frac{\partial P}{\partial x_i} + \frac{\partial t_{ij}}{\partial x_j} + F \tag{2.9}$$

$$\begin{aligned}\frac{\partial}{\partial t}\left[\rho\left(e + \frac{1}{2}u_i u_i\right)\right] + \frac{\partial}{\partial x_j}\left[\rho u_j\left(h + \frac{1}{2}u_i u_i\right)\right] \\ = \frac{\partial}{\partial x_j}(u_i t_{ij}) + \frac{\partial}{\partial x_j}\left(\kappa \frac{\partial T}{\partial x_j}\right) + Q\end{aligned} \tag{2.10}$$

where κ is thermal conductivity, t_{ij} is the instantaneous viscous stress sensor and F and Q are the terms that model the exchange of energy and momentum with the discrete phase. The constitutive relation between stress and strain rate for a Newtonian fluid is given by Equation 2.11.

$$t_{ij} = 2\mu s_{ij} - \frac{2}{3}\mu \frac{\partial u_k}{\partial x_k}\delta_{ij} \tag{2.11}$$

where s_{ij} is the instantaneous strain-rate tensor, given by Equation 2.12.

$$s_{ij} = \frac{1}{2}(\frac{\partial u_i}{\partial x_j} + \frac{\partial u_j}{\partial x_i}) \tag{2.12}$$

Considering the air flow an ideal gas, three equations of state have been included in the Navier-Stokes equations that relate the thermodynamic variables, as shown in Equations 2.13 - 2.15. Thus, a system of eight equations with eight unknown variables is obtained.

$$P = \rho R T \tag{2.13}$$

$$e = c_v T \tag{2.14}$$

$$h = c_p T \tag{2.15}$$

where R is the ideal gas constant, c_v the specific heat for constant volume and c_p the specific heat for constant pressure.

All these equations have to be adapted to take into account the flow turbulence, according to the way chosen to carry out the modeling. Thus, new equations are also necessary to solve the new turbulent variables that will appear.

2.2.3.2 Turbulence modeling

The fluid regime depends on the value of Reynolds number (Re), a dimensionless number which is defined as the ratio of inertial forces to viscous forces, as shown in Equation 2.16.

$$Re = \frac{vL}{\nu} = \frac{\text{inertial forces}}{\text{viscosity forces}} \tag{2.16}$$

where L is a characteristic linear dimension, v is the characteristic velocity of the object relative to the fluid and ν is the kinematic viscosity.

At larger Reynolds numbers, the fluid's inertia overcomes the viscous stresses, and the laminar motion becomes unstable. Large velocity and pressure fluctuations appear and the motion becomes inherently three dimensional and unsteady. When this occurs the motion is described as **turbulent** [108].

Different methodologies are used to resolve a turbulent flow. The most accurate option is the **Direct Numerical Simulation (DNS)**, which means a complete three dimensional and time-dependent solution of the Navier-Stokes and continuity equations. All scales of turbulence are resolved without modeling. Another option is the **Large Eddy Simulation (LES)**, where the largest eddies are resolved and the smallest eddies are modeled. These two methodologies achieve very accurate solutions, even though their computational cost is very high, especially in DNS.

Any time and space dependent flow variable ($\phi(x,t)$) can be written as the sum of an average ($\bar{\phi}(x)$) and a fluctuation ($\phi^{'}(x,t)$), as shown in Equation 2.17.

$$\phi(x,t) = \bar{\phi}(x) + \phi^{'}(x,t) \tag{2.17}$$

This decomposition yields a set of equations governing the average flow field, called the **Reynolds Averaged Navier Stokes Equations (RANS)**. With a RANS approach all turbulent scales are modeled and, therefore, the computer demands decrease substantially. RANS-models can be divided into two major categories, the Eddy Viscosity Models (EVM) and the Reynolds Stress Transport Models (RSTM). The RSTM use more transport equations and achieve more accurate results, dealing with the isotropy of turbulence and the extra strains. However, the EVM demands less computational cost, they are robust and even though they do not calculate with precision the Reynolds stresses they predict quite well the average values of the variables. The most common EVM is known as the Boussinesq approximation, which considers that it exists an analogy between the molecular gradient-diffusion process and turbulent motion.

$$-\bar{\rho}\tau_{ij} = 2\mu_t\left(S_{ij} - \frac{1}{3}\frac{\partial \tilde{u}}{\partial x_k}\delta_{ij}\right) - \frac{2}{3}\bar{\rho}k\delta_{ij} \tag{2.18}$$

$$S_{ij} = \frac{1}{2}\left(\frac{\partial \tilde{u}_i}{\partial x_j} + \frac{\partial \tilde{u}_j}{\partial x_i}\right) \tag{2.19}$$

where μ_t is the turbulent eddy viscosity and S_{ij} is the mean strain rate tensor given by Equation 2.19.

While some simpler models rely on the concept of mixing length to model the turbulent viscosity in terms of mean flow mean quantities, the EVM solve additional transport equations for scalar quantities that enable the turbulence to be derived. In this thesis, the EVM with two transport equation have been chosen to define the turbulence modeling by means of the **Realizable K-Epsilon Two-Layer turbulence model**.

k-ϵ turbulence model

The k-ϵ turbulence model is a two-equation model that solves transport equations for the turbulent kinetic energy (k) and the turbulent dissipation rate (ϵ) in order to determine the turbulent eddy viscosity. It relates the turbulent eddy viscosity μ_t, the turbulent kinetic energy k and the dissipation rate ϵ by means of Equation 2.20.

$$\mu_t = \rho\, C_\mu \frac{k^2}{\epsilon} \tag{2.20}$$

The Realizable k-ϵ model contains a new transport equation for the turbulent dissipation rate ϵ. Adittionally, a critical coefficient of the model C_μ is expressed as a function of mean flow and turbulence properties, rather than assumed to be constant as in the standard k-ϵ model. Equations 2.21 - 2.22 represent the transport equations for the turbulent kinetic energy (k) and the turbulent dissipation rate (ϵ), respectively.

$$\frac{\partial}{\partial t}(\rho k) + \frac{\partial}{\partial x_i}(\rho k u_i) = \frac{\partial}{\partial x_j}\left[\left(\mu + \frac{\mu_t}{\sigma_k}\right)\frac{\partial k}{\partial x_j}\right] - \rho\epsilon - Y_M + G_k \tag{2.21}$$

$$\begin{aligned}\frac{\partial}{\partial t}(\rho\epsilon) + \frac{\partial}{\partial x_j}(\rho\epsilon u_j) &= \frac{\partial}{\partial x_j}\left[\left(\mu + \frac{\mu_t}{\sigma_\epsilon}\right)\frac{\partial \epsilon}{\partial x_j}\right] \\ &+ C_{\epsilon 1}\,\frac{\epsilon}{k}\,G_\epsilon - C_{\epsilon 2}\,f_2\,\rho\left(\frac{\epsilon}{T_\epsilon} - \frac{\epsilon_0}{T_0}\right)\end{aligned} \tag{2.22}$$

with the following coefficients values:

$$C_{\epsilon 1} = 1.44;\;\; C_{\epsilon 2} = 1.9;\;\; C_\mu = 0.09;\;\; \sigma_k = 1.0;\;\; \sigma_\epsilon = 1.2$$

Y_M and G_k are production terms to represent the compressibility modification and turbulent production, respectively, whereas T_ϵ is the large-eddy time scale.

$$G_k = 2\mu_t S_{ij} S_{ij} \tag{2.23}$$

$$Y_M = \frac{C_M k \epsilon}{c^2} \tag{2.24}$$

$$T_\epsilon = \frac{k}{\epsilon} \tag{2.25}$$

where c is the speed of sound and C_M is a coefficient value ($C_M = 2$)

ϵ_0 is the ambient turbulence value in the source terms that counteracts turbulence decay. The possibility to impose an ambient source term also leads to the definition of a specific time-scale T_0 that is defined as:

$$T_0 = max\left(\frac{k_0}{\epsilon_0}, C_t\sqrt{\frac{v}{\epsilon_0}}\right) \tag{2.26}$$

where C_t is a model coefficient that for the k-ϵ turbulence model takes a value of C_t=1.

The transport equation for the turbulent kinetic energy (k) is insensitive, by construction, to stabilizing and destabilizing effects usually associated with strong streamline curvature and frame rotation. These effects can be incorporated by using a curvature correction factor, which alters the turbulent kinetic energy production term according to the local rotation and vorticity rates. The curvature correction factor f_c is calculated as:

$$f_c = min\left(C_{max}, \frac{1}{C_{r_1}\left(|\eta| - \eta\right) + \sqrt{1 - min\left(C_{r_2}, 0.99\right)}}\right) \tag{2.27}$$

Wall treatment

Walls are a source of vorticity and, therefore, an accurate predicition of flow and turbulence parameters across the wall boundary layer is essential. Close to the wall the mean flow velocity (U) only depends on the distance y from the wall, the fluid density ρ and viscosity μ and the wall shear stress τ_w. Dimensional analysis shows the so-called **law of the wall** and contains the definitions of two important dimensionless groups, u^+ and y^+ (See Equation 2.28) [109].

$$u^+ = \frac{U}{u_\tau} = f\left(\frac{\rho u_\tau y}{\mu}\right) = f(y^+) \tag{2.28}$$

where u_τ is the so-called friction velocity defined as:

$$u_\tau = \sqrt{\frac{\tau_w}{\rho}} \tag{2.29}$$

The inner region of the boundary layer can be divided into three sublayers. The *viscous sublayer* is the fluid layer in contact with the wall, which is dominated by viscous effects and is almost laminar. The *buffer layer*, a transitional layer where viscous and turbulent effects are equally important and the *log-law layer*, mainly affected by turbulent effects (See Figure 2.15). The non-dimensional wall distance y^+, given by Equation 2.30, is used to define the extents of the sublayers.

$$y^+ = \frac{u_\tau y}{\nu} \tag{2.30}$$

Two types of wall laws are used in STAR-CCM+. *Standard wall laws*, used with $high - y^+$ wall treatments and *blended wall laws* used with $all - y^+$ wall treatments, which include a buffer region that smoothly blends the laminar and turbulent profiles together.

Two-layer approach

The two-layer approach, first suggested by Rodi [110], is an alternative to the low Reynolds number approach that allows the k-ϵ model to be applied in the viscous-affected layer (including the viscous sub-layer and the buffer layer). In this approach, the computation is divided into two layers. In the layer next to the wall, the turbulent dissipation rate (ϵ) and the turbulent viscosity (μ_t) are specified as functions of wall distance. The ϵ values specified in the near-wall layer are blended smoothly with the values computed from solving the transport

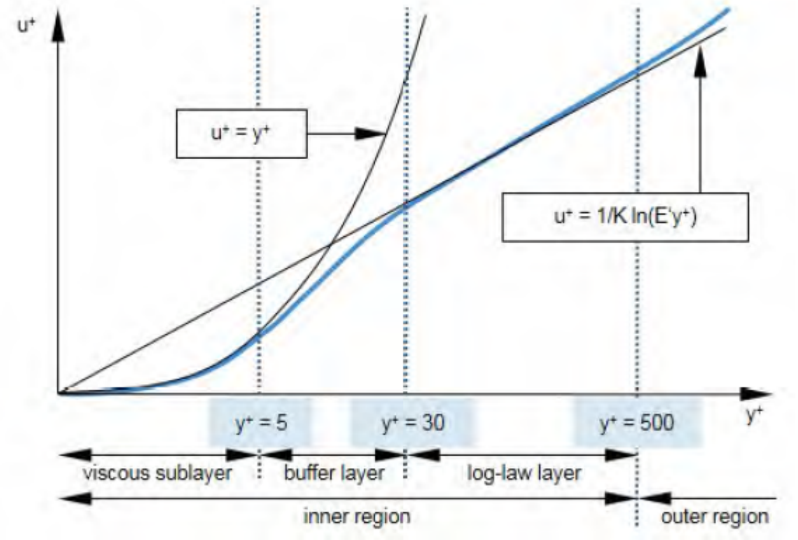

Figure 2.15: Subdivisions of the near-wall treatment. Source: STAR-CCM+

equation far from the wall. The equation for the turbulent kinetic energy (k) is solved across the entire flow domain. For the two-layer models the dissipation rate near the wall is prescribed as:

$$\epsilon = \frac{k^{3/2}}{l_\epsilon} \tag{2.31}$$

where l_ϵ is a length scale function that is calculated depending on the model variant. The CFD code used provides three variants of two-layer models (Wolfstein model, Norris-Reynolds model and Xu model). In this thesis, the Wolfstein two-layer model [111] has been used where the length scale function (l_ϵ) is defined by means of Equation 2.32.

$$l_\epsilon = c_l d \left[1 - e^{\left(-\frac{Re_d}{2c_l}\right)} \right] \tag{2.32}$$

$$c_l = 0.42\ C_\mu^{-3/4} \tag{2.33}$$

2.2.3.3 Discrete phase modeling: Lagrangian multiphase model

Multiphase flows can be classified into two categories: *stratified flows*, such as free surface flows or annular film flow in pipes and *dispersed flows* such as droplet flows as the aerosol generated by means of the IC-1.1.

STAR-CCM+ provides different models depending on the characteristics of the multiphase flow. The **Volume-of-fluid (VOF) model** is designed to capture the interface between two immiscible fluids and, therefore, is suitable for multiphase flows where two fluids are clearly and sharply separated, which is not the case of the the dispersed flow generated by the IC-1.1.

For dispersed flows, it can be used either the **Lagrangian multiphase model (LMP)** or the **Eulerian multiphase model (EMP)**. The EMP considers the droplets in terms of concentration (volume fraction) and averaged velocity. This model is more economical than the LMP, particularly for flows with high droplet concentrations. This model is based on a Eulerian-Eulerian formulation where each phase has its own set of conservation equations. Phases are considered to be mixed on length scales smaller than the length scales resolved by the grid, and coexist everywhere in the flow domain. This model is suitable to flows where each phase can be considered continuously mixed, for instance, a cloud of sand that is transported by wind, bubbles moving inside liquids or two liquids in a mixer or separator.

The LMP solves the trajectories of each droplet which is assumed to be spherical and smaller than the cell size. This model allows to track the movement of individual droplets in fine detail. Each track is calculated based on the Lagrangian formulation. In order to save computational time, all the droplets are grouped in numerical parcels, each of them constituted of several non-interacting identical droplets. A key assumption of this model is that the volume fraction of the Lagrangian phase in each cell has to be smaller than 40%. In the study of Goikoetxea et al. [98] it was found that the volume of compound nebulized by the IC-1.1 was less than 0.5% of total volume independently of the compound and pressure used.

Therefore, it has been considered the LMP model as the most suitable choice to create the numerical model of the aerosols produced with the IC-1.1.

2.2.3.4 Droplet equations of motion

The conservation equation of momentum for a droplet is written in the Lagrangian framework. The change in momentum is balanced by surface and body forces that act on the droplet. The equation of conservation of momentum for a material droplet of mass m_p is given by:

$$m_p \frac{dv_p}{dt} = F_s + F_b \tag{2.34}$$

where v_p denotes the instantenous droplet velocity, F_s is the resultant of the forces that act on the surface of the droplet and F_b is the resultant of the body forces.

$$F_s = F_D + F_p + F_{vm} \tag{2.35}$$

where F_D is the drag force, F_p is the pressure gradient force and F_{vm} is the virtual mass force.

Much of the work in aerosol science is based on two assumptions [112]: (1) The droplet is assumed to be spherical, which is quite reasonable since such small liquid droplets are spherical and (2) the droplet density is assumed to be much larger than the surrounding fluid density. The second assumption (i.e. $\rho_{droplet} >> \rho_{air}$) is acceptable, since the densities of the compounds analyzed in the numerical study, PFD and FC75, are between 1000-2000 times the air density ($\rho_{PFD} = 1950 kg/m^3$; $\rho_{FC75} = 1780 kg/m^3$) and, therefore, $\rho_{droplet} \sim 10^3 \rho_{air}$. This assumption simplifies the analysis since surface forces as F_p and F_{vm} become insignificant [113]. Therefore, the droplet force balance equation is reduced to:

$$m_p \frac{dv_p}{dt} = F_D + F_b \tag{2.36}$$

The drag force (F_D) acts on the droplet in a uniform pressure field when there is no acceleration of the relative velocity between the droplet and the conveying fluid, air in this case. The force is quantified by the drag coefficient through the Equation 2.37.

$$F_D = \frac{1}{2} C_D \rho A_p v_{rel}^2 \tag{2.37}$$

where C_D is the drag coefficient of the droplet, ρ is the density of the continuous phase, A_p is the projected area of the droplet and v_{rel} is the relative velocity between the droplet and the air.

The drag coefficient (C_D) is a function of the small-scale flow features around the individual droplets. These features are impractical to resolve spatially and the usual practice is to obtain the drag coefficient from correlations, tipically derived from experiment or theoretical studies. The CFD code provides different methods for defining the drag coefficient depending on the nature of the dispersed phase. In this thesis, the Schiller-Naumann correlation [114] has been used, which is suitable for the spherical liquid droplets generated by means of the IC-1.1.

$$C_D = \begin{cases} \frac{24}{Re_d}\left(1 + 0.15 Re_d^{0.687}\right) & Re_d \leq 10^3 \\ 0.44 & Re_d > 10^3 \end{cases} \tag{2.38}$$

where Re_d is the droplet Reynolds number.

Regarding the body forces (F_b), the gravity force has not been included in the definition of the numerical study since it has been considered its effect as negligible due to the high velocity values obtained at the distal end of the IC-1.1. Other possible body forces, as Coulomb force, are not involved in this application. Therefore, body forces have not been included in the definition of the discrete phase.

2.2.3.5 Turbulent dispersion

A droplet in a turbulent flow experiences a randomly-varying velocity field to which it responds according to its inertia. This behaviour is modeled by a stochastic approach that includes the effect of instantaneous velocity fluctuations on the droplet. According to Gosman and Ioannides [115], a droplet is assumed to pass through a sequence of turbulent eddies as it traverses a turbulent flow field. Here, an eddy is a local disturbance to the Reynolds-averaged velocity field. The droplet remains in the eddy until either the eddy time-scale (τ_e) is exceeded, or the separation between the droplet and the eddy exceeds the length scale of the eddy (l_e). A droplet experiences an instantaneous fluid velocity v in each eddy, described as:

$$v = \bar{v} + v^{'} \tag{2.39}$$

where $\bar{v}$ is the local Reynolds-averaged velocity and $v^{'}$ is the eddy velocity fluctuation, unique to each droplet. The latter is a normal (Gausian) deviate with zero mean value and a standard deviation that comes from the eddy velocity scale

$$u_e = \frac{l_t}{\tau_t}\sqrt{\frac{2}{3}} \tag{2.40}$$

The turbulence model provides the length and time-scales of the turbulence, l_t and τ_t. Once generated, a single realization of $v^{'}$ continues to apply to a droplet until its eddy interaction time is exceeded:

$$\tau_l = min(\tau_e, \tau_c) \tag{2.41}$$

The eddy time-scale measures the lifetime of the eddy, i.e., the maximum interval over which a single realization of $v^{'}$ remains valid. It can be related to the diffusion of a passive scalar according to the underlying turbulence model, giving,

$$\tau_e = \frac{2\mu_t}{\rho u_e^2} \tag{2.42}$$

The droplets can interact with the eddy for less than the eddy time-scale when they have non-zero slip velocity, making it possible for the droplet to cross the eddy and espape. The edDy transit time is defined only for material droplets when the drag force is activated, in which case it is estimated from:

$$\tau_c = \begin{cases} \infty & \tau_v \leq \frac{l_e}{|v_s|} \\ -\tau_v ln\left(1 - \frac{l_e}{\tau_v |v_s|}\right) & \tau_v > \frac{l_e}{|v_s|} \end{cases} \tag{2.43}$$

where τ_v is the momentum relaxation time-scale.

2.2.3.6 Secondary breakup

Liquid droplets may break up under the action of non-uniform surface forces that are induced by their motion relative to the continuous phase. This phenomenon is known as **secondary breakup**. The response of droplets to non-uniform surface forces is invariably to deform, with the deformation resisted by the surface tension and viscous forces inside the droplet. This behaviour can be measured with the dimensionless Weber number (We) given by Equation 2.44.

$$We = \frac{\rho_g \left|v_{rel}\right|^2 D_p}{\sigma} \tag{2.44}$$

STAR-CCM+ provides different physics models for the numerical study of the breakup of liquid droplets in a gaseous stream. In the present numerical study, the secondary breakup has been modelled through the **Taylor Analogy Breakup (TAB) model**. This model uses the Taylor analogy described by O'Rourke et al. [116], which represents a distorting droplet as a damped spring-mass system. It considers only the fundamental mode of oscillation of the droplet whereas the displacement and velocity of the mass in the spring-mass system correspond to representative distortion and rate of distortion quantities for the droplet. Despite being based on a single mode of oscillation in the vibrational regime, the TAB model reproduces the same characteristic time-scales in low and high Weber number limits (We<100).

Droplet Distortion

The goal of the TAB distortion model is to calculate the instantaneous displacement x of the droplet equator from its equilibrium position. This displacement is illustrated in Figure 2.16. For simplicity of analysis, this displacement is normalized to the droplet diameter, as shown in Equation 2.45.

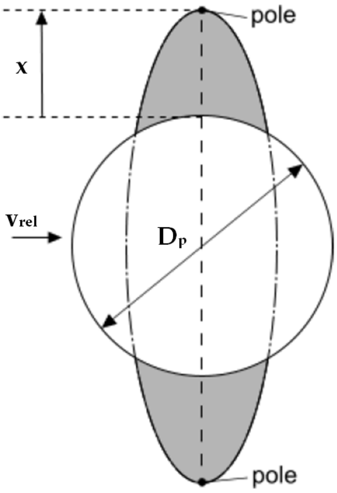

Figure 2.16: Illustration of the droplet distortion.

$$y = \frac{2x}{C_b \cdot D_p} \tag{2.45}$$

where C_b is an empirical constant (C_b=0.5), x is the instantaneous displacement of the droplet from its equilibrium position and D_p is the droplet diameter. The Taylor analogy between a distorting droplet and a damped spring-mass system gives a second-order ordinary differential equation, as expressed by Equation 2.46.

$$\frac{\rho_l D_p^2 y}{4} = \frac{C_k \sigma}{D_p} \left(\frac{We}{We_{crit}} - 2y \right) - C_d \mu_l \dot{y} \tag{2.46}$$

where σ and μ_l are the surface tension and viscosity of the droplet, respectively. C_d, C_k and We_{crit} are empirical constants with the following values:

$$C_d = 5;\;\; C_k = 8;\;\; We_{crit} = 12;$$

Droplet Breakup

The TAB breakup model relies on the TAB distortion model to calculate the normalized droplet distortion (See Equation 2.45). When the droplet oscillations reach a critical value (y=1), the droplet is assumed to be critically distorted and a breakup event is then triggered. The Sauter mean diameter D_{32} of the post-breakup droplets is related to the diameter D_p of the parent droplet through an energy balance, giving:

$$\frac{D_p}{D_{32}} = 1 + \frac{KC_b^2C_k}{5} + \frac{3C_b^2m_p}{4\sigma\pi}\left(\frac{K}{5} - \frac{C_v^2}{6}\right)\dot{y}^2 \tag{2.47}$$

where C_k and C_b are inherited from the TAB distortion model, K is the ratio of the total energy in distortion and oscillation to the energy in the fundamental mode. In STAR-CCM+, the breakup replaces the parent droplets with child droplets whose diameter is chosen from a Rosin-Rammler distribution with the Sauter mean diameter given by Equation 2.48. Post-breakup parcels are also given a velocity normal to the original velocity of the parent parcel (See Equation 2.48). This is proportional to their rate of distortion at the instant of breakup $\dot{y}_b$.

$$v_\perp = \frac{1}{2}C_vC_bD_p\dot{y}_b^2 \tag{2.48}$$

where C_v is the normal velocity coefficient (C_v=1).

Due to the high velocity gradients in the outlet of the IC-1.1, the primary atomization was assumed to occur before the droplet injectors, which were placed 2 mm away from the catheter tip as an estimation of the distance between the the APS nozzle and the laser beams that measures the droplets properties. It must be noted that the APS has the potential to measure the properties of droplets between 0.5 μm - 20 μm, associated with the secondary breakup, and not the fragmentation and formation of ligaments related to the primary breakup.

2.2.3.7 Interaction between continuous phase and dispersed phase

The interactions between the continuous phase and the dispersed phase can be modeled as *one-way coupling* or *two-way coupling*. The coupling refers to the way that momentum, heat and mass are exchanged between the phases.

With *one-way coupling*, the continuous phase influences the dispersed phase, but not in the reverse direction. With *two-way coupling*, the effects of the dispersed phase on the continuous phase such as displacement, interphase momentum, mass, and heat transfer are taken into account (See Figure 2.17). The displacement of the continuous phase by the dispersed phase is accounted for through the volume fraction. The volume fraction of a Lagrangian phase is the fraction of the local cell volume which that phase occupies.

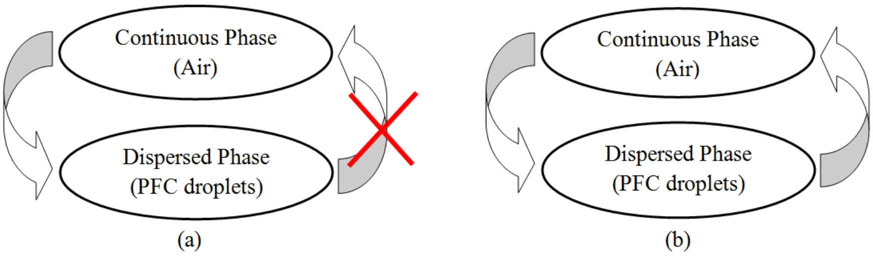

Figure 2.17: (a) One-way coupling and (b) Two-way coupling interaction.

The volume fraction ϕ_c of a Lagrangian phase is seen as a void by the continuous phase. The volume available for the continuous phase decreases by this fraction and, in practice, ϕ_c is under-relaxed to promote stability:

$$\phi_c = \alpha \left(\sum \phi \right) + (1 - \alpha) \cdot \phi_{c,old} \tag{2.49}$$

where α is an under-relaxation factor of the two-way coupling solver and $\sum \phi$ is the sum of the volume fractions of the relevant Lagrangian phases. The value of ϕ_c which is contributed to the continuous phase void fraction is limited to min(ϕ_c, $\phi_{c,max}$) again to promote stability.

The Lagrangian dispersed phase equations, when integrated over a cell, yield the changes in the momentum, mass and energy of each droplet between its entry and exit. The sum of these changes for all droplets crossing the volume provides the net momentum, mass and energy that is exchanged with the continuous phase. These net exchanges enter the continuous phase equations as source terms.

2.2.4 Numerical Procedure

The CFD code used in the present thesis, STAR-CCM+, provides multiple flow solvers that address different categories of fluid flow. These solvers include the *viscous flow solver*, the *segregated flow solver* and the *coupled flow solver*. Choosing the correct solver is one of the first steps in a flow analysis. According to the guidelines of the CFD code, for an external flow of a Newtonian fluid, the **Coupled Flow model** is the solver suggested to provide more robust and accurate solutions in compressible flows with Mach numbers in the range expected in this application ($0.7 < \text{Ma} < 1.2$). The scheme of Figure 2.18 represents the procedure followed for the resolution with the coupled flow model.

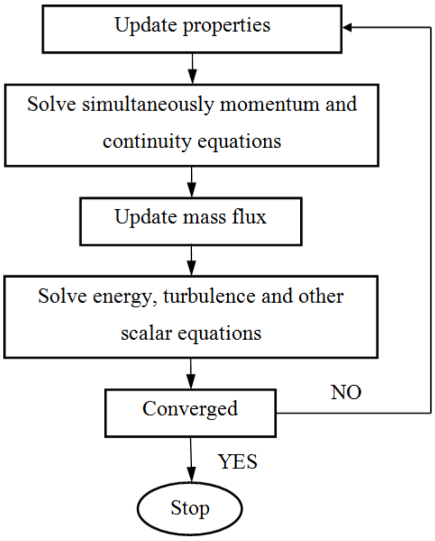
Update properties
Solve simultaneously momentum and continuity equations
Update mass flux
Solve energy, turbulence and other scalar equations
Converged
NO
YES
Stop

Figure 2.18: Numerical procedure followed for the resolution with the Coupled Flow model.

With the coupled solver, the conservation equations for continuity, momentum and energy are solved in a coupled manner, that is, they are solved simultaneously as a vector of equations. The velocity field is obtained from the momentum equations, the pressure is calculated from the continuity equation and the density is evaluated from the equation of state.

Figure 2.19 summarizes the steps carried out to run the numerical simulations. Initially, the continuity and Navier-Stokes equations were solved for the continuous phase (airflow) in steady state. Once the steady state air solution was converged, the numerical results were saved and used as the initial condition to run the unsteady state simulation with both phases, the continuous phase (airflow) and the discrete phase (PFC droplets).

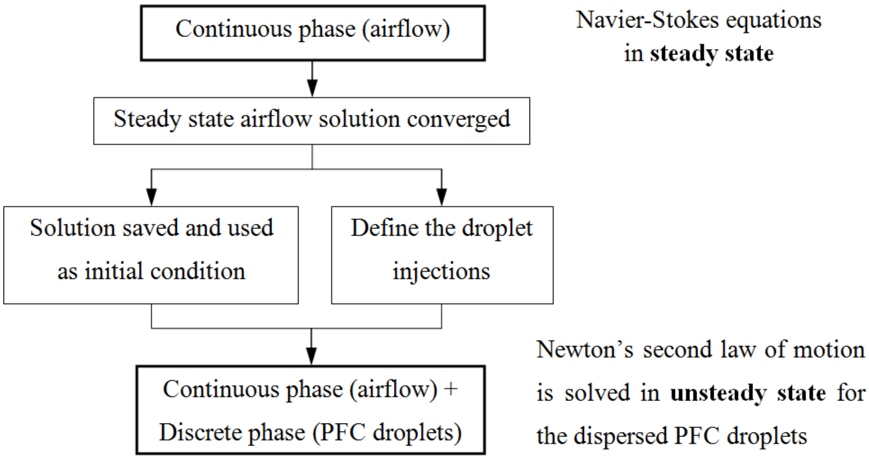
Continuous phase (airflow)
Navier-Stokes equations in **steady state**
Steady state airflow solution converged
Solution saved and used as initial condition
Define the droplet injections
Continuous phase (airflow) + Discrete phase (PFC droplets)
Newton's second law of motion is solved in **unsteady state** for the dispersed PFC droplets

Figure 2.19: Steps carried out to run the numerical simulations.

This system of equations is solved by either the explicit or the implicit time-integration scheme. In the present thesis the **implicit scheme with a first order temporal discretization** has been chosen with a Courant number (CFL) value of 50 in order to facilitate the convergence of the solution. The CFL condition, defined by Equation 2.50, expresses that the distance that any information travels during the time-step length must be lower than the distance between mesh elements, i.e., the information from a given mesh element must propagate only to its immediate neighbours.

$$CFL = \frac{u\Delta t}{\Delta x} \tag{2.50}$$

where u is the velocity magnitude, Δt is the time-step and Δx is the length interval.

A time-step in an unsteady simulation advances the solution from time t to time $t + \Delta t$. A single iteration of the unsteady solver for the LMP model involves:

1. Recovering the Lagrangian Multiphase solution at time t.
2. Advancing the Lagrangian Multiphase solution to time $t + \Delta t$ by time-marching. A local time-step is used for each parcel. The time-step is adjusted dynamically according to the time-step controls in force.

These two steps are executed in each iteration of the unsteady solver, before the flow solver. Additionally, with the two-way coupling model active, the source terms that the Lagrangian phase models compute are stored for subsequent application in their respective transport equations. The *Hybrid Gauss-Least Squares Method* has been used for the evaluation of the variable gradients and the Cell Cluster property of the *Source Smoothing method* has been activated to control the size to the large-scale cells. This option uses a cell clustering technique to group together cells to form a coarser mesh on which to pass data. The size of the cluster is then independent of the underlying mesh size, ensuring that droplets are always smaller than the mesh used for coupling with the flow.

For **parallel processing**, the traditional approach to decompose the volume mesh is to provide each processor with approximately the same number of cells. For cases where the same Eulerian flow equations are solved in each cell, this approach generally gives good performance. However, for cases containing particles (droplets in this study), this traditional form of decomposition can lead to imbalanced CPU loads across the parallel cores. If one or two partitions contain most of the droplets, they will require significantly more computation time than partitions with few droplets. The traditional decomposition method does not account for this difference. STAR-CCM+ provides an alternative approach which takes into account the presence of droplets in the domain decomposition. The **Lagrangian load-balancing solver** collects information about the computational load that is required to solve droplet physics in each Eulerian cell and passes it to the partitioning solver, which coordinates the final load balancing (see scheme of Figure 2.20). This approach optimizes the domain decomposition in response to changing droplet distributions and the computational load across all CPU cores remains balanced as droplets migrate throughout the domain.

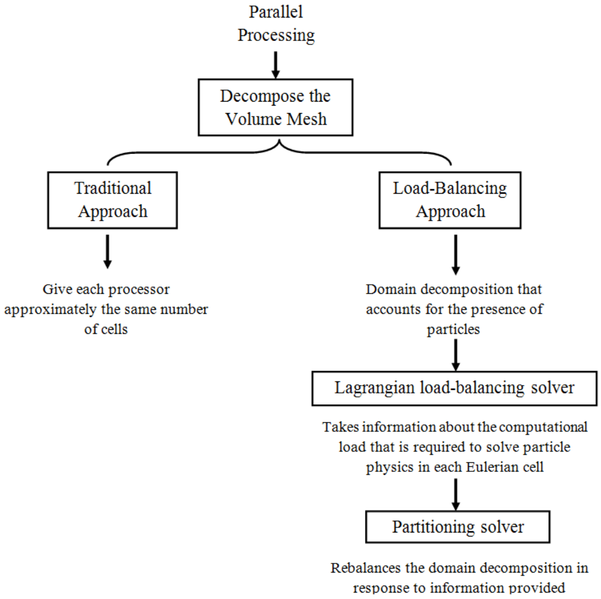
Parallel Processing
Decompose the Volume Mesh
Traditional Approach
Load-Balancing Approach
Give each processor approximately the same number of cells
Domain decomposition that accounts for the presence of particles
Lagrangian load-balancing solver
Takes information about the computational load that is required to solve particle physics in each Eulerian cell
Partitioning solver
Rebalances the domain decomposition in response to information provided

Figure 2.20: Scheme of domain decomposition approaches.

2.2.5 Temporal and Discrete Phase Discretization

The determination of the temporal discretization for a simulation is based on the adequate resolution of an unsteady physical phenomenon. In this case, due to the unsteady characteristics of the aerosols produced with the IC-1.1, it was necessary to define the temporal discretization in the numerical model, which consists of solving the unknowns of the flow in a specific instant. To that end, it is necessary to indicate how often is desired to obtain these unknowns by means of the **time-step (Δt)**. The larger the Δt value, the larger the temporal discretization error, since the solver is not able to capture the whole unsteady physics of the problem. However, the computational cost increases exponentially as the Δt value is decreased. Therefore, in order to obtain a time-step independent solution, different Δt values were studied and finally a constant Δt of $1{\cdot}10^{-4}$ s has been chosen taking into consideration the relation between the accuracy of the results and the computational cost. Additionally, 300 inner iterations per time-step has been defined to achieve the convergence of the numerical solution.

From the computational standpoint, solving the trajectories of hundreds of thousands of physical droplets that form part of the aerosol is extremely expensive. For this reason, the CFD code uses the concept of **parcel** to reduce the computational cost. Each parcel represents a group of droplets that have the same physical properties (temperature, velocity, mass fraction, etc). Therefore, the total population of droplets is represented by a small number of computational parcels instead. Similar to the number of cells, the number of parcels is not arbitrary; it must be large enough to represent accurately the full population of the aerosol droplets. In that sense, a **parcel dependency study** has been carried out to control the discretization accuracy of the droplet population. This is visible from a monitor plot of the droplet mass flow at the outlet of the computational domain. The results for the PFD compound at 4 bar were monitored with three different number of parcels injected per time-step (100 parcels/Δt, 500 parcels/Δt and 1000 parcels/Δt), as illustrated in Figure 2.21. An increase in the number of parcels injected improves the accuracy of the solution. It was necessary to take a balance between the computational time, the convergence and the accuracy of the solution to choose the optimal number of parcels. A considerable difference was observed between the case with 100 and 500 parcels/Δt. After analyzing the results, and due to the high difference in computational time between the cases of 500 and 1000 parcels/Δt it was concluded that the resolution with 500 parcels/Δt

provides the best relation between accuracy and computational cost to discretize the droplet population of the aerosol.

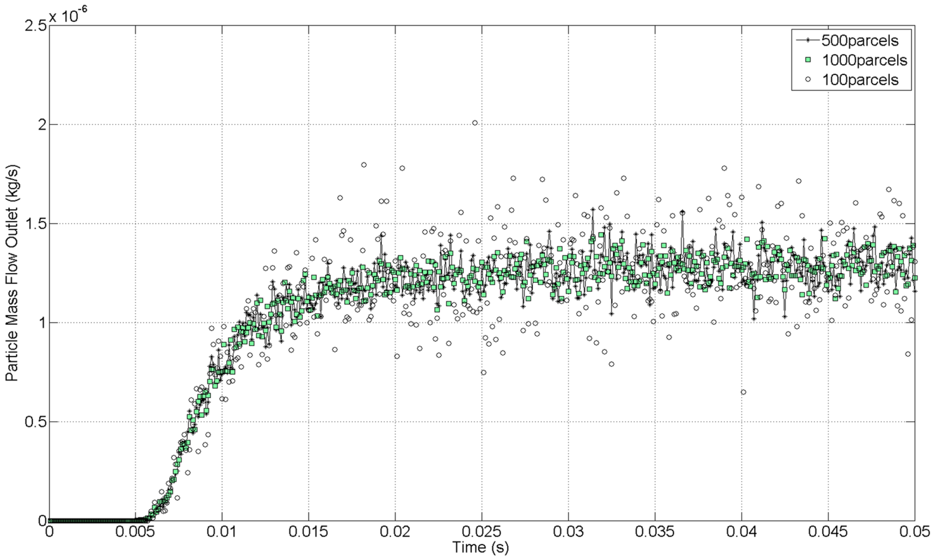

Figure 2.21: Discrete phase dependency study.

2.2.6 Continuous and Discrete Phase Simulation Results

Firstly, Navier-Stokes and continuity equations were solved for the continuous phase in steady state. The results of the converged solution were saved and subsequently used as the initial condition for the transient simulation of both phases, i.e., the airflow and the parcels representing the discrete phase. The solution of the continuous phase is illustrated in Figures 2.22 - 2.23 with the airflow velocity fields. As expected, the largest axial velocity values were observed close to the catheter tip with 391 m/s and 455 m/s for pressures of 4 and 5 bar, respectively. The velocity in the injectors' position was 247 m/s and 293 m/s for 4 and 5 bar of driving pressure, respectively. These values were checked in order to define the initial velocity condition of the PFC droplets in the injector points. The high air velocity values obtained confirms the importance of considering the airflow as compressible flow in this application.

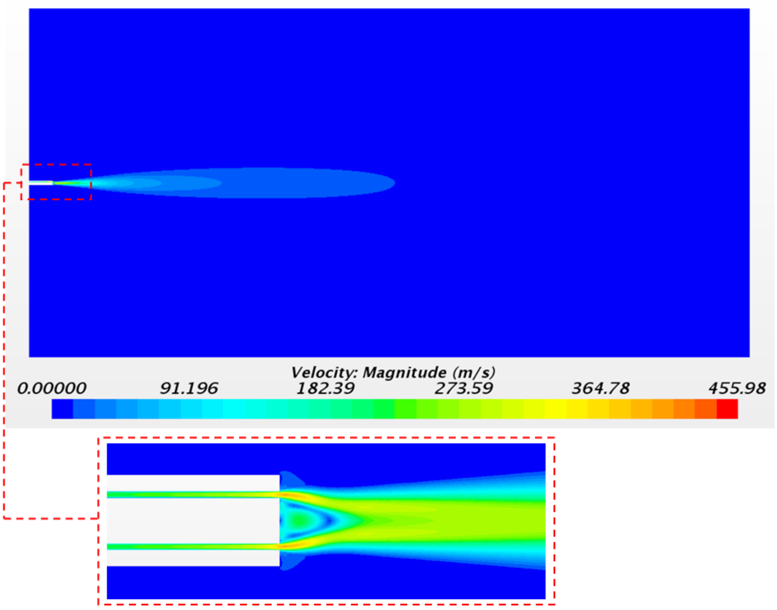

Figure 2.22: Continuous-phase velocity magnitude with a pressure of P=4bar.

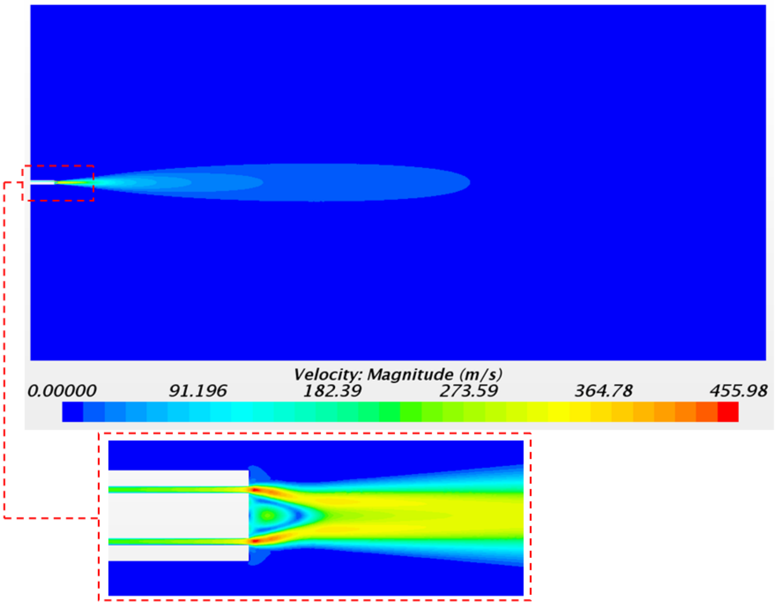

Figure 2.23: Continuous-phase velocity magnitude with a pressure of P=5bar.

The solution of the discrete phase is illustrated in Figure 2.24 with the formation of the aerosol cone with FC75 at 4 bar. The solution was taken 0.06 s after the release of droplets from the injectors. The transitory condition of the aerosol flow changes the distribution of droplets with time. For that reason, it was necessary to track a representative sample of 0.01 s in order to study the numerical results.

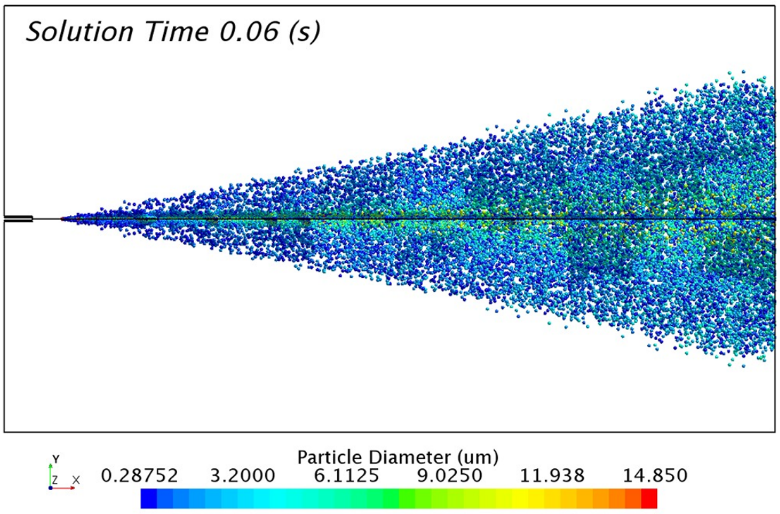

Figure 2.24: Particle size distribution of the FC75 discrete droplets with a driving pressure of 4 bar.

2.2.7 Convergence Criteria

When running a numerical simulation it is important to establish a convergence criterion to define when the calculation has reached the final solution. The convergence of a numerical process can be stated as the solution of the system of algebraic equations approaching the true solution of the partial differential equations having the same initial and boundary conditions as the refined grid system [117]. This system of algebraic equations is usually solved iteratively by the CFD codes. During the numerical procedure, the imbalances (errors) of the discretized equations are monitored and they are referred as the **residuals** of the system of algebraic equations. For a satisfactory convergence, the residuals should diminish as the numerical process progresses. In the current thesis, the solution was considered converged with a three-order-of-magnitude drop in the numerical residuals [118]. Additionally to the residuals it is advisable to monitor a quantity of interest to ensure the stability of the solution. In this case, the evolution of the axial velocity in a point at the outlet of the computational domain has been monitored, see Figure 2.25. The criterion used to consider that the axial air velocity at the outlet is stable has been to verify that the velocity varies less than 0.1% every 1000 iterations. Figure 2.26 shows the evolution of the axial velocity throughout the numerical process with a variation of 0.0087% in the last 1000 iterations.

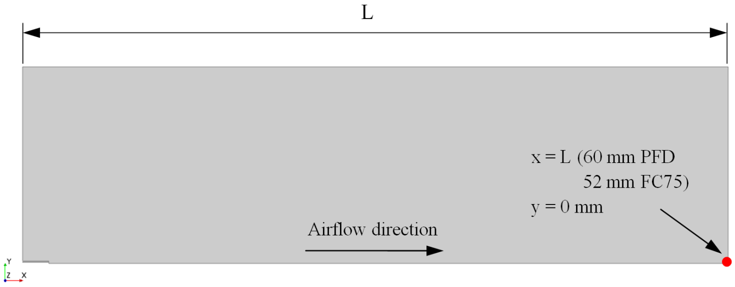

Figure 2.25: Coordinates of the point chosen to monitor the evolution of the axial air velocity.

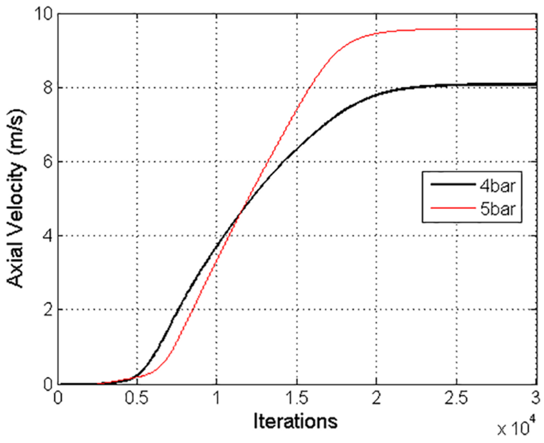

Figure 2.26: Axial air velocity values with pressures of 4 bar and 5 bar, considered to confirm the convergence of the numerical solution.

2.2.8 Validation of the Numerical Model

The axial velocity results with a pressure of 4 bar were monitored at several distances from the catheter tip and validated with the experimental results obtained by Goikoetxea et al. [98]. The turbulence model chosen along with the mesh refinement generated close to the catheter tip led to an accurate prediction of the airflow velocity values, as shown in Figure 2.27 [119].

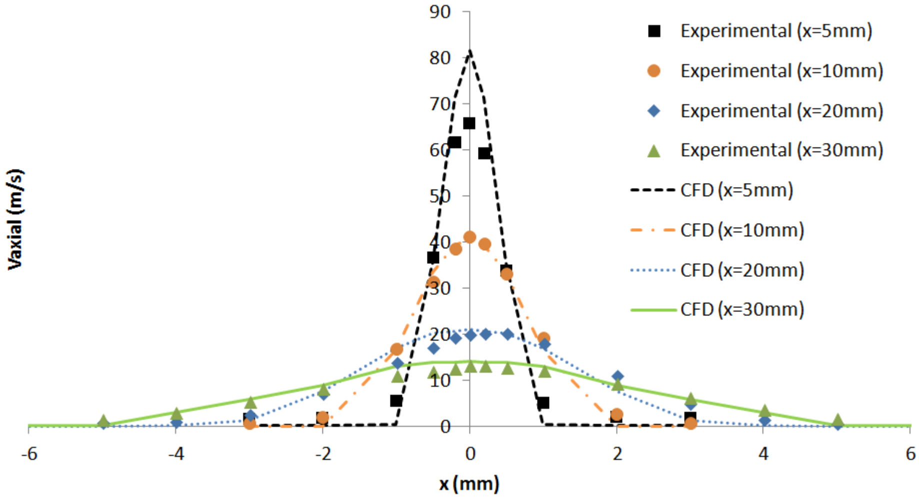

Figure 2.27: Experimental and numerical axial air velocity profiles at different distances from the IC-1.1 tip.

The results of the cumulative mass distribution as a function of the droplet size (Y_{dg}) are presented in Figures 2.28 and 2.29 for PFD and FC75 compounds, respectively, and were compared with the experimental data obtained by means of the APS. Some differences were found between the numerical and the experimental results. The collision and coalescence of the droplets may be the cause of those deviations. In the numerical model, which considered the breakup of the droplets with the TAB breakup model but not the coalescence, a higher cumulative mass fraction was obtained for droplets above 3 μm for the PFD compound at both pressures and for each distance studied. For the FC75 compound, with a pressure of 4 bar, the cumulative mass fraction was higher for droplets below 5 μm and considerable lower for droplets above 10 μm. With a pressure of 5 bar there was a different pattern in the experimental results and the cumulative mass fraction for droplets above 10 μm was considerable higher.

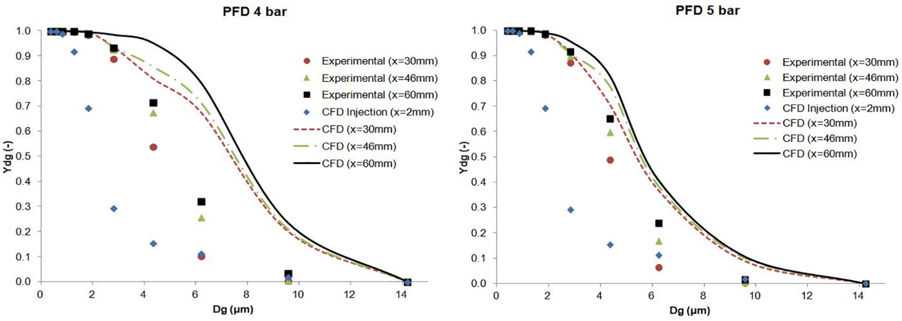

Figure 2.28: Experimental and numerical cumulative mass distribution based on droplet size for the PFD compound.

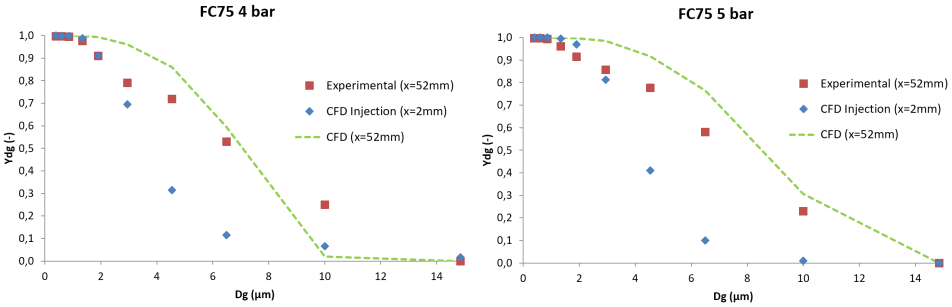

Figure 2.29: Experimental and numerical cumulative mass distribution based on droplet size for the FC75 compound.

2.2.9 Conclusions

This chapter has studied the generation of a PFC aerosol by means of an inhalation catheter, the IC-1.1, and its main parameters measured experimentally with an APS and numerically with CFD techniques [120]. Different cases were studied for PFD and FC75 varying the driving pressure of the compressed air between 4 and 5 bar. The results were measured at the optimal distances between the

APS nozzle and the catheter tip and at some additional distances in the case of PFD. The GSD values varied from 1.61 to 2.04, leading to the formation of heterodisperse aerosols. The aerodynamic diameter (D_a) provided values that were within the recommended range values (1-5 μm) and, although the MMAD results were between 5-10 μm, we must take into account that the goal of this study is the generation of an aerosol beyond the nasopharyngeal region, avoiding in that way the deposition of these bigger droplets.

Subsequently, the numerical model was introduced in order to simulate the generation of the PFD and FC75 aerosols with CFD tools. These numerical simulations were validated with the axial velocity results obtained experimentally with a hot-wire anemometer [98], confirming their accuracy at different downstream positions. The differences in the cumulative mass distribution of the aerosol droplets between the numerical and experimental procedure suggest that the collision and coalescence of the PFC droplets may play an important role during the formation of the aerosol. Similar behavior could be seen for PFD at both driving pressures studied, whereas for FC75, the cumulative mass fraction for droplets above 10 μm was considerable higher with a driving pressure of 5 bar. The numerical study presented in this thesis could be a helpful tool to carry out parametric studies with new prototype nebulizers to treat the RDS in preterm babies.

CHAPTER 3

NEBULIZER PROTOTYPE DESIGN

3.1 Additive Manufacturing Techniques in Medical Applications

Additive manufacturing consists in the manufacturing process of a three-dimensional object created by superimposing successive layers of material. This development allows the creation of complex 3D prototypes, curved surfaces, cantilevers and interior ducts that could hardly be manufactured using conventional technology. Lee et al. [121] summarized the fundamental aspects of additive manufacturing processes in terms of resolution, speed and specific energy as well as the introduction of new novel advanced materials with specific properties. Ligon et al. [122] reviewed the development of polymers and advanced polymer systems specifically for additive manufacturing.

The manufacture of 3D models requires a pre-printing process which consists in the configuration and programming of the model to be printed in the specific software of each machine. This process is summarized with the following steps: (See Figure 3.1).

1. Design the 3D model by means of CAD software.
2. Export the 3D model to printable .STL format (triangular mesh).
3. Import the 3D model into the machine-specific printing software.
    (a) Model slicing (Layers generation).
    (b) Model orientation (Avoid or reduce the printing of supports).
    (c) Supports generation.
    (d) Material configuration (Temperature of manufacturing, print speed...).
4. Launch the processed model to 3D printer to start the manufacturing.

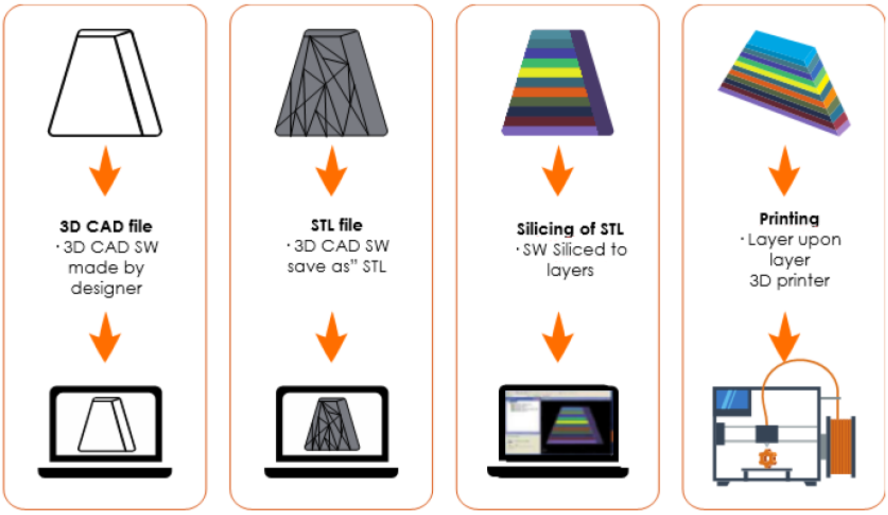
3D CAD file
· 3D CAD SW
made by
designer
STL file
· 3D CAD SW
save as" STL
Silicing of STL
· SW Siliced to
layers
Printing
· Layer upon
layer
3D printer

Figure 3.1: Steps involved in the configuration and programming of the pre-printing process. Source: provided by Optimus 3D company.

Over the last years, the use of additive manufacturing techniques has experienced an upsurge for the **development of new biomedical devices** due to its flexibility and versatility to reproduce complex geometries and personalized products. Vukicevic et al. [123] analyzed the application of 3D printing techniques to create models of congenital heart defects for anatomic teaching or medical training. Regarding the study of respiratory issues, Cheng et al. [124] manufactured a customized nasal mask cushion for a CPAP device to fit a particular patient's face. Two rapid prototyping techniques were compared and it was found that the customized cushion provided a better fit between the face and the cushion and less leakage compared with two other similar commercial cushions. Vermeulen et al. [125] presented a case study where a patient-specific airway geometry was used to manufacture a 3D model and to perform a flow analysis by a particle image velocimetry system. Recently, Copploe et al. [126] have developed a neonate eight-generation airway model by means of additive manufacturing techniques to study the distribution of instilled surfactant, see Figure 3.2. This work showed the potential of 3D printed models to carry out quantitative studies of surfactant delivery into the respiratory system and to identify the best conditions that lead to an optimal distribution.

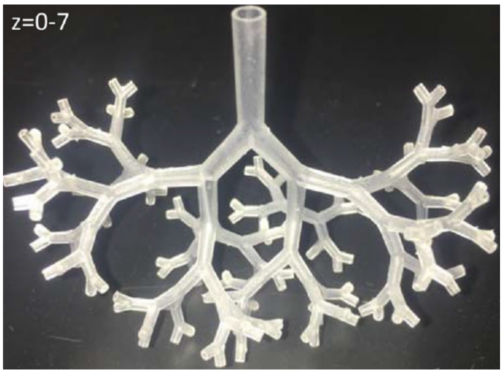

Figure 3.2: Eight-generation neonate airway model created with additive manufacturing techniques by Copploe et al.[126].

3.1.1 Additive Manufacturing Technologies

Additive manufacturing covers various technologies with the same principle of superposition/addition of material but with technical differences for each case and application. The following list summarizes the most common technologies; the rest will comprise the same manufacturing base having different specific characteristics (manufacturing speeds, materials, software, hardware ...).

- **Fused Deposition Modeling (FDM):** The filamented polymer melts and the head extrudes the material by depositing it layer by layer on the printing plate. The superposition of the layers will create the 3D model. One of the most common materials used with this technology is the acrylonitrile butadiene styrene (ABS), a thermoplastic polymer mainly known for its good resistance to low temperatures and its light weight. The layer resolution, depending of the machine, oscillates between 0.127-0.330 mm.

- **Selective Laser Melting (SLM):** It is a technology specially developed for 3D printing of metal alloys. It generates additive parts by melting the metal dust particles layer by layer in an integral fusion process creating a homogeneous block with high resistance. The materials used are usually nickel-based, titanium, stainless steel and aluminium alloys with a layer resolution approximately of 0.05 mm.

- **Selective Laser Sintering (SLS):** It was developed and patented in the mid-1980s by Deckard and Beaman [127]. This technique uses a laser as the power source to sinter powdered plastic material into a solid structure based on a 3D model. It uses a comparable concept to SLM, but sintering the material instead of melting. The most common materials used with this technology includes polymers such as polyamides and polystyrenes. The layer resolution oscillates between 0.060-0.150 mm, depending on the 3D printer used.

- **Multi Jet Fusion (MJF):** With the Multi Jet Fusion technology, developed by the commercial brand HP, a thin layer of powder is spread over the build platform where it is heated to a near-sintering temperature. MJF provides faster cooling times and greater recyclability than SLS with recovered powder values up to 80-85%. The main material used is PA 12 (nylon) with an approximate layer resolution of 0.08 mm.

- **Stereolithography (SLA):** This additive manufacturing process uses a liquid resin that becomes solid when exposed to the light from an ultraviolet laser. The liquid resin is solidified through a process called photopolymerization, where the monomer carbon chains that compose the liquid resin are activated by the ultraviolet laser light, creating strong unbreakable bonds between each other. It provides good resolutions at 0.05-0.127 mm, depending on the 3D printer used.

- **PolyJet:** This technology is an improvement over the SLA technique. Both of them use ultraviolet energy to cure plastics but their differing build styles separate them in terms of accuracy and applications. This technology is based on the photopolymerization of resin, which consists in the projection of micro droplets over a platform along with an emission of ultraviolet light that solidifies the material with a curing procedure. This process is repeated creating the desired geometry, layer by layer, until obtaining the model part, which will not need any subsequent stage, and getting the manufacturing of great precision parts with complex geometries. PolyJet uses multiple print heads to deposit liquid plastic onto a clean build platform layer by layer. The speed and fine resolution of PolyJet make this technology ideal for the manufacturing of highly detailed prototypes, with a layer resolution up to 16 μm.

3.2 Application of 3D Printing Techniques to Manufacture a Nebulizer Prototype

Further research is needed to develop a suitable device for neonates in order to optimize the drug delivery in a non-invasive and effective way. To that end, additive manufacturing techniques have been chosen for the development of a new nebulizer prototipe due to the versatility and flexibility of this technology. However, the small dimensions required to obtain an accurate nebulization made this a challenging manufacturing process. Two different prototypes have been developed, allowing the aerosol generation and offering potential to drug delivery without the need of intubation. Both protoypes designed are classified within twin-fluid nebulizers with external mixing, i.e., the gas interacts with the liquid outside of the nebulizer. Twin-fluid nebulizers typically produce a full cylindrical spray cone with relatively small droplets at high liquid mass flow rates [128]. **Prototype 1** consists of six small outer lumens, where compressed air is delivered, and a central lumen where the liquid flows. On the other hand, in the **Prototype 2**, the outer lumens have been replaced with two half-circular rings. The central lumen has the same dimensions in both prototypes and the area of the two half-circular ring in Prototype 2 is equal to the area of the six outer lumens of Prototype 1. Figure 3.3 shows the distal geometry of each prototype and their main dimensions. Drawings with all the geometry details of both prototypes are added in Appendix A.

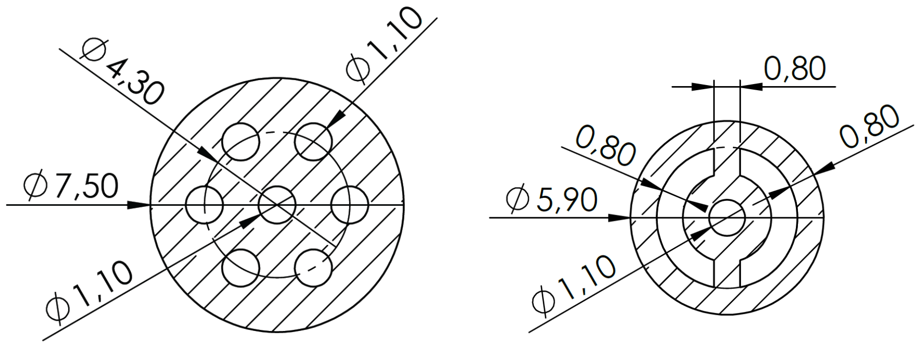

(a)

(b)

Figure 3.3: (a) Distal geometry dimensions of Prototype 1 and (b) Prototype 2. (Dimensions are given in mm).

3.2.1 Prototypes Manufacturing with PolyJet Technology

The manufacturing of all the prototypes presented in the current thesis have been developed by the company OPTIMUS 3D, located in the Álava Technology Park. Initially, it was considered to use the Polyjet technology by means of the *Stratasys*

Objet30 Pro 3D printer, see Figure 3.4a. The resolution of this machine allowed to print the prototypes proposed with all the necessary details.

(a)

	Objet30 Pro
Maximum Build Size (XYZ)	294 x 192 x 148.6 mm
Resolution	600 x 600 x 900 DPI
Layer Thickness	16 μm
Model Material	VeroClear Transparent
Support Material	SUP705 (WaterJet removable)

(b)

Figure 3.4: (a) Stratasys Objet30 Pro 3D printer and (b) its specifications.

Initially, preliminary printing tests were performed with a section model of 82 mm in length, instead of the original total length dimension proposed of 131.9 mm, in order to check the feasibility to print and clean a model of this length and such small dimensions. This manufacturing system deposits material in the build tray and, at the same time, it is solidified by means of ultraviolet light allowing to create the model layer by layer. Support material is printed for the creation of models with ring holes or that are cantilevered on the printing surface, which is finally removed by means of pressurized water or by soaking the models in a solution of caustic soda (sodium hydroxide). To facilitate the removal of this support material and minimize the problems related with that, tolerance cylinders were designed as shown in Figure 3.5. When the printing has ended, the model was introduced in a solution of caustic soda to soften the support material and then the cylinders were extracted, allowing to remove most of the support material. Finally, pressurized water was used to remove the remaining support material.

The extraction of cylinder 1 (2 mm) could be carried out succesfully, as observed in Figure 3.6b. However, the cylinders created for the outer and central lumen (0.75 mm) were not possible to be extracted and on several occasions the cylinders broke during the process. It was also observed that the intersection between the two inlets was the more difficult part of the model to carry out the removal of the support material.

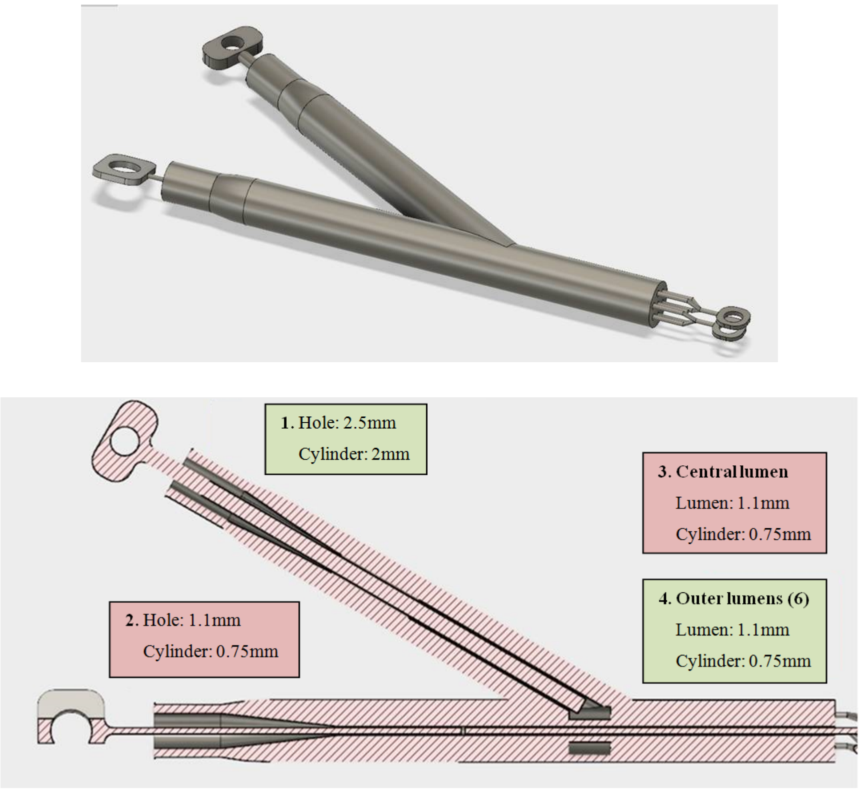
1. Hole: 2.5mm
Cylinder: 2mm
3. Central lumen
Lumen: 1.1mm
Cylinder: 0.75mm
4. Outer lumens (6)
Lumen: 1.1mm
Cylinder: 0.75mm
2. Hole: 1.1mm
Cylinder: 0.75mm

Figure 3.5: Definition of the tolerance cylinders to facilitate the extraction of the support material.

In conclusion, the *Objet30 Pro* 3D printer allowed to print the models and the detail of the holes correctly but **it was not able to remove the support material** by the use of pressurized water without causing the breakage of the model. These initial tests showed that it was necessary to increase the diameter proposed for the central and outer lumens in order to create stiff enough cylinders. More preliminary tests were carried out, reaching to the conclusion that it was necessary a minimum lumen diameter of 2.5 mm to be able to remove cylinders of 2 mm to clean correctly a model of the length proposed in Prototype 1 and Prototype 2 (131.9 mm).

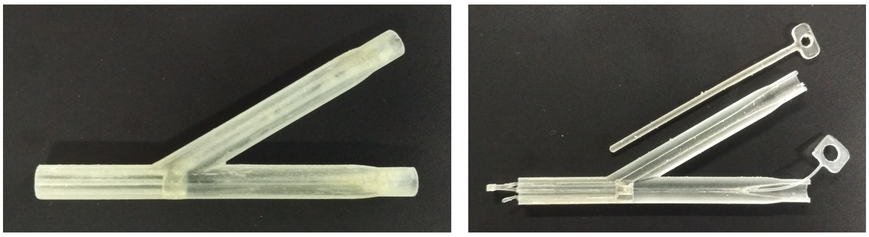

(a) Section of Prototype 1 printed (82 mm in length).

(b) Extraction of tolerance cylinders to remove the support material.

Figure 3.6: Preliminary tests carried out with the Objet30 Pro 3D printer.

These dimensions are far away of our requirements and, therefore, other different additive manufacturing processes were taken into account to print the prototypes proposed. Finally, the *3D Systems-ProJet MJP 5600* 3D printer, illustrated in Figure 3.7, was chosen for the development of the prototypes discussed in the present thesis. This 3D printer, just as the *Objet30 Pro* used previously, is based in the PolyJet technology and it has a height layer precision of 16 μm, allowing the manufacturing of the holes required in the prototypes presented in this thesis. It is a large format multi-material 3D printer that offers print speeds up to twice as fast as similar PolyJet printers. In addition, thanks to the large volume of printing, it has the advantage to reduce model costs up to 40% compared to 3D printers for multiple competing materials.

The difference between both 3D printers consists in the application of the support material. The *3D Systems-ProJet MJP 5600*, in comparison with the *Objet30 Pro*, offers the alternative of **generating a specific wax support**, which is removed with heat after printing. This 3D printer uses flexible and rigid photopolymers of the *VisiJet* family commercial brand. Specifically, the *VisiJet CR-CL* (Clear Polycarbonate-like material) has been used in all the prototypes printed and discussed in this thesis. Table 3.1 shows the specifications of this material.

(a)

	MJP 5600
Maximum Build Size (XYZ)	518 x 381 x 300 mm
Resolution	600 x 600 x 1600 DPI
Layer Thickness	16 μm
Model Material	VisiJet CR-CL
Support Material	VisiJet S500 non-toxic wax

(b)

Figure 3.7: (a) Stratasys Objet30 Pro 3D printer and (b) its specifications.

Properties	**VisiJet CR-CL**
Composition	Ultraviolet curable plastic
Description	Rigid polycarbonate-like
Color	Translucent clear
Solid Density	1.18 g/cm^3
Tensile Strength	37-47 MPa
Tensile Modulus	1000-1600 MPa
Elongation at Break	7-16 %
Flexural Strength	61-72 MPa
Flexural Modulus	1400-2000 MPa
Impact Strength (Notched Izod test)	16-19 J/m
Water Absorption	0.5 %
Shore A Hardness	N/A
Shore D Hardness	76-80
Heat Distortion Temperature	46 °C

Table 3.1: Material properties.

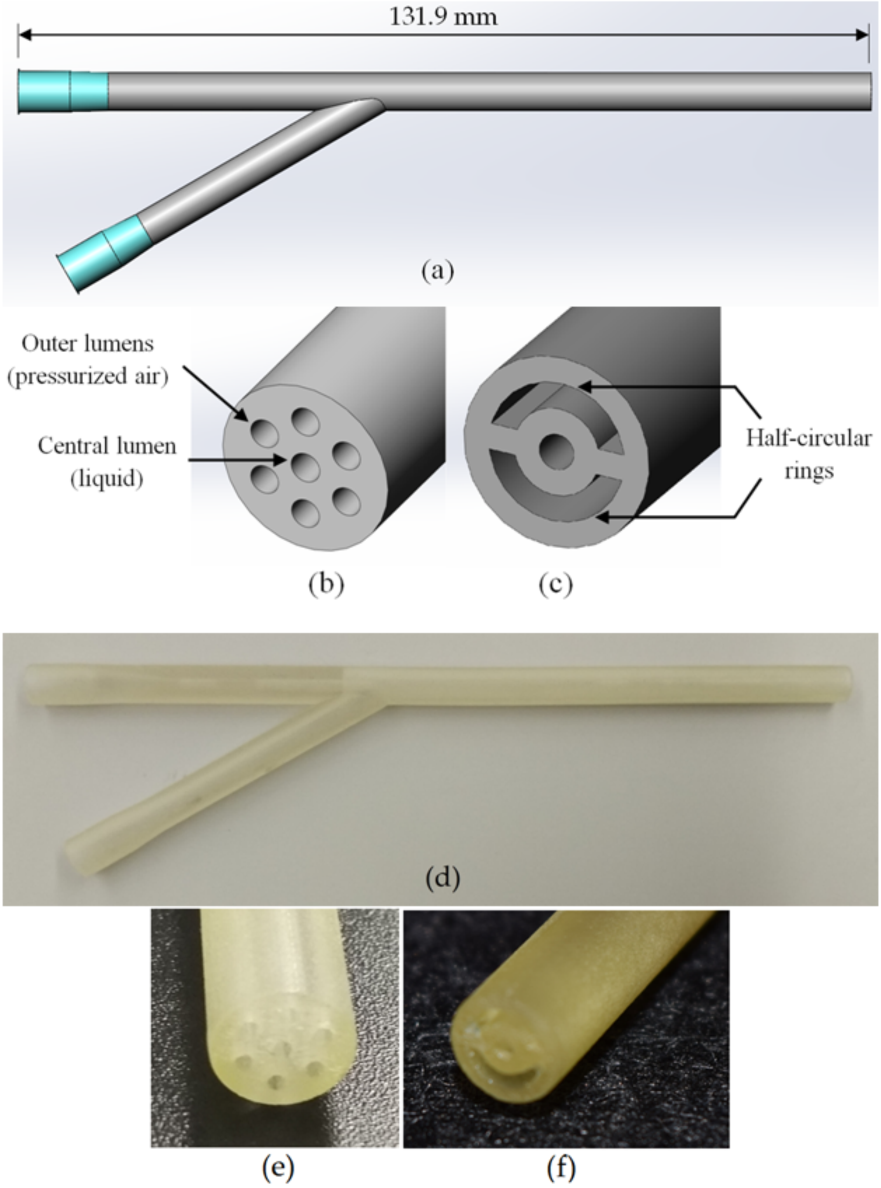
131.9 mm
(a)
Outer lumens
(pressurized air)
Central lumen
(liquid)
Half-circular
rings
(b)
(c)
(d)
(e)
(f)

Figure 3.8: (a) General visualization of the nebulizer prototype design proposed, distal section of (b) Prototype 1, (c) Prototype 2. Manufacturing result of Prototype 1 (d), distal section detail of the manufactured (e) Prototype 1 and (f) Prototype 2.

3.3 Experimental Setup with the Prototypes

Both prototypes were tested with the same compounds that were used in the experimental study carried out with the IC.1.1 described in the previous chapter; distilled water (H_2Od), PFD and FC75. Their properties are shown in Table 3.2. Figure 3.9 illustrates the experimental setup used to measure the droplet size distribution of the aerosols generated with Prototype 1 and Prototype 2. The mass median aerodynamic diameter (MMAD), the aerodynamic diameter (D_a) and the geometric standard deviation (GSD) were analyzed by means of the APS.

Parameter	H_2Od	PFD	FC75
Density (ρ) [g/ml]	0.99	1.95	1.78
Kinematic viscosity (υ) [cSt]	1.003	2.70	0.81
Surface tension (σ) [dyn/cm]	73	15	15

Table 3.2: Properties of H_2Od and PFCs.

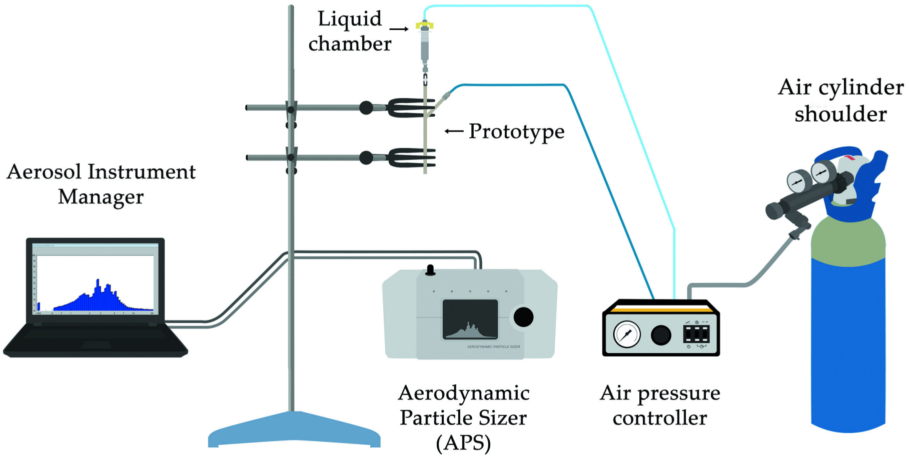
Liquid chamber
Prototype
Air cylinder shoulder
Aerosol Instrument Manager
Aerodynamic Particle Sizer (APS)
Air pressure controller

Figure 3.9: Experimental setup used for the particle size characterization with the nebulizer prototypes.

The same **air pressure controller** described in the experimental study with the IC-1.1 (LABneb, Trudell Medical International), with an operating range of 0-7 bar, has been used. It provides compressed air to both the small piston placed within the liquid chamber and to the side connection of the nebulizer prototypes, where the air is delivered to the outer lumens and to the two half-circular rings respectively. The air was supplied by an **air cylinder shoulder** (Alphagaz 1 Air) with purity higher than 99,999% assuring that the air delivered is empty of impurities that could block the nebulizer prototypes lumens or the APS nozzle. A **pressure reducer** was included to regulate the pressure from the 200 bar supplied by the air cylinder shoulder to an interval of 0-10 bar, necessary to control the air pressure provided to the air pressure controller, see Figure 3.10.

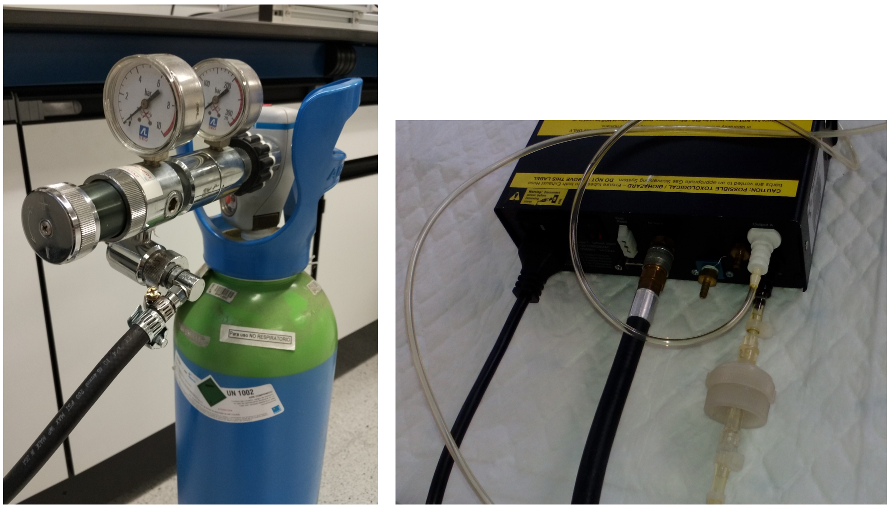

(a) (b)

Figure 3.10: (a) Air cylinder shoulder with the pressure reducer included and (b) detail of the connections to the air pressure controller.

The distance between the inlet nozzle of the APS and the distal section of the nebulizer prototypes was controlled during the experiments in order to get a value as close as possible to the average droplet concentration of 1000 droplets/cm^3. All the samples collected with the APS were recorded, stored and analyzed by the Aerosol Instrument Manager software associated with the instrument.

Figure 3.11 shows in detail how the nebulizer prototype was connected. The central inlet of the prototype, where the liquid is delivered, was first connected to a three-way stopcock valve to control the charge of the compound into the liquid chamber whereas the side connection was directly connected with the air pressure controller.

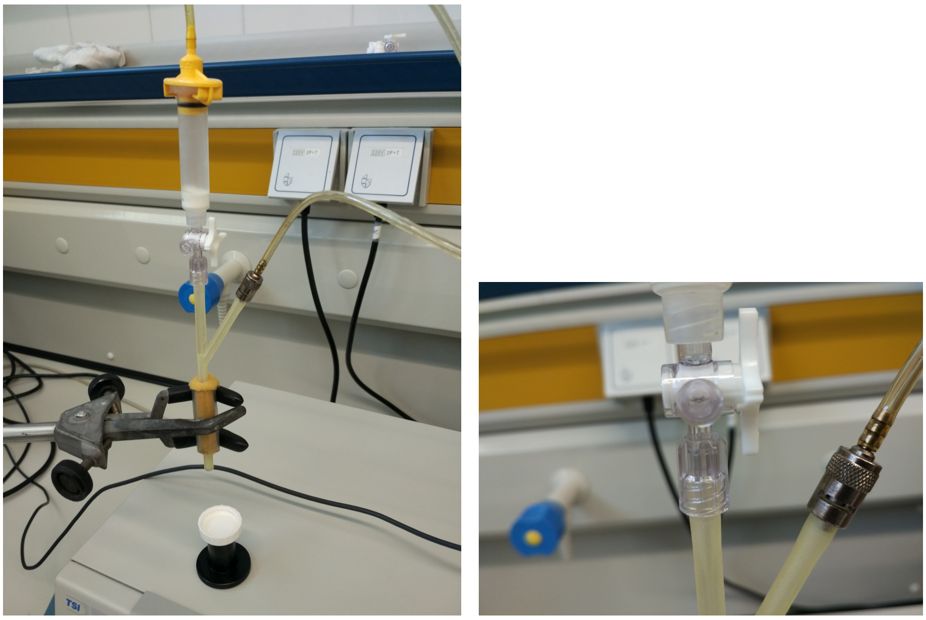
(a) (b)

Figure 3.11: (a) Setup of the nebulizer with the liquid chamber where the liquid is supplied and (b) detail of the connections to administer the compressed air and the liquid respectively.

Statistics

A statistical analysis was carried out with the data obtained. The measurements were repeated five times for each compound and prototype and the mean ± standard deviation were calculated for the D_a, MMAD and GSD. A one-way analysis of variance (ANOVA) was performed to identify any statistically significant difference between the prototypes and each compound for aerosolization rates with a $p<0.05$ accepted as significant.

3.4 Experimental Results with Distilled Water

The distance between the APS inlet nozzle and the distal part of the prototypes was controlled in order to obtain a droplet concentration value close to 1000 droplets/cm^3, as recommended. This distance varied depending on the prototype, compound used and the driving pressure applied. Thus, with the experiments carried out with H_2Od, this optimal distance was found at 19-24.2 cm and 24-28 cm with Prototype 1 and Prototype 2 respectively.

The aerosols produced by Prototype 1, during H_2Od aerosolization, provided MMAD values lower than 9 μm. Specifically, a minimum value was observed with a driving pressure of 1 bar (5.96 ± 0.76 μm) and a maximum value with a driving pressure of 2 bar (8.80 ± 1.84 μm), see Figure 3.12a. On the contrary, larger MMAD measurements were achieved during aerosolization with Prototype 2 with values up to 15 μm. A minimum value with a driving pressure of 1 bar (13.03 ± 2.62 μm) and a maximum peak with a driving pressure of 2 bar (14.93 ± 1.13 μm) were obtained. It should be noted that for both prototypes the minimum and maximum MMAD values were obtained for the same driving pressures, 1 and 2 bar respectively.

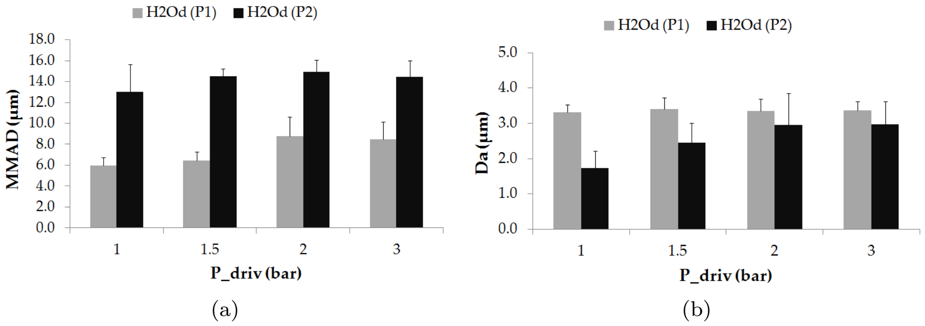

(a) (b)

Figure 3.12: (a) MMAD (μm) and (b) D_a (μm) values for Prototype 1 and Prototype 2 as a function of the driving pressure for distilled water (H_2Od). Values are given as mean ± standard deviation.

With regard to the aerodynamic diameter (D_a), the results obtained with Prototype 1 and H_2Od maintained a stable value regardless of the driving pressure, between 3.32 ± 0.20 μm (1 bar) and 3.40 ± 0.31 μm (1.5 bar). Prototype 2, however, presented a smooth increment in the D_a proportionally with the driving pressure, as shown in Figure 3.12b.

According to the GSD values obtained, both prototypes produced aerosols with many different sizes (heterodisperse aerosols), as shown in Table 3.3, with GSD values between 1.79 ± 0.03 (Prototype 1 at 1 bar) and 2.47 ± 0.28 (Prototype 2 at 2 bar).

	GSD	
P (bar)	**Prototype 1**	**Prototype 2**
1	1.79 ± 0.03	1.95 ± 0.31
1.5	1.86 ± 0.05	2.31 ± 0.26
2	1.86 ± 0.06	2.47 ± 0.28
3	1.90 ± 0.05	2.37 ± 0.12

Table 3.3: Geometric standard deviation (GSD) for both prototypes nebulizing H_2Od at different pressures. Values are given as mean ± standard deviation.

Figure 3.13 represents the droplet mass and number distribution of one of the aerosol samples taken for H_2Od with each prototype and suplying the same driving pressure of 1.5 bar. From there, it can be visualized how the droplet mass concentration with Prototype 1 (see Figure 3.13a) is transported by droplets in a wider range than Prototype 2, where most of the aerosol mass is formed by droplets of 10-20 μm (see Figure 3.13b). However, taking into account the concentration number, Prototype 2 presents most of the droplets classified below 3 μm (see Figure 3.13c-3.13d), which is in concordance with the difference between the values of D_a and MMAD explained. The different behavior of Prototype 2 with respect to Prototype 1 may be attributed to the half-circular ring geometry proposed for the air delivery and its possible influence in the breakup and coalescence of the aerosol droplets.

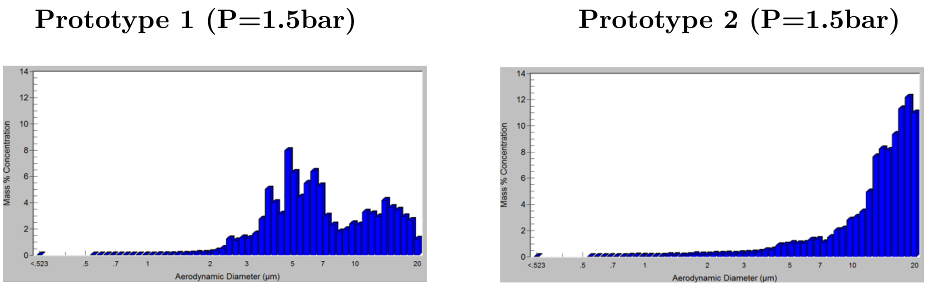

(a) Mass % concentration

(b) Mass % concentration

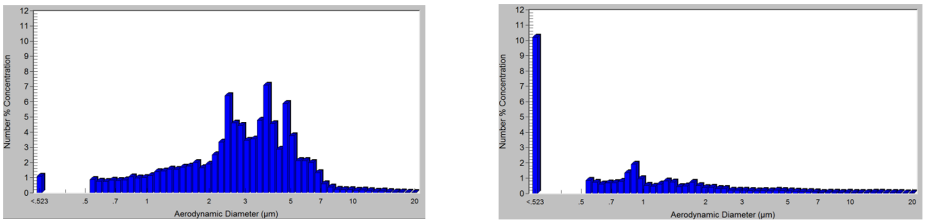

(c) Number % concentration

(d) Number % concentration

Figure 3.13: Mass and number distribution of an H_2Od aerosol sample with Prototype 1 (left) and Prototype 2 (right). (Screenshots taken directly from the Aerosol Instrument Manager software).

3.5 Experimental Results with PFCs: PFD and FC75

After these initial tests carried out with H_2Od, PFCs were tested in order to study in detail the behaviour of both nebulizer prototypes under a compound that can be used subsequently as a mixture with surfactant. Similarly, the optimal distance between the APS inlet nozzle and the distal part of the prototypes was controlled to take the measurements. With PFD this distance varied between 9-22.5 cm and with FC75 between 7-19 cm, depending on the prototype used and the driving pressure applied.

With regard to the MMAD values, the results with both prototypes showed relatively uniform values, close to 12 μm, for the two driving pressures considered. The largest value (13.08 ± 0.36 μm) was obtained with PFD and Prototype 1 applying a driving pressure of 3 bar, whereas Prototype 2 with FC75 provided a minimum value of 11.96 ± 0.17 μm (see Figure 3.14a). The large difference in the MMAD results obtained, compared with those under H_2Od, may be caused due to the high volatility of the PFCs compounds.

The D_a in all cases tested was below 5 μm, as shown in Figure 3.14b. The results with Prototype 2 were slightly lower than those obtained with Prototype 1 for each case and driving pressure. In addition, larger values were achieved with PFD irrespective of the prototype geometry and the pressure defined. The two half-circular rings surrounding the Prototype 2, where the air is delivered, instead of the circular lumens of Prototype 1, may contribute to a larger breakup of the PFCs and, therefore, the generation of smaller droplets. The largest D_a value was achieved with Prototype 1 and PFD (5.00 ± 1.38 μm) whereas Prototype 2 with FC75 provided the minimum value (2.87 ± 0.07 μm). In addition, for the same pressure and the same prototype, the size of the droplets was smaller for the case with FC75 in comparison with PFD, as shown in Figure 3.14b. The reason could be found in the fact that the vapor pressure of the FC75 (63 mmHg) is four times larger than the PFD (14 mmHg). In the case of FC75, the nebulization might lead to the development of smaller droplets or even the generation of PFC vapor [71] [103].

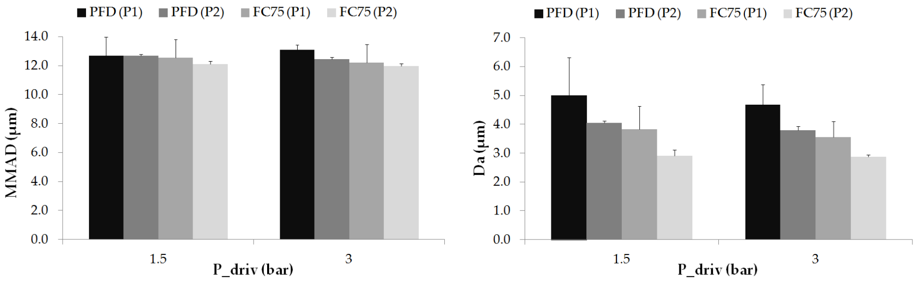

(a)

(b)

Figure 3.14: (a) MMAD (μm) and (b) D_a (μm) values for Prototype 1 and Prototype 2 as a function of the driving pressure for PFD and FC75. Values are given as mean ± standard deviation.

As happened with H_2Od, both prototypes produced heterodisperse PFC aerosols with GSD values between 2.00 ± 0.08 (Prototype 2 with FC75 at 1.5 bar) and 2.34 ± 0.02 (Prototype 2 with PFD at 1.5 bar), as detailed in Table 3.4.

GSD				
	Prototype 1		**Prototype 2**	
P (bar)	**PFD**	**FC75**	**PFD**	**FC75**
1.5	2.23 ± 0.14	2.26 ± 0.12	2.34 ± 0.02	2.00 ± 0.08
3	2.24 ± 0.10	2.25 ± 0.08	2.29 ± 0.02	2.04 ± 0.02

Table 3.4: Geometric standard deviation (GSD) for both prototypes nebulizing PFD and FC75 at different pressures. Values are given as mean ± standard deviation.

Figure 3.15 and 3.16 represents the droplet mass and number distribution obtained by means of the APS of one of the aerosol samples taken for PFD and FC75, respectively. In the post-process it must be noted that for PFD and FC75 compounds, whose density is out of the 0.9-1.1 g/cm^3 range, it is necessary to apply the Stokes correction to obtain the corrected aerodynamic diameter (D_{a2}); see Equations 3.1-3.3. For the correction of the diameter D_{a1} measured with the APS several parameters are taken into account: the dynamic viscosity and the air density at 20°C (μ_{air}, ρ_{air}), the air velocity through the nozzle (U=15000 cm/s), the average droplet velocity ($\bar{V}$), the PFC compound density used (ρ) and the density of the polystyrene latex particles used by the manufacturer to calibrate the system (ρ_{PSL}=1.05g/cm^3).

$$D_{a2} = D_{a1} \left[\frac{6 + R_2^{2/3}}{6 + R_1^{2/3}} \right]^{1/2} \tag{3.1}$$

$$R_1 = \frac{\rho_{air} \left(U - \bar{V} \right) D_{a1}}{\mu_{air} \sqrt{\rho_{PSL}}} \tag{3.2}$$

$$R_2 = \frac{\rho_{air} \left(U - \bar{V} \right) D_{a2}}{\mu_{air} \sqrt{\rho}} \tag{3.3}$$

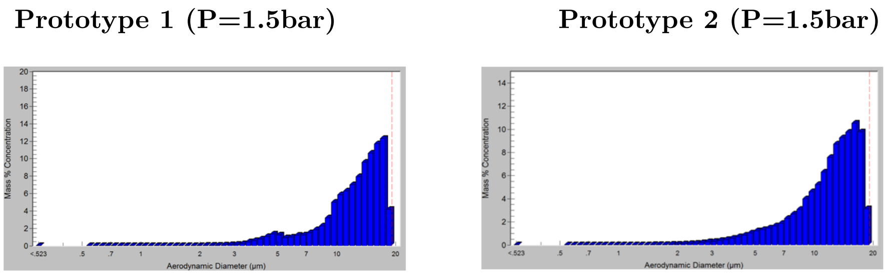

(a) Mass % concentration (b) Mass % concentration

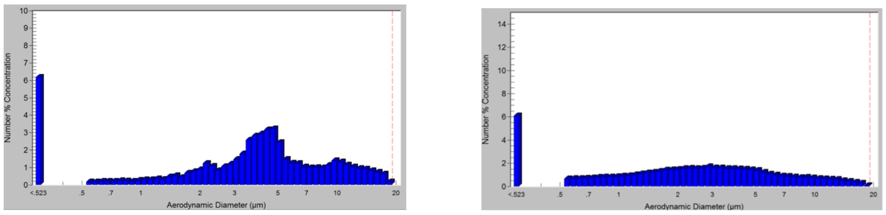

(c) Number % concentration (d) Number % concentration

Figure 3.15: Mass and number distribution of a PFD aerosol sample with Prototype 1 (left) and Prototype 2 (right).

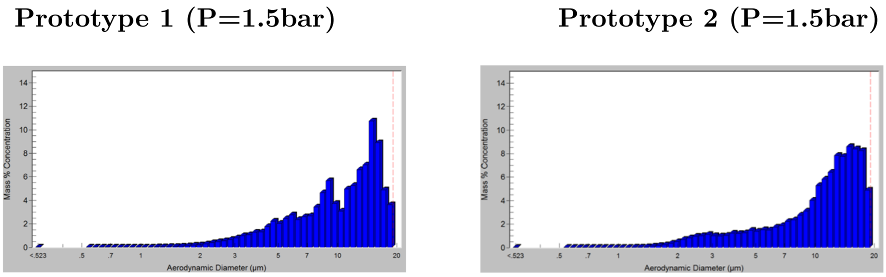

(a) Mass % concentration (b) Mass % concentration

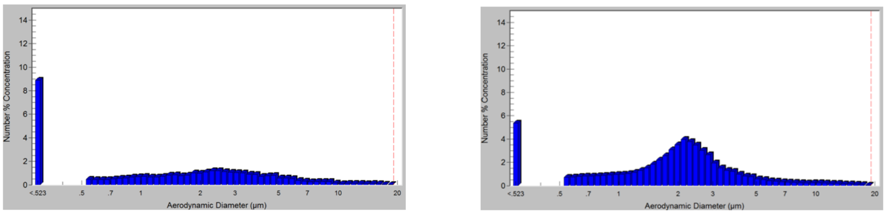

(c) Number % concentration (d) Number % concentration

Figure 3.16: Mass and number distribution of a FC75 aerosol sample with Prototype 1 (left) and Prototype 2 (right).

3.6 Discussion and Conclusions

The current experimental study has been carried out to evaluate and compare two novel nebulizer prototypes to generate respirable droplets with potential to be delivered in the supraglottic region [129]. The prototypes were created by additive manufacturing techniques and subsequently tested with an APS in order to measure the particle size distribution. This study reflects the importance of the nebulizers' geometry and how it can affect in the aerosol size distribution. Figure 3.17 illustrates the nebulization process with each one of the prototypes proposed.

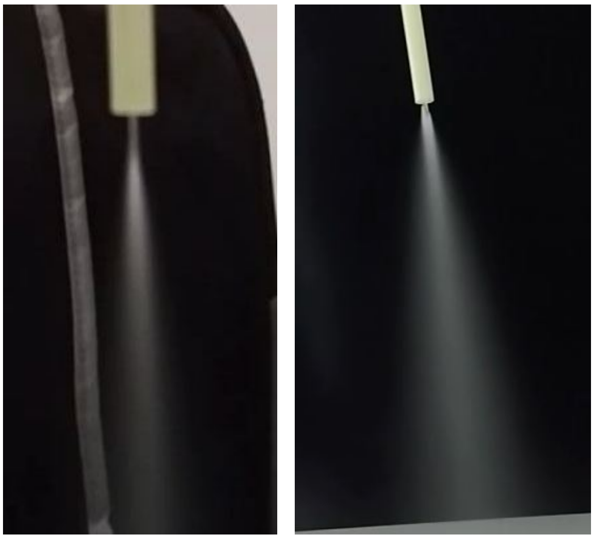

(a) (b)

Figure 3.17: (a) Nebulization case with Prototype 1 and (b) with Prototype 2.

A main finding of the evaluation of these two novel nebulizer prototypes was that they produced droplets with aerodynamic diameters within the optimal range recommended of D_a=1-5 μm for its correct inhalation [130]. In the upper respiratory tract, droplets of 2-5 μm are desirable. Droplets of size larger than 5 μm are mainly deposited by impaction in the oropharyngeal region and are unable to reach to the lungs, whereas droplets of size smaller than 1 μm are mostly exhaled without deposition. It is also important to note that the MMAD values obtained were between 6-13 μm and, therefore, a high amount of the aerosol is transported by droplets larger than 5 μm. Nevertheless, a larger MMAD values might not be a problem taking into account that the aim of these prototypes is to be placed in the supraglottic region. Due to the spreading properties of viscous substances as the surfactant, droplets with larger diameters than 5 μm could reach the lungs along with finer droplets that could penetrate further into the smaller airways for deep lung delivery [78].

With regard to Prototype 1, our findings with H_2Od have shown similar values in terms of D_a compared with those obtained by Goikoetxea et al. [98] using the Aeroprobe pneumatic catheter. In addition, PFCs provided slightly larger D_a values with both prototypes. In this study, the D_a value varies in a range of 3-5 μm while in Goikoetxea et al. [98] values approximately of 2 μm were measured. This increment could be benefit to obtain a better deep lung deposition. The difference in MMAD with PFCs between both studies is more pronounced, since the prototypes proposed in the current thesis provided most of the aerosol mass distributed in droplets within 10-20 μm. The results with the Aeroprobe pneumatic catheter showed lower MMAD values even though the experiments were also carried out at higher driving pressures (4-7 bar). On the other hand, an important difference in the droplet size distribution was observed with the atomizing system of Milesi et al. [79], where droplets with median diameter of 40-60 μm were measured at the tip of their catheter.

The study presents some limitations that must be acknowledged. During the droplet size distribution measurements it was observed that the aerosolization rate was too high to nebulize the 5 ml of compound contained in the liquid chamber in each sample. This issue is directly related with the dimensions of the nebulizer lumens of the prototypes manufactured, which were adjusted as close as possible to the limitations of the additive manufcaturing technology and the 3D printer used. The goal at this point is to adjust the dimensions of the lumens in the distal tip of the prototypes in order to produce an aerosol with lower aerosolization rates, i.e., an increase in the aerosolization time to administer a dose. This will also lead to a reduction in the distal pressure, which is indispensable not to exceed a value of 10 cmH_2O suggested by neonatologists. All these aspects are addressed in the next chapter of this thesis for the design and manufacturing of new improved and optimized prototypes.

CHAPTER 5

CONCLUSIONS AND FUTURE WORK

5.1 Conclusions

The present Chapter summarizes the main conclusions obtained from the analysis of the experimental and numerical results obtained in this thesis, first with the IC-1.1 and finally with the nebulizer prototypes designed and manufactured with additive manufacturing techniques.

The **experimental results obtained with the IC-1.1** provided aerosol droplets with $\bar{D}_a$ values within the recommended size values of 1-5 μm to be considered respirables in the supraglottic region. Specifically, for both PFC compounds studied at driving pressures of 4 and 5 bar, the results varied between 2.28 $\pm$ 0.22 μm and 4.33 $\pm$ 0.01 μm. With regard to the MMAD, results between 5-10 μm were obtained with a minimum value of 4.83 $\pm$ 0.08 μm and a maximum value of 10.01 $\pm$ 0.01 μm. These MMAD results indicate that the aerosol generated by the IC-1.1 contains droplets larger than 5 μm. However, it must be taken into account that the aerosol is generated in the supraglottic region and, therefore, the deposition of droplets larger than 5 μm in the nasopharyngeal region is avoided. The GSD results varied from 1.61 ± 0.01 to 2.04 ± 0.02, leading to the formation of heterodisperse aerosols.

The **CFD numerical model** developed is able to predict the downstream behavior of the aerosol, i.e., the air flow and the droplets formed. The axial velocity results with a pressure of 4 bar were monitored at several distances from the catheter tip and validated with experimental data [98]. These models are able to predict the cumulative mass distribution based on the aerosol droplets size at the exit of the IC-1.1. The overprediction of the CFD numerical model with respect to the experimental data suggests that the collision and coalescence of PFC droplets, that was not included in the CFD model, may be a key factor during the aerosol formation. In conclusion, the application of CFD techniques has been proven as an interesting tool to study the droplet size and mass distribution of the aerosol generated and, therefore, to research new nebulizer devices. It is also important to specify that these type of CFD simulations are quite demanding in time and require the use of High Performance Computing (HPC).

Additive manufacturing techniques have shown potential to **create a new nebulizer prototype** able to generate respirable droplets to be delivered in the supraglottic region. Specifically, the PolyJet technology has been considered the best option to manufacture a prototype device with the dimensions and the accuracy needed for this type of application. The experiments carried out with both prototypes showed $\bar{D}_a$ values within the optimal range recommended of 1-5 μm for its correct inhalation and MMAD values between 6-13 μm. It must be noted that, even though the aerosol produced with these prototypes contains droplets larger than 5 μm, the final goal of these nebulizer prototypes is to be used with surfactant. The viscous properties of this compound facilitate its distribution beyond the trachea once deposited in the walls and, according to medical experts, if surfactant reaches the third generation it would be sucessfully spread to the distal part of the lungs. Therefore, the experimental results obtained with the nebulizer prototypes designed and manufactured in the current thesis offer an encouraging starting point to continue with their optimization and to carry out *in vivo* experiments on animals.

5.2 Future Work

The following future lines of research are proposed to continue progressing in the investigation of the RDS treatment with an aerosolized administration by means of the nebulizer prototype devices presented in the current thesis.

5.2.1 CFD Studies with the Nebulizer Prototypes

For future investigations, it would be highly interesting to improve the CFD numerical model presented in this thesis with the addition of new mathematical models. In particular, it is recommended to study the implementation of the **primary atomization** to achieve a connection between the nebulizer prototype geometry and the formation of aerosol droplets. Nowadays, the CFD codes are working to implement models, as the Linearized Instability Sheet Atomization (LISA) model, to simulate the breakup of a thin liquid sheet. However, this model is proposed to be implemented with special pressure-swirl atomizers that are used for combustion processes and the simulations require of very long computational times and the use of parallel computing with workstations. It is also suggested to include in the CFD model the **airways geometry** where the nebulizer prototype will be placed. In this case, it would be advisable to take into account the **temperature and relative humidity** that exist within the airways. These factors may play an important role in the droplet size distribution, with an approximate temperature of 37°C and a relative humidity close to a 100% in the respiratory system. Additionally, it might be interesting to study the **liquid fluid film** to analyze the behavior of the aerosol droplets deposited on the walls of the airways and to see if they spread towards the lungs.

5.2.2 Pressure Control System

The experiments performed with Prototype 4.2 (see Chapter 4) showed the potential to achieve an emptying rate of the compound contained in the liquid chamber with the application of pressures in small ranges of 0.1-0.5 bar. However, the air pressure controller used in these experiments, that has an operating range of 0-7 bar, does not allow to control accurately the pressure in these small intervals. For that reason, it has been considered to include a **pressure control system** to manage the pressure applied to both the piston placed within the liquid chamber and to the side connection of the prototype. After analyzing different options and taking into account the precise control of pressure needed, the use of **Sentronic Plus Proportional valves** was considered the best choice. The operating principle of this valve, illustrated in Figure 5.1, is summarized in three steps [131]:

- *Applying pressure:* The pressurization piston is operated and the flow is released from port 1 to port 2.
- *Maintaining pressure:* The exhaust piston is in its central position: the flow between port 2 and port 1 or port 3 is blocked.
- *Exhausting pressure:* The exhaust piston is lifted and the flow from port 3 to port 2 is released.

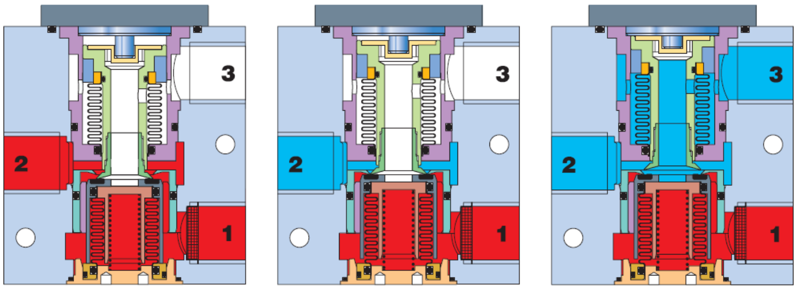

Figure 5.1: Operating principle. Source: Asco Numatics [131].

The nebulizer prototypes designed and manufactured in the current thesis have two independent connections, where pressure is applied to the piston placed within the liquid chamber and to the side connection of the prototype, respectively. Therefore, two proportional valves have been installed to provide an independent pressure control in real time to each connection of the prototype.

- A proportional control valve, with an operating range of 0-500 mbar, to **control the emptying time of the liquid chamber** and, therefore, the nebulization velocity.
- A proportional control valve, with an operating range of 0-100 mbar, to **control the compreesed air pressure** that will produce the liquid breakup and will generate the aerosol.

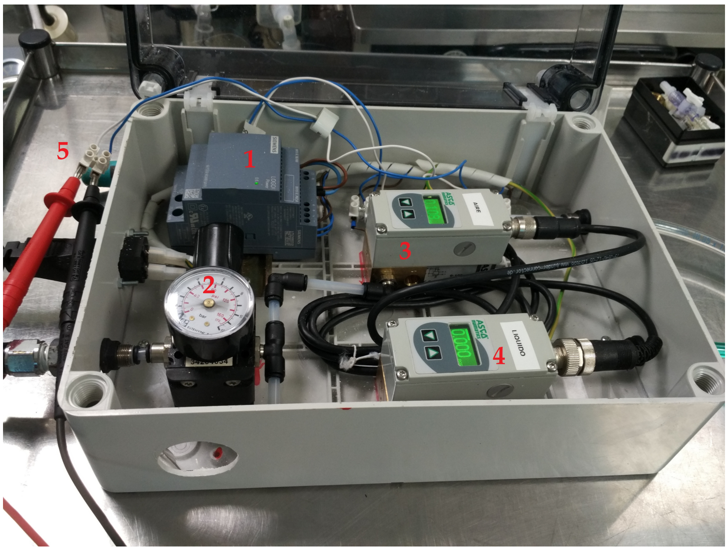

Figure 5.2: Experimental setup with the Sentronic valves.

The experimental setup developed with the pressure control system includes the following elements: (See Figure 5.2).

1. A 24V power supply.
2. A pressure regulator to control the maximum allowable pressure admitted by the proportional control valves (2 bar).

3. A Sentronic Plus proportional control valve (control the compressed air through the side connection of the prototypes).
4. A Sentronic Plus proportional control valve (control the pressure applied to the piston placed within the liquid chamber).
5. A voltage control (0-10 V).

At the end of this thesis, the experimental setup with the pressure control system has been prepared for the development of future experiments with the latest prototypes manufactured. Figure 5.3 shows a prototype connected to both proportional control valves. The control parameters can be changed with the Data Acquisition Software (DaS) associated with the valves in order to adapt the application of pressure through the prototype in real-time.

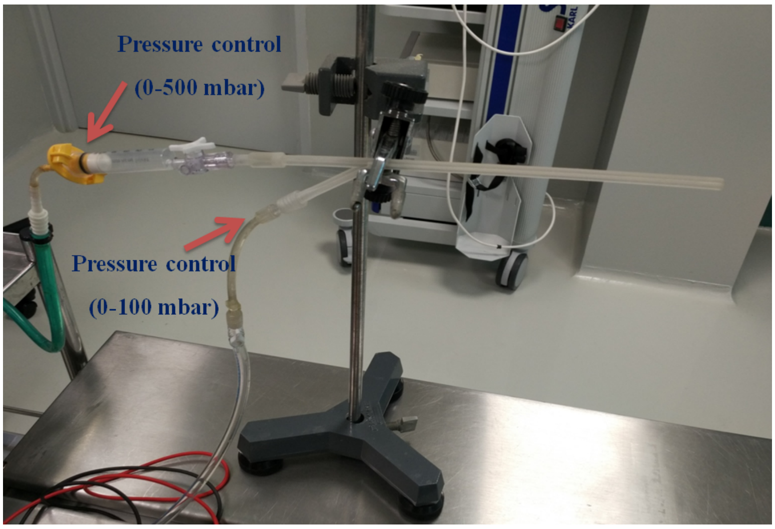

Figure 5.3: Prototype connected with Sentronic valves.

5.2.3 Digitalization of a Real Trachea Geometry

During the course of this thesis it was considered interesting to obtain a trachea geometry for future CFD studies and to create a 3D model with additive manufacturing techniques, as the work presented by Richard et al. [132]. To that end, the animal experimental unit of BioCruces Health Research Institute provided a sample of a pig trachea segment. Then, the sample was digitized with the help of the Graphic Design and Engineering Projects deparment of the University of the Basque Country UPV/EHU [133].

Initially, the trachea segment was split in order to be able to scan the internal geometry. However, an incision would deform its inner shape due to the soft organic tissue composition of the trachea. To minimize this situation, the external part was previously scanned and two rigid plastic shells with the external trachea shape were created with additive manufacturing techniques, as shown in Figure 5.4a. Then, the inner surface of the trachea segment was scanned by means of structured blue light to filter out interfering ambient light. This task was carried out by the ATOS Compact Scan M5 hardware, from GOM Gmbh manufacturer, and by the Geomagic Design X software, from 3D Systems Corporation.

The post-process of the 3D scan data consists of several steps: the point clouds were treated and optimized, the interior surfaces were extracted, the two halves were joined together using rhe initial scan and shells as reference and finally it was exported to a CAD format, that will be compatible for the CFD software in future studies.

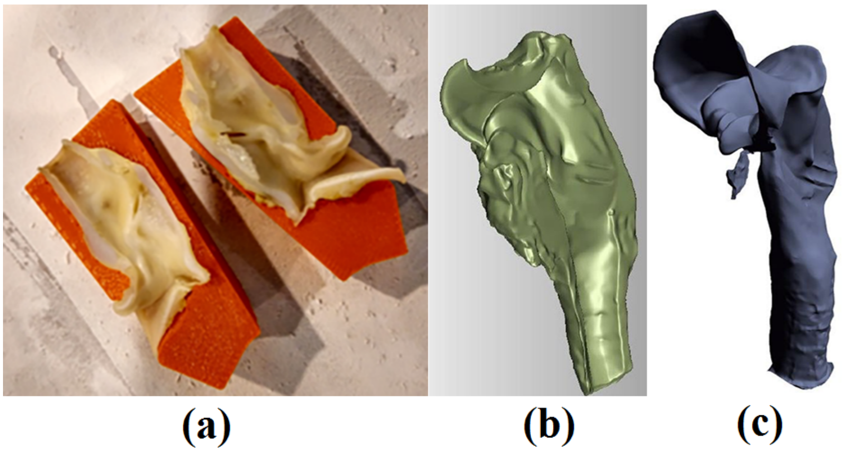

Figure 5.4: (a) Trachea digitalization.

Appendices

APPENDIX A

Nebulizer Prototypes Designs

This Appendix includes the drawings with all the geometrical details of the prototypes designed and manufactured by means of additive manufacturing techniques by the company OPTIMUS 3D.

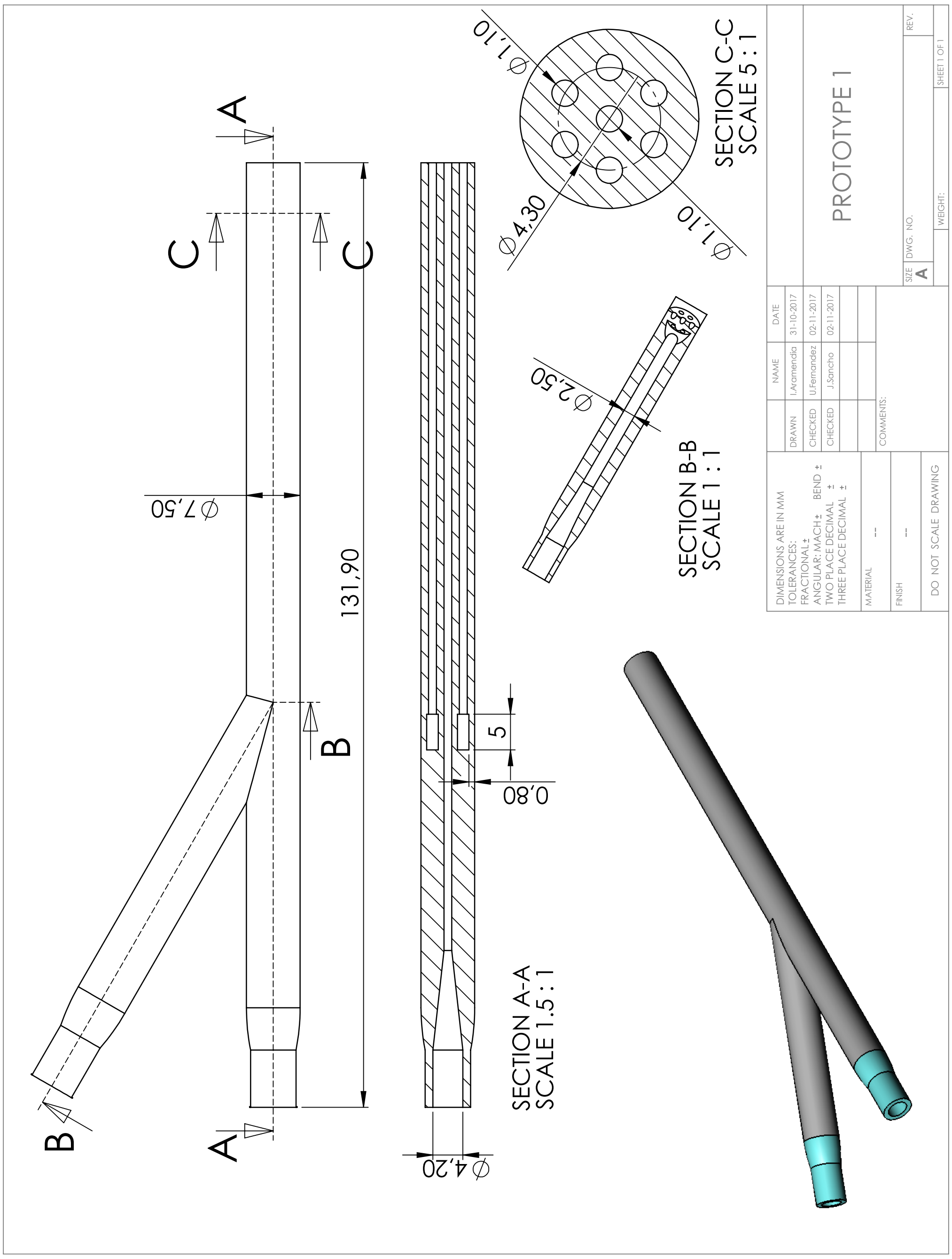
A
C
C
B
B
A
⌀7,50
131,90
5
0,80
⌀4,20
SECTION A-A
SCALE 1.5 : 1
SECTION B-B
SCALE 1 : 1
⌀2,50
SECTION C-C
SCALE 5 : 1
⌀1,10
⌀4,30
⌀1,10
DIMENSIONS ARE IN MM
TOLERANCES:
FRACTIONAL±
ANGULAR: MACH± BEND ±
TWO PLACE DECIMAL ±
THREE PLACE DECIMAL ±
MATERIAL
FINISH
DO NOT SCALE DRAWING
NAME
DATE
DRAWN
I.Aramendia
31-10-2017
CHECKED
U.Fernandez
02-11-2017
CHECKED
J.Sancho
02-11-2017
COMMENTS:
PROTOTYPE 1
SIZE
A
DWG. NO.
REV.
WEIGHT:
SHEET 1 OF 1

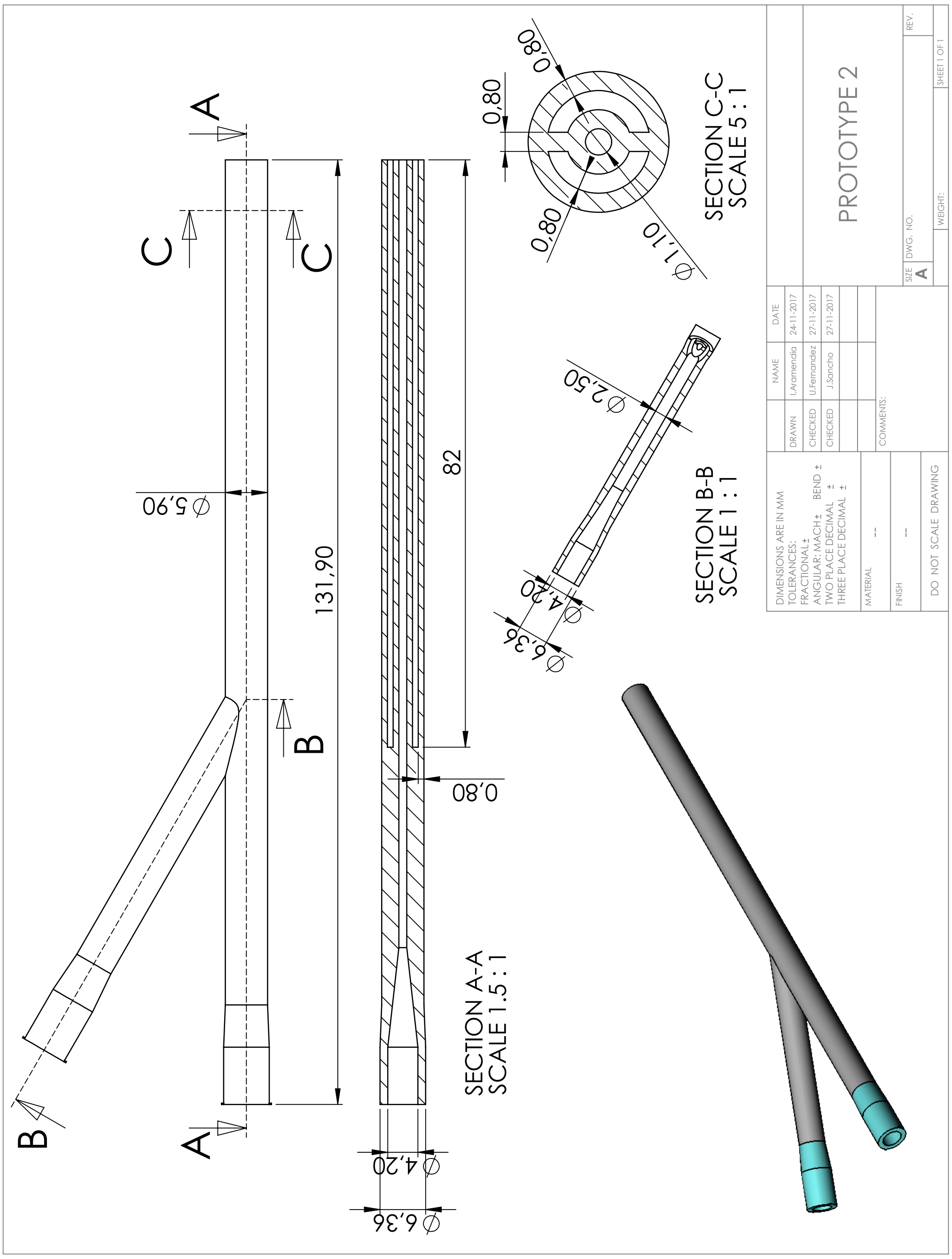
A
A
B
B
C
C
⌀5,90
131,90
82
0,80
⌀4,20
⌀6,36
SECTION A-A
SCALE 1.5 : 1
0,80
0,80
0,80
⌀1,10
SECTION C-C
SCALE 5 : 1
⌀2,50
⌀4,20
⌀6,36
SECTION B-B
SCALE 1 : 1
DIMENSIONS ARE IN MM
TOLERANCES:
FRACTIONAL ±
ANGULAR: MACH ± BEND ±
TWO PLACE DECIMAL ±
THREE PLACE DECIMAL ±
MATERIAL
--
FINISH
--
DO NOT SCALE DRAWING
NAME
DATE
DRAWN
I.Aramendia
24-11-2017
CHECKED
U.Fernandez
27-11-2017
CHECKED
J.Sancho
27-11-2017
COMMENTS:
PROTOTYPE 2
SIZE
A
DWG. NO.
REV.
WEIGHT:
SHEET 1 OF 1

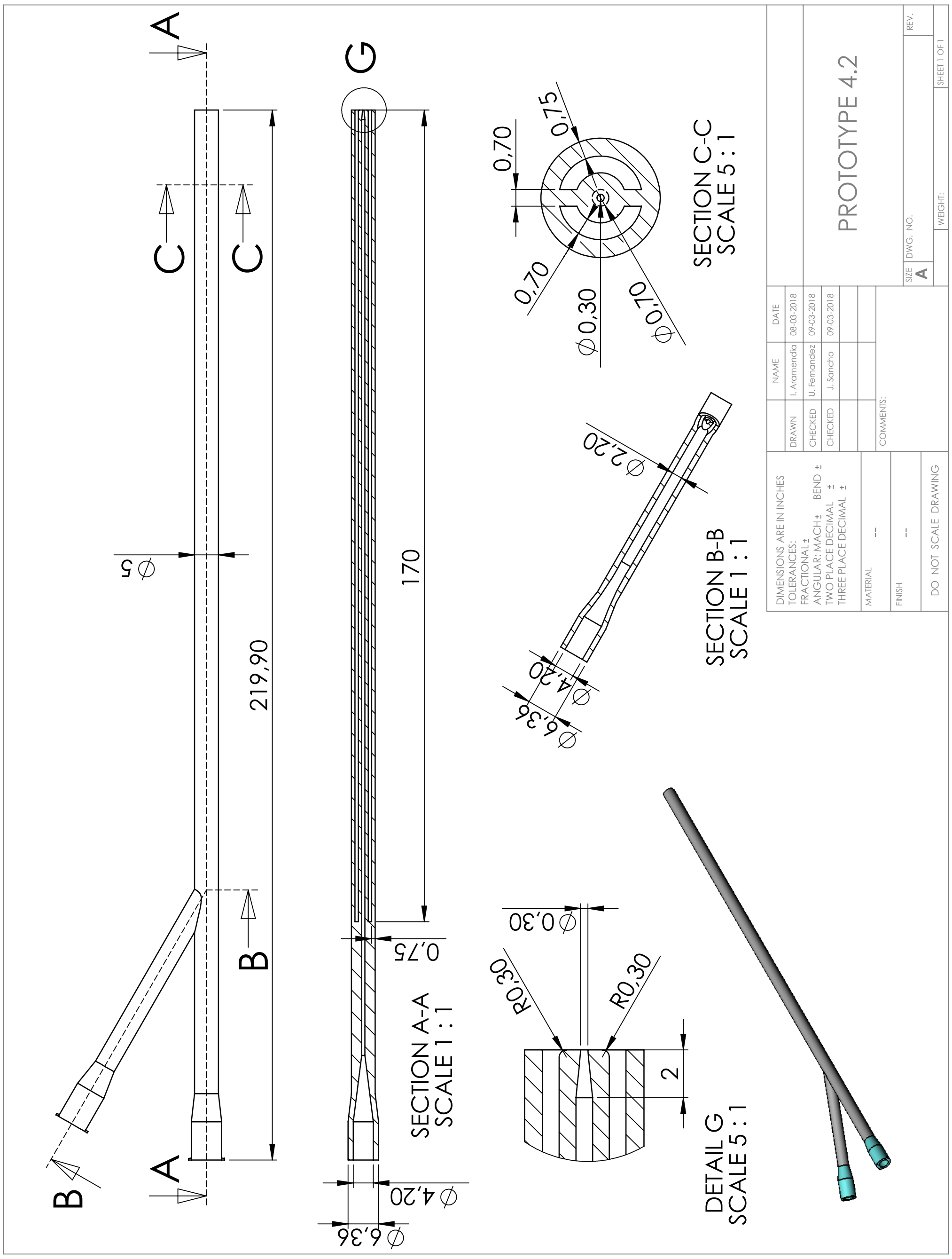
A
A
B
B
C
C
G
⌀5
219,90
170
0,75
⌀4,20
⌀6,36
SECTION A-A
SCALE 1 : 1
0,70
0,75
0,70
⌀0,30
⌀0,70
SECTION C-C
SCALE 5 : 1
⌀2,20
⌀4,20
⌀6,36
SECTION B-B
SCALE 1 : 1
⌀0,30
R0,30
R0,30
2
DETAIL G
SCALE 5 : 1
DIMENSIONS ARE IN INCHES
TOLERANCES:
FRACTIONAL ±
ANGULAR: MACH ± BEND ±
TWO PLACE DECIMAL ±
THREE PLACE DECIMAL ±
MATERIAL
--
FINISH
--
DO NOT SCALE DRAWING
NAME
DATE
DRAWN
I. Aramendia
08-03-2018
CHECKED
U. Fernandez
09-03-2018
CHECKED
J. Sancho
09-03-2018
COMMENTS:
PROTOTYPE 4.2
SIZE
A
DWG. NO.
REV.
WEIGHT:
SHEET 1 OF 1

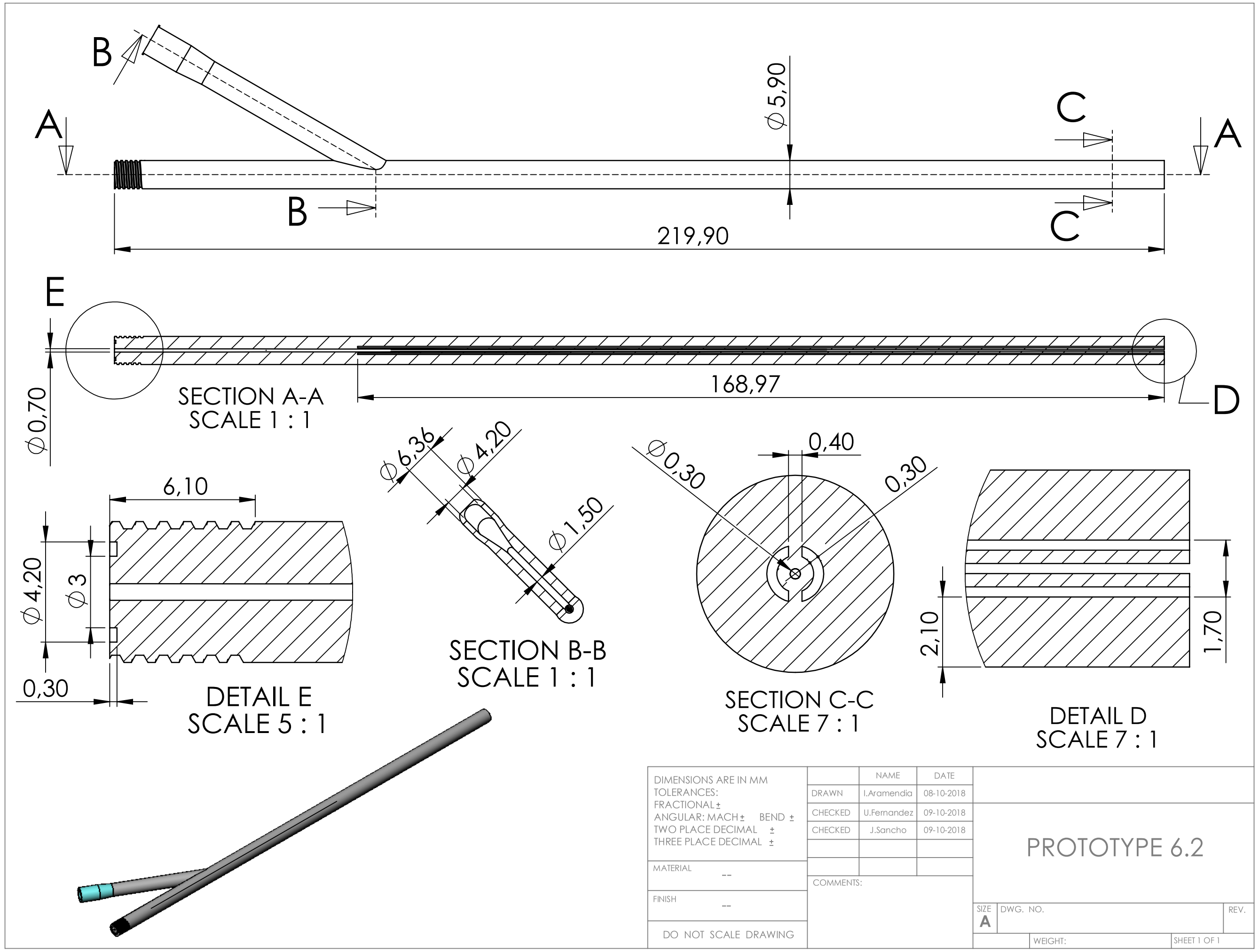
A
A
B
B
C
C
∅5,90
219,90
E
D
∅0,70
168,97
SECTION A-A
SCALE 1 : 1
6,10
∅4,20
∅3
0,30
DETAIL E
SCALE 5 : 1
∅6,36
∅4,20
∅1,50
SECTION B-B
SCALE 1 : 1
∅0,30
0,40
0,30
SECTION C-C
SCALE 7 : 1
2,10
1,70
DETAIL D
SCALE 7 : 1
DIMENSIONS ARE IN MM
TOLERANCES:
FRACTIONAL±
ANGULAR: MACH± BEND ±
TWO PLACE DECIMAL ±
THREE PLACE DECIMAL ±
MATERIAL --
FINISH --
DO NOT SCALE DRAWING
NAME
DATE
DRAWN I.Aramendia 08-10-2018
CHECKED U.Fernandez 09-10-2018
CHECKED J.Sancho 09-10-2018
COMMENTS:
PROTOTYPE 6.2
SIZE A
DWG. NO.
REV.
WEIGHT:
SHEET 1 OF 1

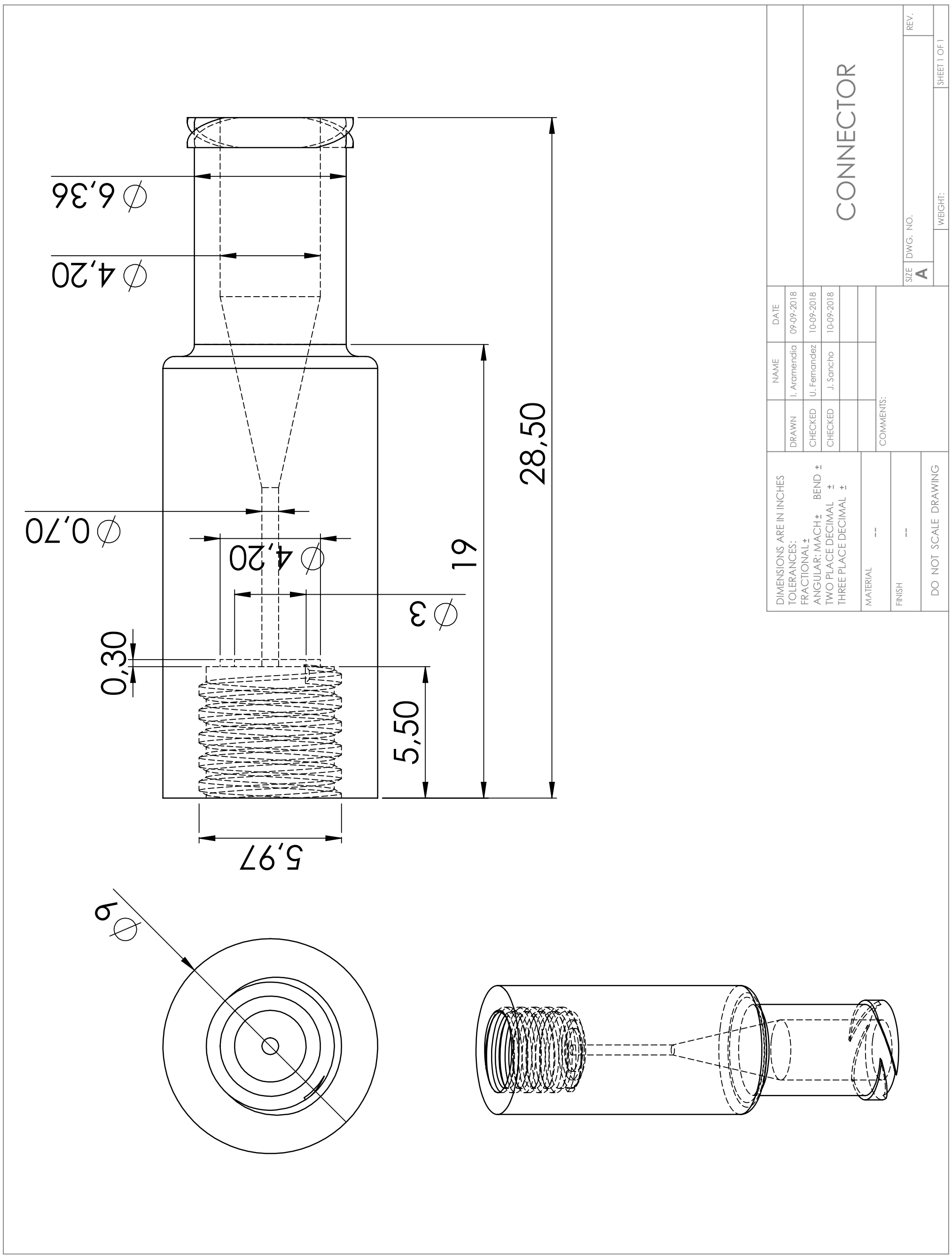
Ø 6,36
Ø 4,20
28,50
Ø 0,70
Ø 4,20
19
Ø 3
0,30
5,50
5,97
Ø 9
DIMENSIONS ARE IN INCHES
TOLERANCES:
FRACTIONAL ±
ANGULAR: MACH ± BEND ±
TWO PLACE DECIMAL ±
THREE PLACE DECIMAL ±
MATERIAL --
FINISH --
DO NOT SCALE DRAWING
NAME
DATE
DRAWN
I. Aramendia
09-09-2018
CHECKED
U. Fernandez
10-09-2018
CHECKED
J. Sancho
10-09-2018
COMMENTS:
CONNECTOR
SIZE
A
DWG. NO.
REV.
WEIGHT:
SHEET 1 OF 1

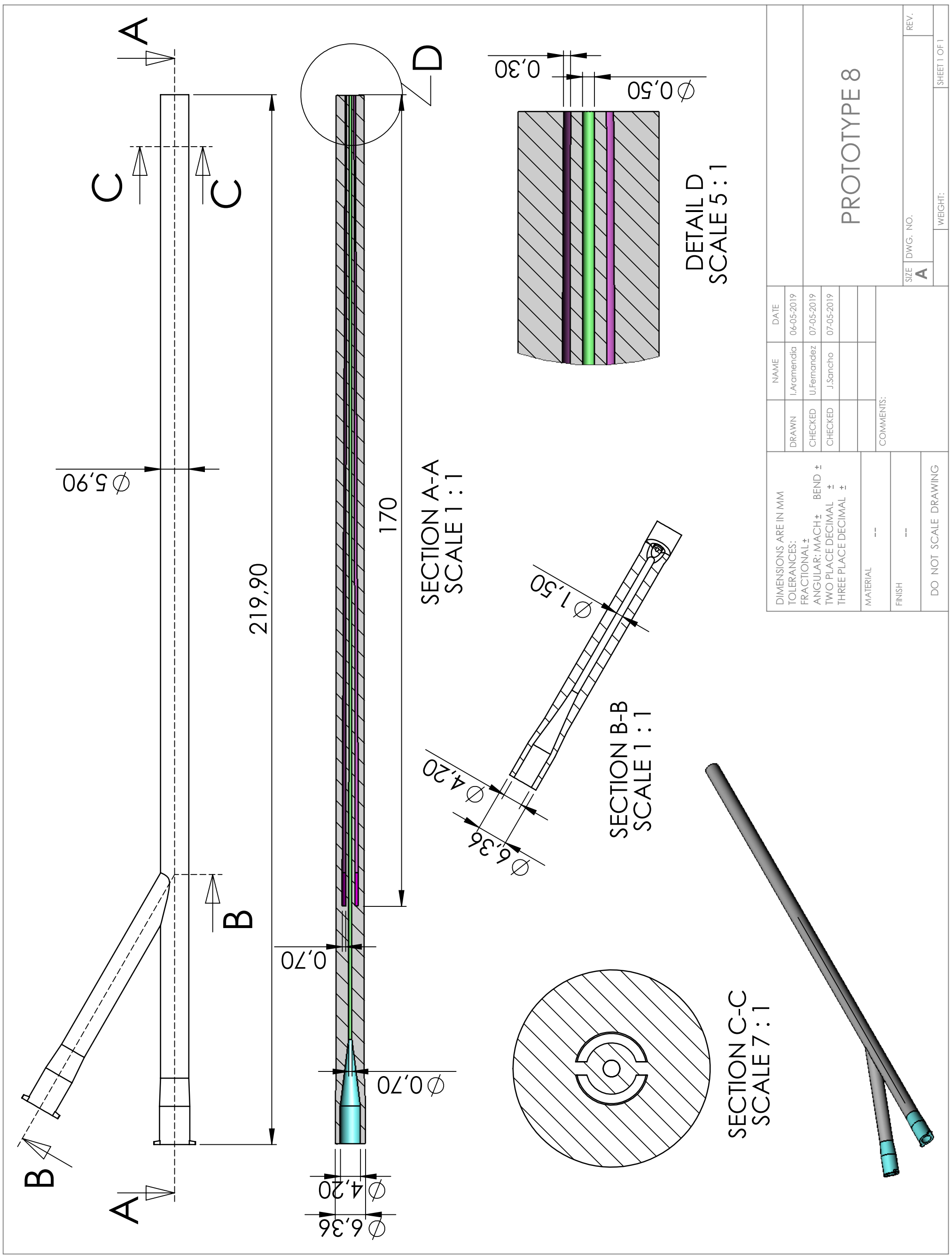
A
A
B
B
C
C
D
∅5,90
219,90
170
0,70
∅0,70
∅4,20
∅6,36
SECTION A-A
SCALE 1 : 1
0,30
∅0,50
DETAIL D
SCALE 5 : 1
∅1,50
∅4,20
∅6,36
SECTION B-B
SCALE 1 : 1
SECTION C-C
SCALE 7 : 1
DIMENSIONS ARE IN MM
TOLERANCES:
FRACTIONAL±
ANGULAR: MACH± BEND ±
TWO PLACE DECIMAL ±
THREE PLACE DECIMAL ±
MATERIAL
--
FINISH
--
DO NOT SCALE DRAWING
NAME
DATE
DRAWN I.Aramendia 06-05-2019
CHECKED U.Fernandez 07-05-2019
CHECKED J.Sancho 07-05-2019
COMMENTS:
PROTOTYPE 8
SIZE A
DWG. NO.
REV.
WEIGHT:
SHEET 1 OF 1

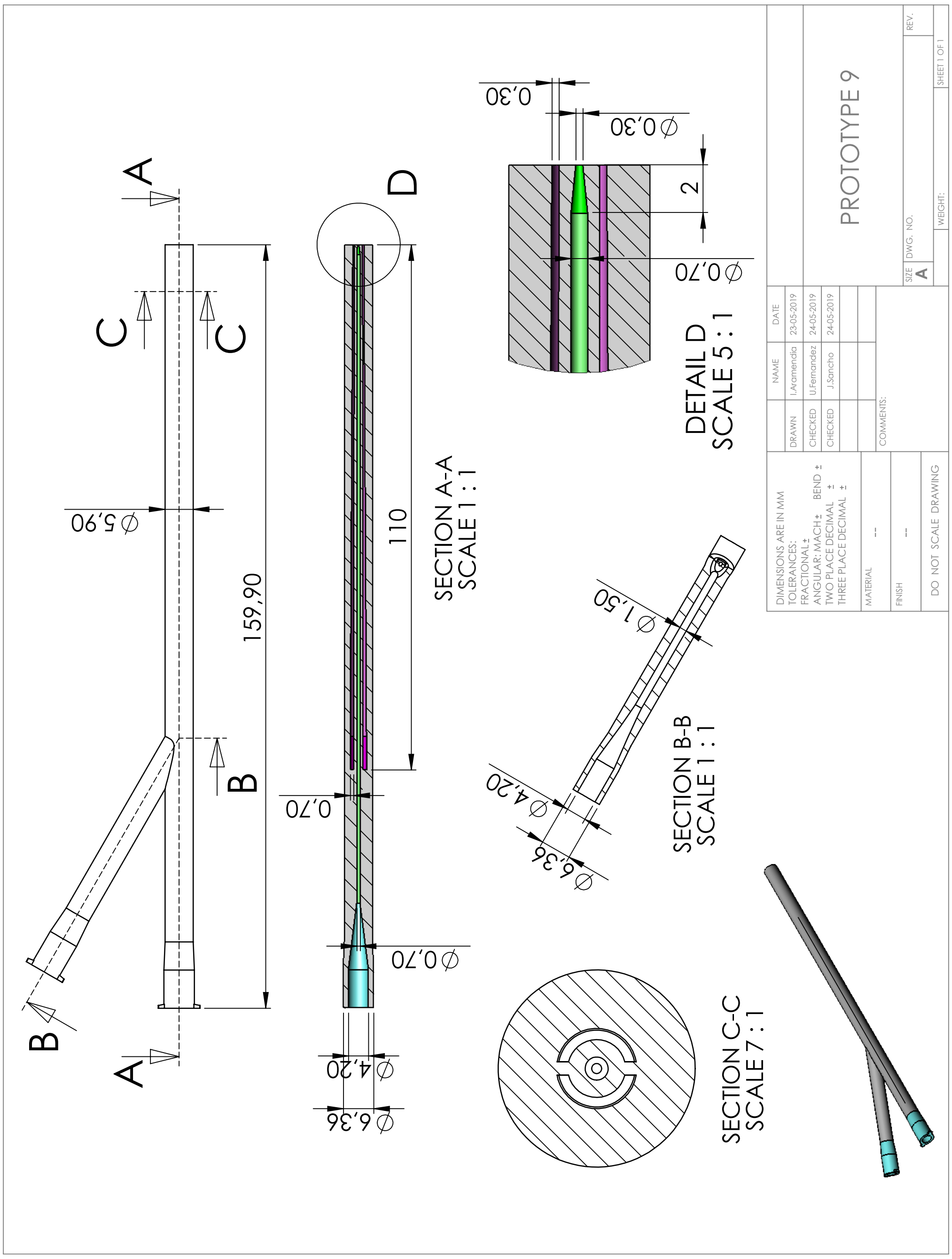
A
A
B
B
C
C
⌀5,90
159,90
D
110
0,70
⌀0,70
⌀4,20
⌀6,36
SECTION A-A
SCALE 1 : 1
0,30
⌀0,30
2
⌀0,70
DETAIL D
SCALE 5 : 1
⌀1,50
⌀4,20
⌀6,36
SECTION B-B
SCALE 1 : 1
SECTION C-C
SCALE 7 : 1
DIMENSIONS ARE IN MM
TOLERANCES:
FRACTIONAL±
ANGULAR: MACH± BEND ±
TWO PLACE DECIMAL ±
THREE PLACE DECIMAL ±
MATERIAL --
FINISH --
DO NOT SCALE DRAWING
NAME
DATE
DRAWN I.Aramendia 23-05-2019
CHECKED U.Fernandez 24-05-2019
CHECKED J.Sancho 24-05-2019
COMMENTS:
PROTOTYPE 9
SIZE A
DWG. NO.
REV.
WEIGHT:
SHEET 1 OF 1

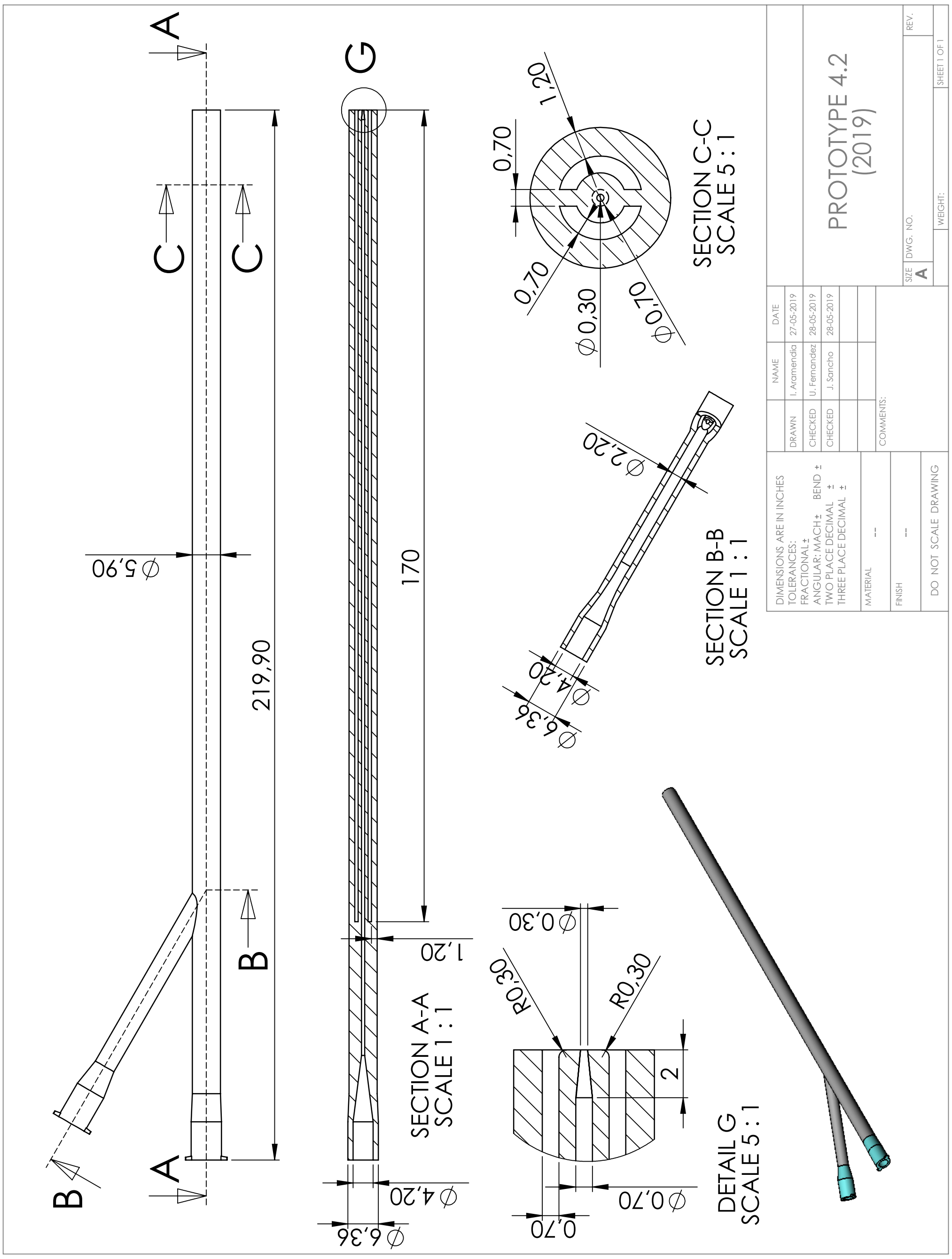
A
A
C
C
B
B
G
Ø5,90
219,90
170
1,20
Ø4,20
Ø6,36
SECTION A-A
SCALE 1 : 1
0,70
1,20
0,70
Ø0,30
Ø0,70
SECTION C-C
SCALE 5 : 1
Ø2,20
Ø4,20
Ø6,36
SECTION B-B
SCALE 1 : 1
Ø0,30
R0,30
R0,30
2
Ø0,70
0,70
DETAIL G
SCALE 5 : 1
DIMENSIONS ARE IN INCHES
TOLERANCES:
FRACTIONAL ±
ANGULAR: MACH ± BEND ±
TWO PLACE DECIMAL ±
THREE PLACE DECIMAL ±
MATERIAL
--
FINISH
--
DO NOT SCALE DRAWING
NAME
DATE
DRAWN
I. Aramendia
27-05-2019
CHECKED
U. Fernandez
28-05-2019
CHECKED
J. Sancho
28-05-2019
COMMENTS:
PROTOTYPE 4.2
(2019)
SIZE
A
DWG. NO.
REV.
WEIGHT:
SHEET 1 OF 1

APPENDIX B

Publications and Conferences

This Appendix presents the publications, conferences and book chapters that have been published during the course of this thesis:

B.1 Publications

[1] Aramendia I., Fernandez-Gamiz U., Lopez-Arraiza A., Rey-Santano C., Mielgo V., Basterretxea F. J., Sancho J., Gomez-Solaetxe M. A., Experimental Evaluation of Perfluorocarbon Aerosol Generation with Two Novel Nebulizer Prototypes. *Pharmaceutics.* 11, (1), 19, **2019.** doi:10.3390/pharmaceutics11010019. JCR (2018): 4.773 [Q1 Pharmacology & Pharmacy (26/267)].

[2] Aramendia I., Fernandez-Gamiz U., Lopez-Arraiza A., Rey-Santano C., Mielgo V., Basterretxea F. J., Sancho J., Gomez-Solaetxe M. A., Experimental and Numerical Modeling of Aerosol Delivery for Preterm Infants. *International Journal of Environmental Research and Public Health.* 15, (3), 17, **2018.**

doi:10.3390/ijerph15030423.
JCR (2018): 2.468 [Q2 Public, Environmental & Occupational Health (67/186)].

[3] Aramendia I., Fernandez-Gamiz U., Lopez-Arraiza A., Gomez-Solaetxe M. A., Lopez-Guede J. M., Sancho J., Basterretxea F. J. Computational characterization of aerosol delivery for preterm infants. *International Journal of Biology and Biomedical Engineering.* 11, 29-38, **2017.**

[4] Aramendia I., Saenz-Aguirre A., Boyano A., Fernandez-Gamiz U., Zulueta E. Oscillating U-Shaped Body for Underwater Piezoelectric Energy Harvester Power Optimization. *Micromachines.* 10, (11), 737, **2019.** doi:10.3390/mi10110737.
JCR (2018): 2.426 [Q2 Instruments & Instrumentation (25/61)].

[5] Aramendia I., Zulueta E., Teso-Fz-Betoño D., Saenz-Aguirre A., Fernandez-Gamiz U. Modeling of Motorized Orthosis Control. *Applied Sciences.* 9, (12), 2453, **2019.** doi:10.3390/app9122453.
JCR (2018): 2.217 [Q2 Physics, Applied (67/148)].

[6] Aramendia I., Fernandez-Gamiz U., Zulueta E., Saenz-Aguirre A., Teso-Fz-Betoño D. Parametric Study of a Gurney Flap Implementation in a DU91W(2)250 Airfoil. *Energies.* 12, (2), 294, **2019.** doi:10.3390/en12020294.
JCR (2018): 2.707 [Q3 Energy & Fuels (56/103)].

[7] Teso-Fz-Betoño D. Zulueta E., Fernandez-Gamiz U., Aramendia I., Uriarte I. A Free Navigation of an AGV to a Non-Static Target with Obstacle Avoidance. *Electronics.* 8, (2), 159, **2019.** doi:10.3390/electronics8020159.
JCR (2018): 1.764 [Q3 Engineering, Electrical & Electronic (154/266)].

[8] Aramendia I., Fernandez-Gamiz U., Zulueta E., Lopez-Guede, J.M., Sancho J. Power Control Optimization of an Underwater Piezoelectric Energy Harvester. *Applied Sciences.* 8, (3), 389, **2018.** doi:10.3390/app8030389.
JCR (2018): 2.217 [Q2 Physics, Applied (67/148)].

[9] Aramendia I., Fernandez-Gamiz U., Lopez-Arraiza A., Gomez-Solaetxe M. A., Lopez-Guede J. M., Sancho J. Water droplets effects on an airfoil aerodynamic performance *International Journal of Mechanics.* 11, 234-241, **2017.**

[10] Aramendia I., Fernandez-Gamiz U., Sancho J., Zulueta E. State of the art of active and passive flow control devices for wind turbines. *Dyna.* 91, (5), 512-516, **2016.** doi:10.6036/7807.
JCR (2016): 0.541 [Q4 Engineering, Multidisciplinary (70/85)].

B.2 Conferences

[1] Aramendia I., Lopez-Arraiza A., Gomez-Solaetxe M. A., Fernandez-Gamiz U., Sancho J., Rey-Santano C., Mielgo V., .Lopez de Heredia J. Computational Simulations of an Aerosol for Surfactant Delivery in Preterm Infants. *5th Iberian Meeting on Aerosol Science and Technology,* Barcelona, Spain, 4-6 July **2017.**

[2] Aramendia I., Fernandez-Gamiz U., Lopez-Arraiza A., Gomez-Solaetxe M. A., Barrenetxea L., Solaberrieta E., Minguez R., Sancho J. Aerosol Delivery by Inhalation Catheter and Trachea Digitalization. *XXXV Congreso Anual de la Sociedad Española de Ingeniería Biomédica (CASEIB),* Bilbao, Spain, November **2017.**

[3] Aramendia I., Saenz-Aguirre A., Fernandez-Gamiz U., Zulueta E., Lopez-Guede J.M., Boyano A., Sancho J. Gurney flap implementation on a DU91W250 airfoil. *2nd International Research Conference on Sustainable Energy, Engineering, Materials and Environment (IRCSEEME)* Oviedo, Spain, July **2018.**

[4] Saenz-Aguirre A., Fernandez-Resines S., Aramendia I., Fernandez-Gamiz U., Zulueta E., Lopez-Guede J.M., Sancho J. 5 MW wind turbine annual energy production improvement by flow control devices. *2nd International Research Conference on Sustainable Energy, Engineering, Materials and Environment (IRCSEEME)* Oviedo, Spain, July **2018.**

[5] Fernandez-Gamiz U., Aramendia I., Zulueta E., Ramos-Hernanz J.A., Lopez-Guede J.M. Innovative geometries for underwater piezoelectric energy harvester. *6th European Conference on Renewable Energy Systems (ECRES),* Istanbul, Turkey, June **2018.**

[6] Aramendia I., Fernandez-Gamiz U., Lopez-Arraiza A., Gomez-Solaetxe M. A., Lopez-Guede J. M., Sancho J. Water droplets effects on an airfoil aerodynamic performance *Conference on Mathematics and Computers in Science and Engineering,* London, United Kingdom October **2017.**

B.3 Book chapters

[1] Aramendia I., Fernandez-Gamiz U., Ramos-Hernanz J.A., Sancho J., Lopez-Guede J.M., Zulueta E. Flow control devices for wind turbines. in Bizon N., Mahdavi-Tabatabaei N., Blaabjerg F. and Kurt E (eds.): *Energy Harvesting and Energy Efficiency: Technology, Methods and Applications,* Berlin, Germany, Springer International Publishing AG, pp. 629-655, ISBN: 978-3-319-49875-1 **2017.**

[2] Aramendia I., Fernandez-Gamiz U., Ramos-Hernanz J.A., Sancho J., Lopez-Guede J.M., Zulueta E. Computational study of Li-ion batteries for automotive applications. in Bizon N., Dascalescu L., Mahdavi-Tabatabaei N (eds.): *Autonomous Vehicles: Intelligent Transport Systems and Smart Technologies,* New York, USA, Nova Science Publishers, pp. 431-451, ISBN: 978-1-63321-326-5 **2014.**

Bibliography

[1] Arroyo V., Diaz J., Salvador P., and Linares C. Impact of air pollution on low birth weight in spain: An approach to a national level study. *Environmental research*, 171:69–79, Apr 2019.

[2] Arroyo V., Linares C., and Diaz J. Premature births in spain: Measuring the impact of air pollution using time series analyses. *Science of the Total Environment*, 660:105–114, Apr 2019.

[3] Kamath B.D., MacGuire E.R., McClure E.M., Goldenberg R.L., and Jobe A.H. Neonatal mortality from respiratory distress syndrome: Lessons for low-resource countries. *Pediatrics*, 127(6):1139–1146, Jun 2011.

[4] Miller H.C. and Futrakul P. Birth weight, gestational age and sex as determining factors in the incidence of respiratory distress syndrome of prematurely born infants. *Journal of Pediatrics*, 72:628–635, May 1968.

[5] Hamvas A., Wise P.H., Yang R.K., Wampler N.S., Noguchi A., Maurer M.M., Walentik C.A., Schramm W.F., and Cole F.S. The influence of the wider use of surfactant therapy on neonatal mortality among blacks and whites. *The New England Journal of Medicine*, 334(25):1635–1640, May 1996.

[6] Ghanta S., Leeman K.T., and Christou H. An update on pharmaco-

logic approaches to bronchopulmonary dysplasia. *Seminars in perinatology*, 37(2):115–123, Apr 2013.

[7] Terzi E., Zarogoulidis K., Kougioumtzi I., Dryllis G., Kioumis I., Pitsiou G., Machairiotis N., Katsikogiannis N., Lampaki S., Papaiwannou A., Tsiouda T., Madesis A., Karaiskos T., Zaric B., Branislav P., and Zarogoulidis P. Acute respiratory distress syndrome and pneumothorax. *Journal of Thoracic Disease*, 6:S435–S442, Oct 2014.

[8] Kleinstreuer C., Zhang Z., and Donohue J.F. Targeted drug-aerosol delivery in the human respiratory system. *Annual Review of Biomedical Engineering*, 10:195–220, 2008.

[9] Nkadi P.O., Merritt T.A., and Pillers D.A.M. An overview of pulmonary surfactant in the neonate: Genetics, metabolism, and the role of surfactant in health and disease. *Molecular genetics and metabolism*, 97(2):95–101, Jun 2009.

[10] Pastva A.M., Wright J.R., and Williams K.L. Immunomodulatory roles of surfactant proteins a and d: implications in lung disease. *Proceedings of the American Thoracic Society*, 4(3):252–257, Jul 2007.

[11] Johansson J., Curstedt T., and Robertson B. The proteins of the surfactant system. *European Respiratory Journal*, 7(2):372–391, Feb 1994.

[12] Parra E. and Pérez-Gil J. Composition, structure and mechanical properties define performance of pulmonary surfactant membranes and films. *Chemistry and physics of lipids*, 185:153–175, 2015.

[13] Kramer B.W. The respiratory distress syndrome (RDS) in preterm infants. *Intensivmedizin und Notfallmedizin*, 44(7):403–408, 2007.

[14] Avery M.E. and Mead J. Surface properties in relation to atelectasis and hyaline membrane disease. *Ama Journal of Diseases of Children*, 97(5):517–523, 1959.

[15] Crowther C.A., McKinlay C.J.D., Middleton P., and Harding J.E. Repeat doses of prenatal corticosteroids for women at risk if preterm birth for improving neonatal health outcomes. *Cochrane Database of Systematic Reviews*, Jan 2015.

[16] Von Neergaard K. Neue auffassungen über einen grundbegriff der atemmechanik. *Zeitschrift für die gesamte experimentelle Medizin*, 66:373–394, 1929.

[17] Pattle R.E. Properties, function and origin of the alveolar lining layer. *Nature*, 175(4469):1125–1126, Jun 1955.

[18] Robillard E., Dagenais-Perusse P., Guilbeault A., Baril E., and Alarie Y. Microaerosol administration of synthetic beta-gamma-dipalmitoyl-l-alpha-lecithin in respiratory distress syndrome - preliminary report. *Canadian Medical Association journal*, 90(2):55–57, 1964.

[19] Shannon D.C. and Bunnell J.B. Diplamitoyl lecithin aerosol in RDS. *Nature*, 10(4):467–467, Jun 1976.

[20] Enhorning G. and Robertson B. Flung expansion in premature rabbit fetus after tracheal deposition of surfactant. *Pediatrics*, 50(1):58–66, 1972.

[21] Fujiwara T., Chida S., Watabe Y., Maeta H., Morita T., and Abe T. Artificial surfactant therapy in hyaline-membrane disease. *Lancet*, 1(8159):55–59, 1980.

[22] Sweet D.G., Carnielli V., Greisen G., Hallman M., Ozek E., Plavka R., Saugstad O.D., Simeoni U., Speer C.P., Vento M., Visser G.H.A., and Halliday H.L. European consensus guidelines on the management of respiratory distress syndrome-2016 update. *Neonatology*, 111(2):107–125, 2017.

[23] Perretta J.S. *Neonatal and Pediatric Respiratory Care: A Patient Case Method.* F.A. Davis Company, Philadelphia, PA, USA, 2014.

[24] McDonald C.L. and Ainsworth S.B. An update on the use of surfactant in neonates. *Current Paediatrics*, 14(4):284–289, 2004.

[25] Polin R.A. and Carlo W.A. Surfactant replacement therapy for preterm and term neonates with respiratory distress. *Pediatrics*, 133(1):156–163, Jan 2014.

[26] Ma C.C.H. and Ma S. The role of surfactant in respiratory distress syndrome. *The open respiratory medicine journal*, 6:44–53, 2012.

[27] Halliday H.L., Tarnow-Mordi W.O., Corcoran J.D., and Patterson C.C. Multicenter randomized trial comparing high and low-dose surfactant regimens for the treatment of respiratory-distress syndrome (the curosurf-4 trial). *Archives of Disease in Childhood*, 69(3):276–280, Sept 1993.

[28] Tridente A., De Martino L., and De Luca D. Porcine vs bovine surfactant therapy for preterm neonates with rds: systematic review with biological plausibility and pragmatic meta-analysis of respiratory outcomes. *Respiratory Research*, 20:28, Feb 2019.

[29] Kaiser J.R., Gauss C.H., and Williams D.K. Surfactant administration acutely affects cerebral and systemic hemodynamics and gas exchange in very-low-birth-weight infants. *Journal of Pediatrics*, 144(6):809–814, Jun 2004.

[30] Obladen M. History of surfactant up to 1980. *Biology of the neonate*, 87(4):308–316, 2005.

[31] Halliday H.L. History of surfactant from 1980. *Biology of the neonate*, 87(4):317–322, 2005.

[32] Jobe A.H. and Ikegami M. Mechanisms initiating lung injury in the preterm. *Early human development*, 53(1):81–94, Nov 1998.

[33] Clark R.H., Gerstmann D.R., Jobe A.H., Moffitt S.T., Slutsky A.S., and Yoder B.A. Lung injury in neonates: Causes, strategies for prevention, and long-term consequences. *Journal of Pediatrics*, 139(4):478–486, Oct 2001.

[34] Martinez F., Lewis J., Copland I., Engelberts D., Kavanagh B.P., Post M., Schurch S., and Belik J. Mechanical ventilation effect on surfactant content, function, and lung compliance in the newborn rat. *Pediatric research*, 56(1):19–25, Jul 2004.

[35] Gregory G.A., Kitterman J.A., Phibbs R.H., Tooley W.H., and Hamilton W.K. Treatment of idiopathic respiratory distress syndrome with continuous positive airway pressure. *New England Journal of Medicine*, 284(24):1333–1340, 1971.

[36] Sinha I.P. and Sinha S.K. Alternative therapies for respiratory distress syndrome in preterm infants. *Research and Reports in Neonatology*, 1:67–74, 2011.

[37] Khalaf M.N., Brodsky N., Hurley J., and Bhandari V. A prospective randomized, controlled trial comparing synchronized nasal intermittent positive pressure ventilation versus nasal continuous positive airway pressure as modes of extubation. *Pediatrics*, 108(1):13–17, Jul 2001.

[38] Meneses J., Bhandari V., Alves J.G., and Herrmann D. Noninvasive ventilation for respiratory distress syndrome: A randomized controlled trial. *Pediatrics*, 127(2):300–307, Feb 2011.

[39] Finer N.N. and Mannino F.L. High-flow nasal cannula: A kinder, gender CPAP? *Journal of Pediatrics*, 154(2):160–162, Feb 2009.

[40] Sinha S. and Tin W. Adjunctive drug therapies for treatment of respiratory diseases in the newborn: based on evidence or habit? *Therapeutic Advances in Respiratory Disease*, 8(2):53–62, 2014.

[41] Hummler H. and Schulze A. New and alternative modes of mechanical ventilation in neonates. *Seminars in Fetal and Neonatal Medicine*, 14(1):42–48, Feb 2009.

[42] More K., Sakhuja P., and Shah P.S. Minimally invasive surfactant administration in preterm infants. A meta-narrative review. *Jama Pediatrics*, 168(10):901–908, Oct 2014.

[43] Verder H., Robertson B., Greisen G., Ebbesen F., Albertsen P., Lundsrom K., Jacobsen T., Agertoft L., Hobolth N., Djernes B., Grytter C., Hertel J., Holm V., Hansen U.S., Kamper J., Johansen K.H., Nathan E., Lange A., Peitersen B., Pedersenbjergaard L., Skov L., Sveningsen N., Cusrstedt T., Bertelsen A., Vestergaard A., and Petersen E. Surfactant therapy and nasal continuous positive airway pressure for newborns with respiratory-distress syndrome. *New England Journal of Medicine*, 331(16):1051–1055, Oct 1994.

[44] Dani C., Corsini I., Bertini G., Fontanelli G., Pratesi S., and Rubaltelli F.F. The insure method in preterm infants of less than 30 weeks' gestation. *Journal of Maternal-Fetal and Neonatal Medicine*, 23(9):1024–1029, Sept 2010.

[45] Sandri F., Plavka R., Ancora G., Simeoni U., Stranak Z., Martinelli S., Mosca F., Nona J., Thomson M., Verder H., Fabbri L., Halliday H., and Group CURPAP Study. Prophylactic or early selective surfactant combined with ncpap in very preterm infants. *Pediatrics*, 125(6):E1402–E1409, Jun 2010.

[46] Burkhardt W., Kraft S., Ochs M., Proquitte H., Mense L., and Ruediger M. Persurf, a new method to improve surfactant delivery: A study in surfactant depleted rats. *Plos One*, 7(10):e47923, Oct 2012.

[47] Dargaville P.A., Aiyappan A., Cornelius A., Williams C., and De Paoli A.G. Preliminary evaluation of a new technique of minimally invasive surfac-

tant therapy. *Archives of Disease in Childhood-Fetal and Neonatal Edition*, 96(4):F243–F248, Jul 2011.

[48] Dargaville P.A., Aiyappan A., De Paoli A.G., Kuschel C.A., Kamlin C.O.F., Carlin J.B., and Davis P.G. Minimally-invasive surfactant therapy in preterm infants on continuous positive airway pressure. *Archives of Disease in Childhood-Fetal and Neonatal Edition*, 98(2):F122–F126, Mar 2013.

[49] Kribs A., Pillekamp F., Hünseler C., Vierzig A., and Roth B. Early administration of surfactant in spontaneous breathing with nCPAP: feasibility and outcome in extremely premature infants (postmenstrual age <= 27 weeks). *Pediatric Anesthesia*, 17(4):364–369, Apr 2007.

[50] Kribs A., Härtel C., Kattner E., Vochem M., Küster H., Möller J., Müller D., Segerer H., Wieg C., Gebauer C., Nikischin W., Wense A.v.d., Herting E., Roth B., and Göpel W. Surfactant without intubation in preterm infants with respiratory distress: First multi-center data. *Klinische Padiatrie*, 222(1):13–17, Jan 2010.

[51] Göepel W., Kribs A., Ziegler A., Laux R., Hoehn T., Wieg C., Siegel J., Avenarius S., Wense A. von der, Vochem M., Groneck P., Weller U., Moeller J., Haertel C., Haller S., Roth B., Herting E., and Network German Neonatal. Avoidance of mechanical ventilation by surfactant treatment of spontaneously breathing preterm infants (amv): an open-label, randomised, controlled trial. *Lancet*, 378(9803):1627–1634, Nov 2011.

[52] Kribs A., Roll C., Göpel W., Wieg C., Groneck P., Laux R., Teig N., Hoehn T., Böhm W., Welzing L., Vochem M., Hoppenz M., Bührer C., Mehler K., Stützer H., Franklin J., Stöhr A., Herting E., Roth B., and Investigators NINSAPP Trial. Nonintubated surfactant application vs conventional therapy in extremely preterm infants a randomized clinical trial. *Jama Pediatrics*, 169(8):723–730, Aug 2015.

[53] Kanmaz H. G., Erdeve O., Canpolat F. E., Mutlu B., and Dilmen U. Surfactant administration via thin catheter during spontaneous breathing: Randomized controlled trial. *Pediatrics*, 131(2):E502–E509, Feb 2013.

[54] Herting E. Less invasive surfactant administration (LISA) - ways to deliver surfactant in spontaneously breathing infants. *Early human development*, 89(11):875–880, Nov 2013.

[55] Dhand R. New frontiers in aerosol delivery during mechanical ventilation. *Respiratory care*, 49(6):666–677, Jun 2004.

[56] Jorch G., Hartl H., Roth B., Kribs A., Gortner L., Schaible T., Hennecke K.H., and Poets C. Surfactant aerosol treatment of respiratory distress syndrome in spontaneously breathing premature infants. *Pediatric pulmonology*, 24(3):222–224, Sept 1997.

[57] Arroe M., Pedersen-Bjergaard L., Albertsen P., Bode S., Greisen G., Jonsbo F., Lundstrom K., Struck J., Westergaard M., and Peitersen B. Inhalation of aerosolized surfactant (Exosurf (R)) to neonates treated with nasal continuous positive airway pressure. *Prenatal and Neonatal Medicine*, 3(3):346–352, Jun 1998.

[58] Berggren E., Liljedahl M., Winbladh B., Andreasson B., Curstedt T., Robertson B., and Schollin J. Pilot study of nebulized surfactant therapy for neonatal respiratory distress syndrome. *Acta Paediatrica*, 89(4):460–464, Apr 2000.

[59] Finer N.N., Merritt T.A., Bernstein G., Job L., Mazela J., and Segal R. An open label, pilot study of aerosurf combined with nCPAP to prevent rds in preterm neonates. *Journal of Aerosol Medicine and Pulmonary Drug Delivery*, 23(5):303–309, Oct 2010.

[60] Minocchieri S., Berry C.A., and Pillow J.J. Nebulised surfactant to reduce severity of respiratory distress: a blinded, parallel, randomised controlled trial. *Arch.Dis.Child.-Fetal Neonatal Ed.*, 2018.

[61] Dargaville P.A., Kamlin C.O.F., Paoli A.G. De, Carlin J.B., Orsini F., Soll R.F., and Davis P.G. The OPTIMIST-A trial: evaluation of minimally-invasive surfactant therapy in preterm infants 25-28 weeks gestation. *BMC Pediatrics*, 14:213, Aug 2014.

[62] Sood B.G., Cortez J., Kolli M., Sharma A., Delaney-Black V., and Chen X. Aerosolized surfactant in neonatal respiratory distress syndrome: Phase I study. *Early Human Development*, 134:19–25, Jul 2019.

[63] Köhler E., Jilg G., Avenarius S., and Jorch G. Lung deposition after inhalation with various nebulisers in preterm infants. *Archives of Disease in Childhood-Fetal and Neonatal Edition*, 93(4):F275–F279, Jul 2008.

[64] Dubus J.C., Vecellio L., De Monte M., Fink J.B., Grimbert D., Montharu J., Valat C., Behan N., and Diot P. Aerosol deposition in neonatal ventilation. *Pediatric research*, 58(1):10–14, Jul 2005.

[65] Tiemersma S., Minocchieri S., van Lingen R.A., Nelle M., and Devadason S.G. Vibrating membrane devices deliver aerosols more efficient than standard devices: A study in a neonatal upper airway model. *Journal of Aerosol Medicine and Pulmonary Drug Delivery*, 26(5):280–286, Oct 2013.

[66] Verma R.K., M.Ibrahim, and L.Garcia-Contreras. *Lung Anatomy and Physiology and their Implications for Pulmonary Drug Delivery*, pages 1–18. Pulmonary Drug Delivery: Advances and Challenges. John Wiley & Sons, 2015.

[67] Stahlhofen W. Experimental-determination of the regional deposition of aerosol-particles in the human respiratory-tract. *American Industrial Hygiene Association Journal*, 41(6):385–398, 1980.

[68] Salma I., Balashazy I., Winkler-Heil R., Hofmann W., and Zaray G. Effect of particle mass size distribution on the deposition of aerosols in the human respiratory system. *Journal of Aerosol Science*, 33(1):119–132, Jan 2002.

[69] Winterhalter M., Bund M., Khaladj N., Hagl C., Simon A., Hoy L., Piepenbrock S., and Rahe-Meyer N. Aerosol delivery by an ultrasonic nebulizer during different mechanical ventilation settings in a lung model–a pilot study. *Drug design, development and therapy*, 2:1–7, 2009.

[70] Ari A., Areabi H., and Fink J.B. Evaluation of aerosol generator devices at 3 locations in humidified and non-humidified circuits during adult mechanical ventilation. *Respiratory care*, 55(7):837–844, Jul 2010.

[71] Murgia X., Gastiasoro E., Mielgo V., Yerro E. Ruiz del, Alvarez-Diaz F.J., Lafuente H., Valls-i-Soler A., Gomez-Solaetxe M.A., and Rey-Santano C. Surfactant and perfluorocarbon aerosolization during different mechanical ventilation strategies by means of inhalation catheters: An in vitro study. *Journal of Aerosol Medicine and Pulmonary Drug Delivery*, 25(1):23–31, Feb 2012.

[72] Martin A.R. and Finlay W.H. Nebulizers for drug delivery to the lungs. *Expert Opinion on Drug Delivery*, 12(6):889–900, Jun 2015.

[73] Dolovich M.B. and Dhand R. Aerosol drug delivery: developments in device design and clinical use. *Lancet*, 377(9770):1032–1045, Mar 2011.

[74] Finlay W.H. *Dry Powder Inhalers*, pages 221–276. The Mechanics of Inhaled Pharmaceutical Aerosols. A.Press, 1st edition, 2001.

[75] Ari A. Jet, ultrasonic, and mesh nebulizers: An evaluation of nebulizers for better clinical outcomes. *Eurasian Journal of Pulmonology*, 16(1):1–7, Jan 2014.

[76] O'Callaghan C. and Barry P.W. The science of nebulised drug delivery. *Thorax*, 52:S31–S44, Apr 1997.

[77] Syedain Z.H., Naqwi A.A., Dolovich M., and Somani A. In vitro evaluation of a device for intra-pulmonary aerosol generation and delivery. *Aerosol Science and Technology*, 49(9):746–751, Sept 2015.

[78] Milesi I., Tingay D.G., Zannin E., Bianco F., Tagliabue P., Mosca F., Lavizzari A., Ventura M.L., Zonneveld C.E., Perkins E.J., Black D., Sourial M., and Dellaca R.L. Intratracheal atomized surfactant provides similar outcomes as bolus surfactant in preterm lambs with respiratory distress syndrome. *Pediatric research*, 80(1):92–100, Jul 2016.

[79] Milesi I., Tingay D.G., Lavizzari A., Bianco F., Zannin E., Tagliabue P., Mosca F., Ventura M.L., Rajapaksa A., Perkins E.J., Black D., Di Castri M., Sourial M., Pohlmann G., and Dellaca R.L. Supraglottic atomization of surfactant in spontaneously breathing lambs receiving continuous positive airway pressure. *Pediatric Critical Care Medicine*, 18(9):E428–E434, Sept 2017.

[80] Allen G.M., Shortall B.P., Gemci T., Corcoran T.E., and Chigier N.A. Computational simulations of airflow in an in vitro model of the pediatric upper airways. *Journal of Biomechanical Engineering-Transactions of the Asme*, 126(5):604–613, Oct 2004.

[81] Longest P.W., Vinchurkar S., and Martonen T. Transport and deposition of respiratory aerosols in models of childhood asthma. *Journal of Aerosol Science*, 37(10):1234–1257, Oct 2006.

[82] De Jongh F.H.C., Rinkel M.J.G., and Hoeijmakers H.W.M. Aerosol deposition in the upper airways of a child. *Journal of Aerosol Medicine-Deposition Clearance and Effects in the Lung*, 19(3):279–289, 2006.

[83] Liu Z., Li A., Xu X., and Gao R. Computational fluid dynamics simulation of airflow patterns and particle deposition characteristics in children upper respiratory tracts. *Engineering Applications of Computational Fluid Mechanics*, 6(4):556–571, Dec 2012.

[84] Golshahi L., Noga M.L., Thompson R.B., and Finlay W.H. In vitro deposition measurement of inhaled micrometer-sized particles in extrathoracic

airways of children and adolescents during nose breathing. *Journal of Aerosol Science*, 42(7):474–488, Jul 2011.

[85] Tsega E.G. Computational fluid dynamics modeling of respiratory airflow in tracheobronchial airways of infant, child, and adult. *Computational and Mathematical Methods in Medicine*, pages 1–9, 2018.

[86] Deng Q., Ou C., Chen J., and Xiang Y. Particle deposition in tracheobronchial airways of an infant, child and adult. *Science of the Total Environment*, 612:339–346, Jan 2018.

[87] Bass K., Boc S., Hindle M., Dodson K., and Longest P.W. High-efficiency nose-to-lung aerosol delivery in an infant: Development of a validated computational fluid dynamics method. *Journal of Aerosol Medicine and Pulmonary Drug Delivery*, 32(3):132–148, Jun 2019.

[88] Goikoetxea E., Rivas A., Murgia X., and Antón R. Mathematical modeling and numerical simulation of surfactant delivery within a physical model of the neonatal trachea for different aerosol characteristics. *Aerosol Science and Technology*, 51(2):168–177, 2017.

[89] Oldham M.J., Phalen R.F., and Heistracher T. Computational fluid dynamic predictions and experimental results for particle deposition in an airway model. *Aerosol Science and Technology*, 32(1):61–71, Jan 2000.

[90] Koombua K., Pidaparti R.M., Longest P.W., and Ward K.R. Computational analysis of fluid characteristics in rigid and flexible human respiratory airway models. *Engineering Applications of Computational Fluid Mechanics*, 2(2):185–194, Jun 2008.

[91] Elcner J., Lizal F., Jedelsky J., Jicha M., and Chovancova M. Numerical investigation of inspiratory airflow in a realistic model of the human tracheobronchial airways and a comparison with experimental results. *Biomechanics and Modeling in Mechanobiology*, 15(2):447–469, Apr 2016.

[92] Feng Y. and Kleinstreuer C. Micron-particle transport, interactions and deposition in triple lung-airway bifurcations using a novel modeling approach. *Journal of Aerosol Science*, 71:1–15, May 2014.

[93] Walenga R.L. and Longest P.W. Current inhalers deliver very small doses to the lower tracheobronchial airways: Assessment of healthy and constricted lungs. *Journal of pharmaceutical sciences*, 105(1):147–159, Jan 2016.

[94] Delvadia R.R., Longest P.W., Hindle M., and Byron P.R. In vitro tests for aerosol deposition. III: Effect of inhaler insertion angle on aerosol deposition. *Journal of Aerosol Medicine and Pulmonary Drug Delivery*, 26(3):145–156, Jun 2013.

[95] Gastiasoro-Cuesta E., Alvarez-Diaz F.J., Rey-Santano C., Arnaiz-Renedo A., Loureiro-Gonzalez B., and Valls-i-Soler A. Acute and sustained effects of lucinactant versus poractant-alpha on pulmonary gas exchange and mechanics in premature lambs with respiratory distress syndrome. *Pediatrics*, 117(2):295–303, Feb 2006.

[96] Rey-Santano C., Mielgo V.E., Andres L., Yerro E. Ruiz del, Valls-i-Soler A., and Murgia X. Acute and sustained effects of aerosolized vs. bolus surfactant therapy in premature lambs with respiratory distress syndrome. *Pediatric research*, 73(5):639–646, May 2013.

[97] Rey-Santano C., Mielgo V.E., Gomez-Solaetxe M.A., Salomone F., Gastiasoro E., and Loureiro B. Cerebral oxygenation associated with INSURE versus LISA procedures in surfactant-deficient newborn piglet RDS model. *Pediatric pulmonology*, 54(5):644–654, May 2019.

[98] Goikoetxea E., Murgia X., Serna-Grande P., Valls-i-Soler A., Rey-Santano C., Rivas A., Anton R., Basterretxea F.J., Minambres L., Mendez E., Lopez-Arraiza A., Larrabe-Barrena J.L., and Gomez-Solaetxe M.A. In vitro surfactant and perfluorocarbon aerosol deposition

in a neonatal physical model of the upper conducting airways. *Plos One*, 9(9):e106835, Sept 2014.

[99] Murgia X., Gastiasoro E., Mielgo V., Alvarez-Diaz F., Lafuente H., Valls-i-Soler A., Gomez-Solaetxe M.A., Larrabe J.L., and Rey-Santano C. Surfactant and perfluorocarbon aerosolization by means of inhalation catheters for the treatment of respiratory distress syndrome: An in vitro study. *Journal of Aerosol Medicine and Pulmonary Drug Delivery*, 24(2):81–87, Apr 2011.

[100] Guo Z.L., Lu G.P., Ren T., Zheng Y.H., Gong J.Y., Yu J., and Liang Y.J. Partial liquid ventilation confers protection against acute lung injury induced by endotoxin in juvenile piglets. *Respiratory Physiology & Neurobiology*, 167(3):221–226, Jul 2009.

[101] Kacmarek R.M., Wiedemann H.P., Lavin P.T., Wedel M.K., Tutuncu A.S., and Slutsky A.S. Partial liquid ventilation in adult patients with acute respiratory distress syndrome. *American Journal of Respiratory and Critical Care Medicine*, 173(8):882–889, Apr 2006.

[102] Kandler M.A., von der Hardt K., Schoof E., Dotsch J., and Rascher W. Persistent improvement of gas exchange and lung mechanics by aerosolized perfluorocarbon. *American Journal of Respiratory and Critical Care Medicine*, 164(1):31–35, Jul 2001.

[103] von der Hardt K., Kandler M.A., Brenn G., Scheuerer K., Schoof E., Dotsch A., and Rascher W. Comparison of aerosol therapy with different perfluorocarbons in surfactant-depleted animals. *Critical Care Medicine*, 32(5):1200–1206, May 2004.

[104] Siemens STAR-CCM+ version 11.06.011, 2017. Available at `http://mdx.plm.automation.siemens.com/` (accessed on 2 September 2017).

[105] Richardson L.F. and Gaunt J.A. The deferred approach to the limit. part i. single lattice. part ii. interpenetrating lattices. *Philosophical Transactions of*

the Royal Society of London Series A-Containing Papers of a Mathematical Or Physical Character, 226:299–361, Jul 1927.

[106] Slater J.W. Nparc. alliance cfd verification and validation web site: Examining spatial (grid) convergence, (last updated 17-09-2008).

[107] Wilcox D.C. *Turbulence Modeling for CFD.* DCW Industries, Inc, USA, 2006.

[108] Pope S.B. *Turbulent Flows.* Cambridge University Press, United Kingdom, 2000.

[109] Versteeg H. K. and Malalasekera W. *An Introduction to Computational Fluid Dynamics: The Finite Volume Method.* Pearson Education, 2nd edition, 2007.

[110] Rodi W. *Experience with two-layer models combining the K-E model with a one-equation model near the wall.* American Institute of Aeronautics and Astronautics, Washington, D.C., 1991.

[111] Wolfstein M. The velocity and temperature distribution in one-dimensional flow with turbulence augmentation and pressure gradient, 1969.

[112] Finlay W.H. *Motion of a Single Aerosol Particle in a Fluid*, pages 17–45. The Mechanics of Inhaled Pharmaceutical Aerosols. A.Press, 1st edition, 2001.

[113] Crowe C., Sommerfeld M., and Tsuji Y. *Multiphase flows with droplets and particles.* CRC Press, 1998.

[114] Schiller L. and Naumann A.Z. Ueber die grundlegenden berechnungen bei der schwerkraftaufbereitung. *Zeitschrift des Vereines Deutscher Ingenieure*, 77:318–320, 1933.

[115] Gosman A.D. and Ioannides E. Aspects of computer-simulation of liquid-fueled combustors. *Journal of Energy*, 7(6):482–490, 1983.

[116] O'Rourke P.J. and Amsden A.A. The tab method for numerical calculation of spray droplet breakup. *SAE Technical Paper Series*, 1987.

[117] Tu J., Yeoh G.H., and Liu C. *Computational Fluid Dynamics: A Practical Approach.* Chapter 5. CFD Solution Analysis Essentials. 2013.

[118] Aramendia I., Fernandez-Gamiz U., Lopez-Arraiza A., Gomez-Solaetxe M. A., Lopez-Guede J. M., Sancho J., and Basterretxea F. J. Computational characterization of aerosol delivery for preterm infants. *International Journal of Biology and Biomedical Engineering*, 11:29–38, 2017.

[119] Aramendia I., Lopez-Arraiza A., Gomez-Solaetxe M.A., Fernandez-Gamiz U., Sancho J., Rey-Santano C., Mielgo V., and Heredia J. Lopez de. Computational simulations of an aerosol for surfactant delivery in preterm infants. In *5th Iberian Meeting on Aerosol Science and Technology, Barcelona, Spain, 4-6 July 2017.*

[120] Aramendia I., Fernandez-Gamiz U., Lopez-Arraiza A., Rey-Santano C., Mielgo V., Basterretxea F.J., Sancho J., and Gomez-Solaetxe M.A. Experimental and numerical modeling of aerosol delivery for preterm infants. *International Journal of Environmental Research and Public Health*, 15(3):423, Mar 2018.

[121] Lee J.Y., An J., and Chua C.K. Fundamentals and applications of 3d printing for novel materials. *Applied Materials Today*, 7:120–133, Jun 2017.

[122] Ligon S.C., Liska R., Stampfl J., Gurr M., and Muelhaupt R. Polymers for 3d printing and customized additive manufacturing. *Chemical reviews*, 117(15):10212–10290, Aug 2017.

[123] Vukicevic M., Mosadegh B., Min J.K., and Little S.H. Cardiac 3D printing and its future directions. *JACC: Cardiovascular Imaging*, 10(2):171–184, Feb 2017.

[124] Cheng Y.L and Chu J.C. Application of rapid tooling to manufacture customized nasal mask cushion for continuous positive airway pressure (CPAP) devices. *Rapid Prototyping Journal*, 19(1):4–10, 2013.

[125] Vermeulen M., Claessens T., Van Der Smissen B., Van Holsbeke C.S., De Backer J.W., Van Ransbeeck P., and Verdonck P. Manufacturing of patient-specific optically accessible airway models by fused deposition modeling. *Rapid Prototyping Journal*, 19(5):312–318, 2013.

[126] Copploe A., Vatani M., Choi J.W., and Tavana H. A three-dimensional model of human lung airway tree to study therapeutics delivery in the lungs. *Annals of Biomedical Engineering*, 47(6):1435–1445, Jun 2019.

[127] Deckard C. and Beaman J. J. Process and control issues in selective laser sintering. In *ASME, Production Engineering Division*, pages 1–7, 1988.

[128] Fritsching U. *Spray Systems*, pages 499–598. Multiphase Flow Handbook. CRC Press, Taylor & Francis Group, Boca Raton, Florida, USA, 2006.

[129] Aramendia I., Fernandez-Gamiz U., Lopez-Arraiza A., Rey-Santano C., Mielgo V., Basterretxea F.J., Sancho J., and Gomez-Solaetxe M.A. Experimental evaluation of perfluorocarbon aerosol generation with two novel nebulizer prototypes. *Pharmaceutics*, 11(1):19, Jan 2019.

[130] Newman S.P. Aerosol deposition considerations in inhalation-therapy. *Chest*, 88(2):S152–S160, 1985.

[131] Asco Numatics. Sentronic Plus Proportional Valve for Pressure Control, 2019. Available at `https://www.asco.com/en-gb/Pages/pneumatic-valve-series-614.aspx#/#flt=e30%3D` (accessed on 20 September 2019).

[132] Richard Z., Jackson E., Jung J.P., and Kanotra S.P. Feasibility and potential of three-dimensional printing in laryngotracheal stenosis. *Journal of Laryngology and Otology*, 133(6):530–534, Jun 2019.

[133] Aramendia I., Fernandez-Gamiz U., Lopez-Arraiza A., Gomez-Solaetxe M.A., Barrenetxea L., Solaberrieta E., Minguez R., and Sancho J. Aerosol delivery by inhalation catheter and trachea digitalization. In *XXXV Congreso Anual de la Sociedad Española de Ingeniería Biomédica (CASEIB), Bilbao, Spain, November 2017.*